Bipolar Electrochemistry: A Wireless Technique for Chemical Analysis and Property Screening

by

Axline Ndzesse Sanghapi

A dissertation submitted to the Graduate Faculty of
Auburn University
In partial fulfillment of the
requirements for the Degree of
Doctor of Philosophy

Auburn, Alabama
May 05, 2013

Keywords: Bipolar electrochemistry, Raman spectroelectrochemistry, potential gradient, reaction gradient, chemical gradient.

Approved by

Curtis Shannon, Chair, Professor of Chemistry and Biochemistry
Vincenzo Cammarata, Associate Professor of Chemistry and Biochemistry
Christopher Easley, Assistant Professor of Chemistry and Biochemistry
ZhongYang Cheng, Professor of Materials Research and Education Center

Abstract

The phenomenon of bipolar electrochemistry was first exploited about three decades ago in the industrial sector to minimize power dissipation and to carry out electrochemical reactions in poorly conducting media. However, following the rigorous mathematical analysis of the potential distribution at the interface of bipolar electrodes by Duval and co-workers in 2001, bipolar electrochemistry has emerged as a powerful technique for electroanalysis and surface patterning. It is particularly the lack of direct electrical connection to the bipolar electrode that makes the technique quite unique. This aspect has facilitated electroanalysis in miniaturized systems such as capillary electrophoresis where microelectrodes are employed and the high electric fields in the separation channel often lead to fluctuations in the potential of the working electrode, making it difficult to control electrochemical reactions.

The variation in the potential difference along the interface of a bipolar electrode makes bipolar electrochemistry a very straight forward technique for decorating substrates with chemical gradients that can be used, for example, to screen chemical or physical phenomena or to drive certain transport processes. Even more interesting is the possibility to control the position, width and shape of the gradients by simply changing the electric field in solution. The simplicity of the instrumentation used to create these gradients makes bipolar electrochemistry an inexpensive alternative to lithographic techniques for gradient formation.

Chapter 1 gives a brief introduction to traditional electrochemistry. It describes the experimental setup for carrying out electrochemical reactions and how these reactions can be

controlled. The fundamental principles of bipolar electrochemistry are also presented in this chapter and its advantages over traditional electrochemistry are stated. It also reviews recent applications of bipolar electrochemistry in areas such as device fabrication, micromotors, analyte enrichment and detection in microfluidic devices, and surface patterning. Finally, a review of spectroelectrochemistry is presented, focusing on Raman spectroscopy.

In chapter 2, basic measurements to provide insight into the potential profile in a bipolar electrochemical setup are presented. The bipolar effect is also demonstrated experimentally using copper deposition as an example. The existence of a potential gradient along a bipolar electrode is demonstrated by evaluating the reactivity gradient on Au and Ag electrodes modified by a self-assembled monolayer (SAM) of a thiol-functionalized quinone upon the application of an electric field. In situ Raman microscopy is used to characterize the gradient. The ability to control the position and width of gradients formed on bipolar electrodes is also demonstrated.

In chapter 3, the applications of cobalt oxide are briefly reviewed. Preparation of cobalt compounds involving different oxidation states of the metal is also reported. Its catalytic, optical and electrochromic properties are investigated using cyclic voltammetry and Raman microscopy.

In chapter 4, a one-dimensional chemical compositional gradient of a cobalt oxide electrocatalyst for water oxidation is displayed on a bipolar electrode. The composition of the material gradient composition is screened using in situ Raman microscopy while its catalytic activity is investigated using Scanning electrochemical microscopy (SECM), leading to the identification of the active phase.

In chapter 5, similar studies in chapter 4 are reported for nickel oxide water oxidation catalyst and comparism between both catalysts is made.

Chapter 6 gives a summary of this dissertation and a quick overview of future projects.

Acknowledgements

I am forever grateful to Dr Curtis Shannon for accepting to be my advisor in the first place. Without him I wouldn't have had this great opportunity to pursue my graduate studies at Auburn University and enjoy all the facilities that it offers. I also address my deepest gratitude to him for his relentless motivation and continuous guidance during the course of studies in the department of Chemistry and Biochemistry. I thank all my committee members, Dr Vincenzo Cammarata, Dr Chistopher Easley and Dr ZhongYang Cheng for their valuable suggestions and constructive criticism that contributed to the success of my research. I particularly thank Dr Minseo Park for helping me with the analysis of Raman data and also for accepting the outside reader for my dissertation.

I thank Dr Rik Blumenthal for his help with powder X-Ray Diffraction (XRD) measurements and Dr Michael Miller for helping me with Scanning Electrochemical Microscopy measurements.

I would also like to thank all my group members Dr Chaokang Gu, Dr Weiping Li, Dr Sridevi Ramakrisnan, Dr Tanyu Wang, Mrs Yajiao Yu, Mr Sanjun Fan, Mrs Li Zhang and Mrs Apu Mazumder for their helpful discussions concerning my research and life in general. I give special thanks Rajakumari Ramaswamy from whom I learnt a lot as far as electrochemistry is concerned.

I appreciate the wonderful staff of the Chemistry and Biochemistry department for their great services.

Finally I would like to thank my family and friends for their moral support during my graduate studies. Special thanks to my parents for all the sacrifices they have made my upbringing in general and in my education in particular. I thank my sister Christelle and my sister-in-laws Edith and Elizabeth for care they provided to my daughters Melissa and Serena each time I was away. I also want to sincerely thank my husband, Fidele, for his unconditional love and constant supporting throughout my study at Auburn.

Table of Contents

List of Figures

Chapter 1

Introduction to Electrochemistry

1.1 The Power of Electrochemistry

Electrochemistry involves the use of electricity to effect chemical transformations (electrolysis) as well as the production of electricity from chemical reactions (energy conversion and storage) [1-6]. Electricity was first observed in chemical systems by Luigi Galvani in 1791. He noticed that a dead frog's leg "kicked" when its muscle was touched with the terminals of simple circuit consisting of two dissimilar metals. At a time when very little was known about electricity, Galvani believed a force within the frog was responsible for the activation of its muscle. He termed this force "animal electricity". However, by replacing the animal tissue with paper soaked with salt water, Alessandro Volta argued that electricity wasn't intrinsic to animals but that the electricity originated from the metals used to contact the animal tissue and that the tissue simply served as a path (electrolyte) for transporting the electricity. Volta further demonstrated that the magnitude of the electricity, and therefore the degree of muscle activation depended on the dissimilarity between the two metals used to sandwich the muscle. Today, Volta can be credited for the discovery of the electromotive force (EMF) and the electrochemical series. The electrochemical series is a series in which metals are listed according to their ability to accept or give up electrons, thereby producing electrical current. By connecting several of these metal/paper/metal sandwich-like structures in series, Volta built the first electric battery in 1800. Therefore, today's quest for emission free vehicles, that is, those powered by fuel cells is based

on an idea that dates back about two centuries. William Nicolson and Anthony Carlisle would later use Volta's battery to perform one of the most significant experiments in the history of chemistry - the decomposition of water into oxygen and hydrogen using the electricity generated from the battery. Not only did this experiment give insight into chemical bonding as would be elaborated on by Gilbert Lewis but it did revolutionalize the industrial sector as it provided a simple and inexpensive method for large scale production of substances such as chlorine and aluminum. In 1834, Michael Faraday empirically elucidated the basic principles and quantitative relationships for the electrochemical phenomena, whereby he related the amount of electricity to the extent of electrochemical reactions. Faraday's relationship relates to electrochemistry in the same way that Beer's law relates to spectroscopy. Building on this foundation, electrochemistry has emerged as a powerful analytical tool thanks Jaroslav Heyrovsky whose work on the discovery and development of polarographic methods of analysis earned him the Nobel Prize in Chemistry in 1959. He has also been called the father of electroanalytical chemistry. In polarography, the metal in contact with the electrolyte is Mercury although other metals can be used. A potential difference is applied across a metal/electrolyte/metal system and the resulting current is measured.

Chemical transformations such as water splitting are at the heart of chemistry. Whether such transformations are effected using electricity or some other means such as light or heat, the experimentalists all have the same goal at the end - to elucidate the mechanism of the transformation and therefore control the extent of the reaction. This is particularly important for the synthetic chemist because it allows him to employ routes that would give him the maximum yield of a specific product. According to Arrhenius' equation the best way to control a chemical reaction is to change the temperature. Another common method is to adjust the concentration of

the reacting species or to employ a catalyst. All three parameters, namely temperature, concentration and the use of catalysts to control reactions have similar effect on electrochemical reaction as they do on chemical reactions in general. However, for electrochemical reactions, there exists an additional and very powerful means of controlling the rate of a reaction. It involves adjusting the (electric) potential of the electrochemical system. Theoretically, increasing the potential of a system by 1V may increase the reaction rate by several orders than raising the reaction temperature by $100^{O}C$. This can be attributed to the fact that the electrical potential is directly related to the energy of the electrons which are the main reactants in electrochemical reactions. In analytical electrochemistry, we control or adjust the potential of the system in order to isolate the process giving rise to a signal. By doing so, it is possible to determine the composition of the system as well as the amount of each component. For electrochemical devices such as batteries, the contributing processes are optimized with the goal of enhancing the performance of the device. The development of modern electronic instrumentation as well as computers with powerful data-processing and computational capabilities has revolutionized electrochemistry in this regard. For example potentiostats allow precise control of the potential applied to an electrochemical system and measures the current resulting from the reaction very accurately. They are also very sensitive and can measure current down to the nanoampere range.

Another major development in the field of electrochemistry was the discovery scanning electrochemical microscopy (SECM) which allows microscopic surface areas to be probed. This technique has been successful due to the development of ultramicro electrodes from which the analytical current is generated. The electrode scanned across the surface the electrode of interest using piezo controllers. Unlike the traditional electrochemical setup where the measured current is the collective response from reactions on the electrode surface, SECM offers lateral resolution

about the state of the electrode. It can therefore be useful in identifying active sites on the surface of an electrode and has been used as a high throughput technique for screening electrocatalyst candidates.

1.2 Definition of Terms

Because electrochemistry involves interaction between charged species, it will be useful to define some of the terms often used to describe the behavior of electrical charges in general.

1.2.1 Electric force

The force F, exerted by a source charge, Q_2 on a test charge, Q_1 is given by Coulomb's law

$$F = \frac{1}{4\pi\varepsilon_0\varepsilon}\frac{Q_1\,Q_2}{r^2} = K\,\frac{Q_1\,Q_2}{r^2} \qquad 1.2.1$$

where Q_1 and Q_2 have units of Coulombs C, where 1 C is the amount of charge on 6.24 x 10^{18} electrons.

r is the distance between the charged substances

ε_0 is the permittivity of free space (= 8.85 x 10^{-12} C^2/Nm^2)

ε is the dielectric constant of the medium between the charged substances.

K is a proportionality constant known as the Coulomb's law constant

The force, of course, is the vector along the direction of both charges.

1.2.2 Electric field

The magnitude of the electric field is simply defined as the force per unit charge at certain point

$$Electric\ field, E = \frac{Force, F}{Charge, Q} \qquad 1.2.2$$

Therefore the electric field strength experienced by the test charge Q_1 due the source charge Q_2 is given by

$$E = \frac{F}{Q_1} = K \frac{Q_1 Q_2}{r^2} \frac{1}{Q_1} = K \frac{Q_2}{r^2} \qquad 1.2.3$$

Notice that E is independent of Q_1. Therefore, the electric field strength measured at any given location around the source charge, Q_2, will be the same irrespective of the test charge. By convention the direction of the electric field is from the positive charge to the negative charge.

1.2.3 Electrical potential energy

In general, charged species respond to an electric field by moving in a direction that will annul the effect of an electric field. The electrical potential energy at a point in an electric field E is defined as the work, W done against the electric field in order to bring of a test charge Q_1 from a reference location (usually infinity) to that point.

$$U(r) = -W = \int_{\infty}^{r} F.dr = \int_{\infty}^{r} K \frac{Q_1 Q_2}{r^2} dr = K \frac{Q_1 Q_2}{r} \qquad 1.2.4$$

1.2.4 Electric potential

The electric potential, ϕ at a point in an electric field is the electric potential energy per unit at that point. It is therefore the work required to move a unit charge

$$Electric\ potential, \phi = \frac{Electric\ potential\ energy,\ U}{Charge, Q} \qquad 1.2.5$$

According to equation 1.2.4 it is therefore the work required to move a unit charge from infinity to that point.

$$\phi(r) = -\frac{W}{Q_1} = -\frac{1}{Q_1}\int_{\infty}^{r} \frac{Q_1 Q_2}{r^2}\, dr = -K\frac{Q_2}{r} \qquad 1.2.6\ a$$

By differentiating equation 1.2.6, we obtain the following expression

$$\frac{\partial \phi(r)}{\partial r} = -K\ \frac{Q_2}{r^2} \qquad 1.2.6\ b$$

The quantity on the right hand side of equation 1.2.6a is the same as the electric field, E according to equation 1.2.3. We can therefore rewrite equation 1.2.6a as

$$-\frac{\partial \phi(r)}{\partial r} = E \qquad 1.2.7$$

That is, the electric field can also be described as the negative gradient of the electrical potential.

1.3 The Electrochemical Reaction.

Electrochemical reactions occur as a result of the transfer of electrons between two chemical phases: an electronic conducting phase called the electrode and an ionic conducting phase called the electrolyte. The transfer of electrons occurs solely at the boundary or interface between the electrode and the electrolyte. The electrode-electrolyte interface is therefore of fundamental

importance in electrochemistry because its structure and composition has a direct consequence on the behavior of electrochemical reactions.

When a metal, M, is dipped in a solution containing the metal cation, M^{n+} an equilibrium is established according to the equation

$$M \leftrightharpoons M^{n+} + ne^{-} \qquad 1.2.8$$

where n is the number of electrons lost by the metal to form the cation.The situation is demonstrated in figure 1.3.1 with a Zn metal dipped in a aqueous solution of $ZnSO_4$. Some of the Zn atoms in the metal dissociate into Zn^{2+} ions which go into solution. The electrons resulting

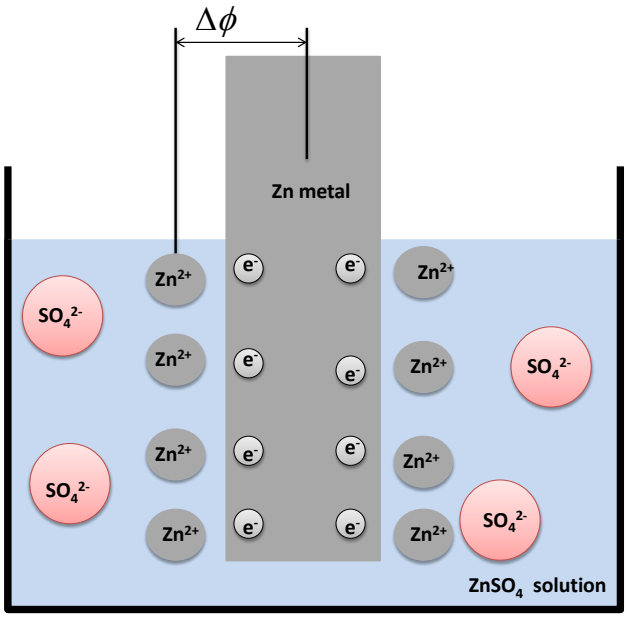

Figure 1.3.1. When a piece of Zn metal (electrode) is dipped in an aqueous ZnSO4 solution (electrolyte), a small amount of the Zn atoms in the metal goes into solution as Zn^{2+}, leaving behind the electrons on the Zn electrode. The charge buildup on the electrode and the solution leads to a potential difference of about 1V between the electrode and the solution.

from the dissociation remain on the Zn the metal. In electrochemistry, the setup shown in figure 1.3.1 is referred to as *a half cell* while the reaction occurring at the electrode-soution interface is referred as the *half cell reaction*. As a result of the charge separation at the interface, a potential difference, $\Delta\phi$, develops between the metal and the solution creating an electric field which tends to oppose further dissociation and therefore the transfer of Zn^{2+} ions from the metal across the interface into the solution. In order to move this system away from equilibrium, that is, push more Zn^{2+} ions into the solution or cause the Zn^{2+} ions already in solution to deposit on the metal as Zn atoms, an external force must be applied to the system. In electrochemistry, a power supply (potentiostat), connected to the system is used to apply an external potential to the system and the current resulting from the transfer of charges across the interface is recorded. That is, it is possible to construct a potential-current plot for a given system and such a plot can provide useful information about the system. Information obtained from such plots include, the amount of material reacted, which is related to the amount of charge transferred. Information about the kinetics and thermodynamics of the system can also be obtained from such electrochemical studies.

It is rather inconvenient to work with single half cell like the one shown in figure 1.3.1. Therefore electrochemical experiments are usually performed using a setup consisting of at least two half-cells. Moreover, $\Delta\phi$ for a single interface cannot be determined directly although changes in its value can be easily measured. For example if the half cell in figure 1.3.1 is connected to another half cell undergoing the opposite reaction i.e. a deposition reaction, a potential difference, E which is the sum of the potential differences across both interfaces can be measured using a high resistance voltmeter as shown in figure 1.3.2. The magnitude of E is a

measure of the work required to drive electrons externally between the Zn and Cu electrodes. The current due to the flow of electrons through the external wire can be measured and related to the extent of the reaction. The salt bridge is usually made of a saturated solution of a highly conducting electrolyte such as KNO_3 and provides electrical connection between the solutions in the two half cells. This prevents accumulation of ions in both half cells that would otherwise prevent further electrochemical reactions. As shown on figure 1.3.2, the electrode at which species get oxidize is called the *anode* while the one at which species get reduced is called the *cathode*.

The potential difference, $\Delta\phi$, that develops at the interface between the metal and the solution is about only about 1V. Although this may seem like a very small voltage, its effect on redox reactions occurring at that interface can only be appreciated if the distance over which the potential difference exists is considered - about 10^{-8}cm. This corresponds to an electric field strength (or potential gradient) of 10^{6}V/cm. This enormous field strength is strong enough to alter the structure and reactivity of species at the interface. It is over this distance, extending over a region called the *electrical double layer*, that all electrochemical reactions take place. A direct effect of $\Delta\phi$ on electrochemical reactions is that changes in its value influence the relative electron affinities of species in the electrode and electrolyte thereby controlling the direction of reaction.

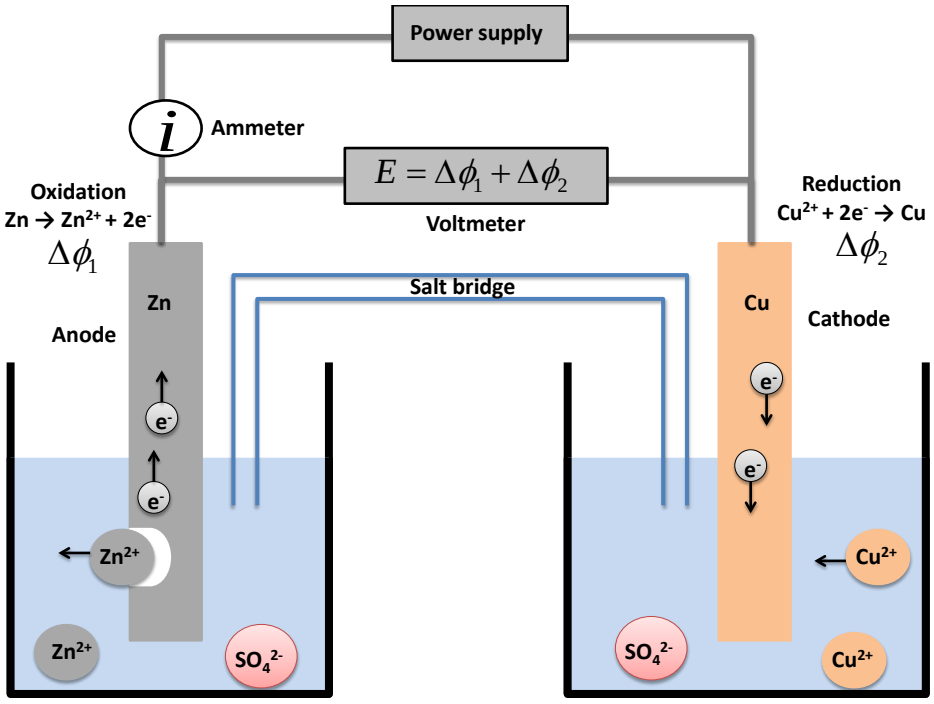

Figure 1.3.2. An electrochemical cell consisting of two electrodes: an anode where oxidation reactions take place and a cathode where reduction reactions take place. A power supply is used to drive reaction in the desired direction while the ammeter and voltmeter allow measurement of current and potential that can be related to the extent of reaction.

Usually, one is interested in the reactions occurring at a single electrode. This electrode is called the working electrode (WE). To ensure that the changes in the value of E are only due to the electrode of interest, i.e. the WE, E is rather measured against a second electrode called the reference electrode (RE) as shown in figure 1.3.3.This electrode is designed such that the potential difference at its interface, $\Delta\phi_{RE}$ remains constant during the experiment. In order to keep $\Delta\phi_{RE}$ constant, no significant current must go through the RE because if it did, there will be a charge redistribution at its interface thereby changing the value of $\Delta\phi_{RE}$. Therefore, the

current resulting from reactions at the WE flows through a third electrode called the counter electrode (CE). The internationally accepted reference electrode is called the *normal hydrogen electrode (NHE)* and has been assigned a potential difference of 0V.

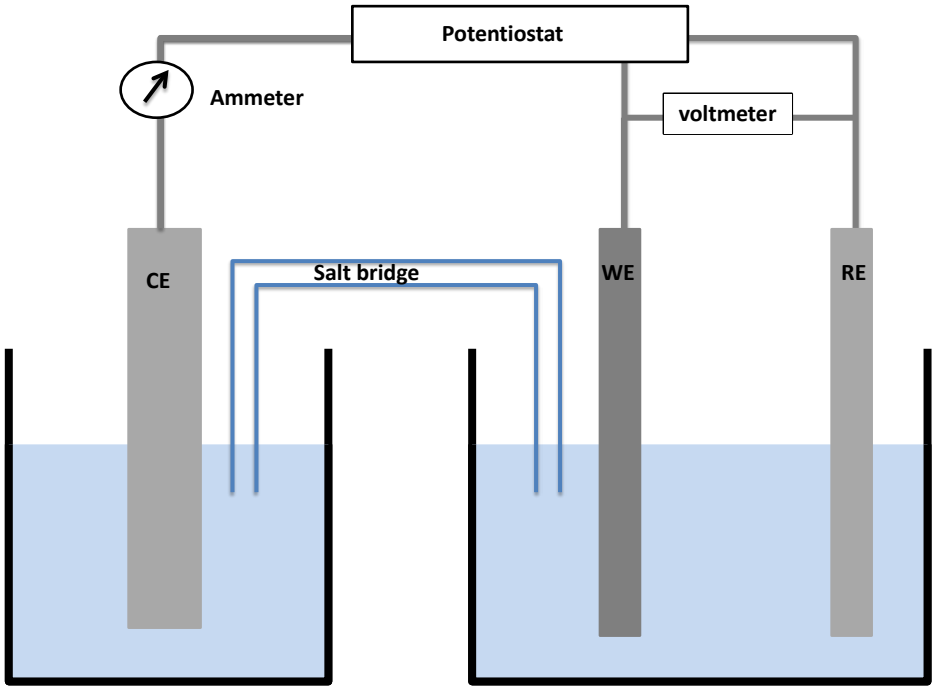

Figure 1.3.3. An electrochemical cell consisting of three electrodes: a working electrode (WE) which is the electrode of interest, a counter electrode through which current from the WE flows and a reference electrode (RE) against which the potential of the WE is controlled. A power supply is used to drive reaction in the desired direction while the ammeter and voltmeter allow measurement of current and potential that can be related to the extent of reaction.

1.4 Controlling the Direction of Electrochemical Reactions

Since the value of $\Delta\phi_{RE}$ remains constant during the experiment, any changes in E must be attributable to reactions occurring at the WE. Therefore, one observes changes in the interfacial potential difference, $\Delta\phi_{WE}$,of the WE with respect to the RE. It was mentioned above that the

direction of electron transfer across the electrode-solution interface is controlled by changes in the potential difference $\Delta\phi$ across the electrode-solution interface. One way to change $\Delta\phi$, is to change the potential of the electrode by connecting an external power supply as shown in figure

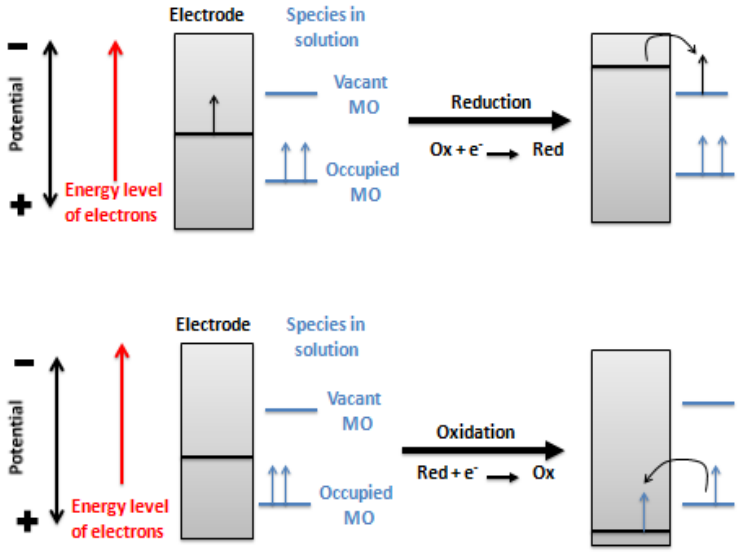

Figure 1.4.1. Reduction **a)** and oxidation **b)** reaction involving solution species Ox and Red respectively as a result of changes in the electrode potential.

1.3.4, to the electrochemical cell with one of the terminals attached to the electrode (working electrode). For example if the negative terminal of the power supply is connected to the working electrode, its potential will be more negative compared to that of the solution. As a result, the Because negatively charged particles flow in the direction of positive potential, the electrons in the electrode will transfer to the species present in the solution shown in figure 1.3.4a. This corresponds to *a reduction reaction*. The flow of electrons from the electrode to the solution results in a *reduction* current that can be measured and related to the amount of species reduced,

according to Faraday's law. On the other hand, if the electrode is connected to the positive terminal of the powers supply, its potential becomes more positive relative that of the solution. In this case, electrons will transfer from species in the solution onto the electrode as shown in figure 1.3.4b. This corresponds to an *oxidation reaction.* Hence, *oxidation* current that is related to the amount of species oxidized will flow through the cell.

1.5 Introduction to Bipolar Electrochemistry

It was mention earlier that electrochemical reactions occur as a result of charge transfer across the electrode-solution interface and that the driving force for the electron transfer is the difference between the potential of the electrode and that of the solution. In the traditional electrochemical set up, the potential of the electrode is controlled against that of the solution relative to a reference electrode by injecting electrons in or out of the electrode using a potentiostat. Because the excess charge is distributed uniformly across electrode surface, the potential will be the same at every point on the electrode and we have an equipotential surface. As a result, reactions will occur uniformly across the surface of the electrode. In *bipolar electrochemistry*, electrochemical reactions occur on a conducting substrate that has no physical contact to the power supply as shown in figure 1.5.1. Due to the lack of electrical contact between the electrode and the power supply, its potential cannot be controlled and therefore adjusts to the potential of the surrounding solution. Moreover the substrate acts as a *bipolar electrode (BPE),* that is, an electrode that acts simultaneously both as an anode and as a cathode. The principles of bipolar electrochemistry have been described quantitatively[7-10]. The experimental configuration of a bipolar electrochemi cal cell is shown in figure 1.5.1a.

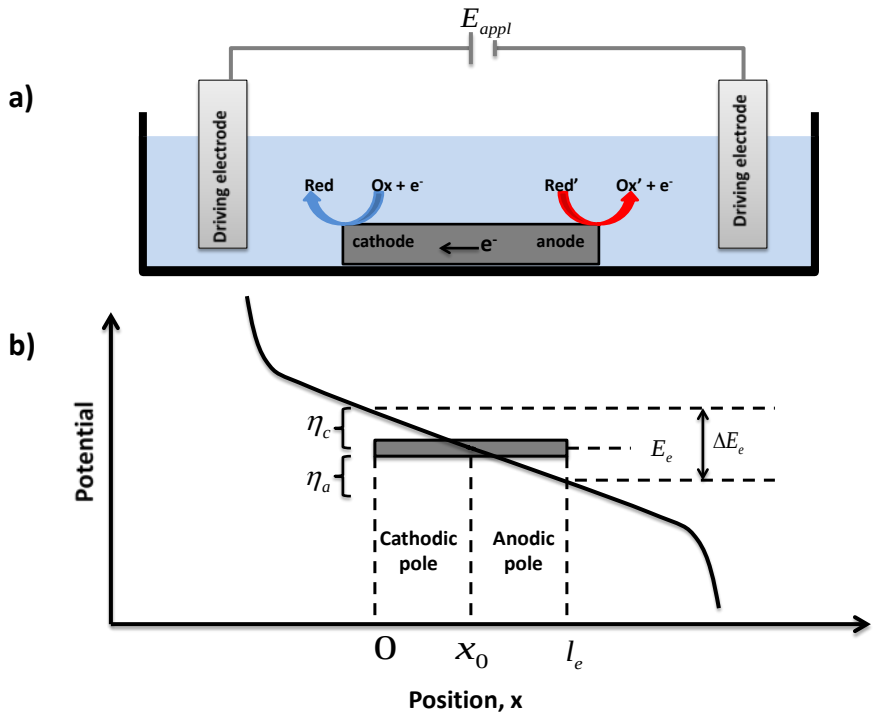

Figure 1.5.1 A bipolar electrochemical cell consisting consisting of two driving electrodes between which a voltage, E_{appl}, is applied and a bipolar electrode (BPE) where faradaic reactions at both ends **a)** and the cell geometry showing the origin of the cathodic and anodic overpotentials **b).**

A voltage, E_{appl}, is applied between two driving electrodes across the solution. Because of the solution's resistance, the potential drops, first exponentially near the diving electrodes and then approximately linearly in the center of the solution. This implies that the potential difference between a point on the substrate and the solution will vary laterally along the surface. When the applied voltage E_{appl} is sufficiently high, faradaic reactions will be initiated at both ends of the bipolar electrode – anodic reaction on end and cathodic reactions on the other. According to a recent quantitative description of BPEs by Duval and coworkers[1] there exists a single point on

the BPE where it's potential equals that of the solution. This point, at which no reactions occur, divides the BPE into two poles; the cathodic and anodic poles. The potential at this point, E_e corresponds to the potential that the BPE will adopt in the absence of E_{appl}. When E_{appl} is applied across the solution, the fraction of it dropped over a distance in solution corresponding to the length of the length, l_e, of the bipolar electrode is given by

$$\Delta E_e = V\, l_e = \frac{E_{appl}}{l}\, l_e \qquad 1.5.1$$

where V is the electric field in solution and l is the distance between the driving electrodes. ΔE_e represents the total potential difference between the bipolar electrode and the solution overpotential needed to drive two faradaic reactions occurring simultaneously on opposite poles of the bipolar electrode i.e. $\Delta E_e = \eta_c - \eta_a$. Note that the symbol η denotes a potential difference and can also be referred to as an overpotential. For two redox reactions to occur simultaneously at the opposite ends of the bipolar electrode, ΔE_e must be at least equal to the difference between the formal potentials of the two redox couples involved. Equation 1.5.1 indicates that for a given value of E_{appl}, a higher value of ΔE_e can be attained by using a longer bipolar electrode or by reducing the distance between the driving electrodes.

The potential difference or overpotential between a point, x ,on the electrode and the solution is given by

$$\eta_{(x)} = E_{(x)} - E_e = V\,(x - x_0) = \frac{\Delta E_e}{l_e}\,(x - x_0) \qquad 1.5.2$$

where x_0 is the position on the bipolar electrode between the anodic and cathodic pole at which the solution potential equals the equilibrium potential, E_e of the substrate. This point, at which no reactions occur, divides the BPE into two poles; the cathodic pole for which $E_{(x)} > E_e$ and the anodic pole for which $E_{(x)} < E_e$. Note that it is necessary that the reactions at both pole to occur simultaneously to maintain electroneutrality on the electrode surface. That is the electrons generated at the anodic pole due to an oxidation reaction must be consumed in a reduction process at the cathode

1.6 Applications of Bipolarelctrochemistry

Although the phenomenon of bipolar electrochemistry was first described several years ago, it was exploited mainly for industrial applications such as electrosynthesis to reduce electrical connection and power dissipation in external cirtcuits[11-16], solar cells[17-19], batteries[20, 21] and fuel cells[22]. Recently, the field has received considerable attention in the areas of analytical chemistry, surface patterning, material science, electronic device and macro- and microswimmer development.

One attractive feature of bipolar electrodes is the fact that the electrode under investigation is not physically connected to the external power supply. This allows electrochemistry to be carried out on micrometer-sized electrodes as first demonstrated by Fleischman et al. [14, 15]. The concept of using bipolar electrochemistry in the area of electronic devices was pioneered by Bradley and coworkers. They demonstrated the formation of electrical contact between particles[23-28]. In this experiment, two micrometer-sized copper particles were aligned between two Pt driving electrodes that were dipped into water. Upon application of a voltage between the driving

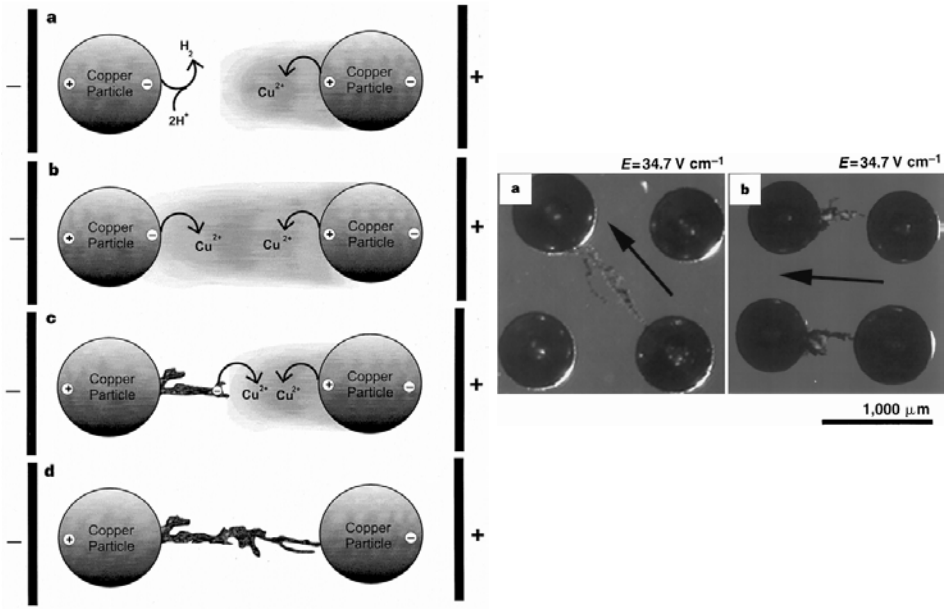

Figure 1.6.1 (Left) Diagram of wire formation between two particles under bipolar conditions. **a)** Two copper particles are placed in an aqueous environment and an electric field is applied. The polarization of each particle is shown. Initially the particle on the right liberates copper ions while the particle on the left reduces water. The shaded area represents a hypothetical distribution of the ionic cloud. (For clarity only the phenomena in the interparticle region are shown). **b)** When the copper-ion concentration near the particle on the left is high enough electrodeposition occurs and the wire begins to grow on the side facing the other particle. **c)** Electrodeposition occurs preferentially at the wire tip where cathodic polarization is expected to be highest. **d)** When the wire reaches the particle on the right, electrical contact is made. At this point there is no potential difference between the particles and electrochemical processes in the interparticle region cease. (Right) Control of wire growth within a 4× 4 particle array. **a)** The applied electric field was along the diagonal of the copper particle array (indicated by the arrow) generating a single wire in the expected location. The other two particles were left unaffected. **b)**

The applied electric field vector was parallel to the side of the particle array (arrow) generating two parallel wires. [Reprinted with permission from Bradley, J-C.; Chen, H. M.; Crawford, J.; Eckert, J.; Ernazarova, K.; Kurzeja, T.; Lin, M.; Mcgee, M.; Nadler, W.; Stephens, S. G. *Nature* **1997,** 389, 268-271. Copyright © 1997, Rights Managed by Nature Publishing Group]

electrodes, an electric field was generated in the solution. Because of the variation of potential in the solution one particle acts as an anode while the other acts as the cathode. This leads to the oxidation of copper to Cu^{2+} ions on one particle and the reduction of water on the other particle. The Cu^{2+} ions begin to accumulate in the space between the two particles reaching a point where its reduction back to Cu metal starts to compete with water reduction on the cathode. The continuous electrodeposition of Cu results in the growth of the metal in the direction of the field and towards the anode. When the Cu "wire" has grown enough to span the gap between the cathode and the anode, electrical contact is made between the two particles. The progress of the Cu wire formation is shown in Figure 1.6.1(left). Figure 1.6.1(right) shows that by changing the direction of the electric field in the solution, connections can be made between selected particles. This ability to control the direction of the wire growth provides a very simple and inexpensive method of constructing three-dimensional microcircuits compared to photolithography and imprint technologies. It has been shown that by using less polar solutions such as organic solvent higher electric fields[26] could be reached in the solution, allowing nanosized particles[25] to be used.

This group [29-32] has also exploited the phenomenon of bipolar electrochemistry to enhance the surface area of electrodeposited catalysts. In this work[29], graphite particles were immobilized on one side of cellulose paper, a stack of which was sandwiched between two driving electrodes

dipped into a 1mM organic solution of $PdCl_2$. In this case each particle simultaneously acts as the anode and cathode allowing Pd to be selectively deposited on the cathodic side. Unlike in traditional electrochemistry where the amount of catalyst is limited to the surface of the working electrode, bipolar electrochemistry allows the catalyst to deposit over several centimeters on the support. In addition to graphite particles, this group has demonstrated the modification of other materials such as carbon nanofibers, carbon nanotubes[31] and carbon nanopipes[32].

In the experimental setup proposed by Bradley's group, the size of the particles to be modified is limited to the submicrometer scale due the high electric field that is required for smaller particles. Building upon their work the group of Kuhn has developed a method that allows the modification of object even in the nanometer range[33-38]. In this method, a setup (figure 1.6.2, left) for capillary electrophoresis is employed. The driving electrodes are placed in two separate compartments, one of which contains the deposition solution. Both compartments are connected with a capillary filled with a suspension of the substrate to be modified. Upon application of an electric field, the substrate is transported due to electroosmotic flow from the capillary end in the anodic compartment towards the end in the cathodic compartment where Ni is deposited[34] as shown in Figure 1.6.2, right. The flow of species is monitored by measuring the UV absorbance of the passing solution. The advantage of this technique is that the particles to be modified are not immobilized. Therefore there is no limit to the number of "Janus" particles that can be made. In addition, the use of a capillary electrophoresis setup allows higher electric fields to be attained due to the high resistance of the capillary channel. By attaining such high electric fields, particles in the nano-scale can be modified using the phenomenon of bipolar electrochemistry.

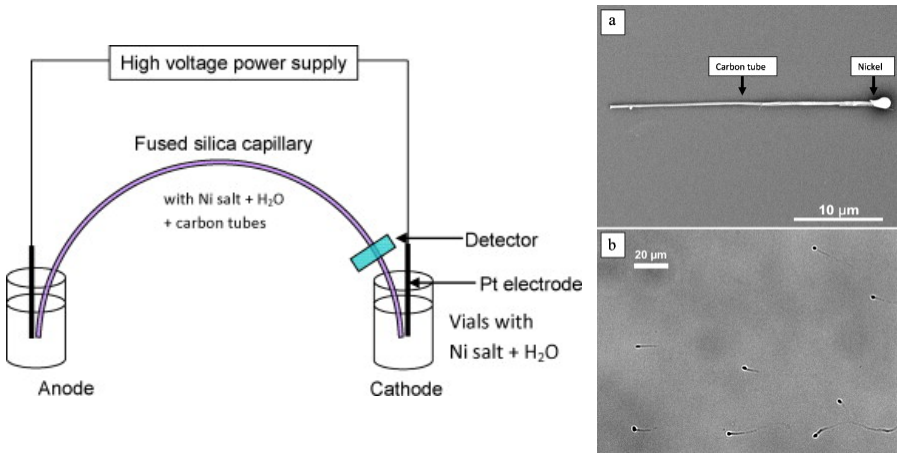

Figure 1.6.2 (Left) Schematic illustration of the capillary electrophoresis set-up used in this study. (Right) Site selective bipolar electrodeposition of nickel at one end of a carbon tube **a)** electron microscope image of a selected tube from a diluted sample and **b)** optical microscope image of an ensemble of nickel modified tubes still suspended in the aqueous solution. [Reprinted with permission from Loget, G.; Larcade, G, Lapeyre, V.; Garrigue, P.; Warakulwit, C.; Delville, M. H.; Ravaine, V.; Kuhn, A. *Electrochim. Acta* **2010,** 55, 8166-8120. Copyright © 2010, Elsevier]

Another area that is currently exploiting the bipolar effect is the development of micro- and nanoobjects[39-46] that can move in response to an external stimulus. Such objects have potential applications ranging from micropumps and drug delivery to microfluidic devices and assembly of microstructures. Unlike other methods that have been employed to induce motion in the so

called “swimmers”, bipolar electrochemistry is simple and does not require the use “fuel”. It only takes advantage of any asymmetry created around an object acting as a bipolar electrode. The motion of the object can therefore be controlled by adjusting the strength and direction of the electric field. The use of bipolar electrochemistry in developing microswimmers has the advantage that any object, as long as it is conductive can be used as a swimmer. Shortly after the group of Bradley[39] demonstrated that material dissolution and deposition can occur simultaneously on opposite ends of immobilized metallic particle, the groups of Sen and Mallouk demonstrated that freely suspended bimetallic Pt/Au nanorods can be propelled in solution by simultaneous oxidation and reduction of H_2O_2 at the Pt and Au ends, respectively[40].

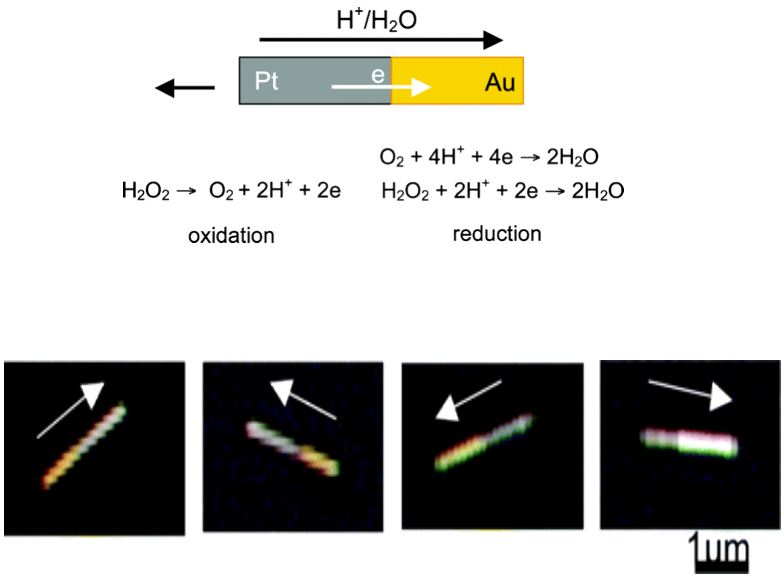

Figure 1.6.3 (Top) Bipolar Electrochemical Decomposition of H_2O_2 at a Pt−Au Nanorod. In the electrokinetic mechanism, H^+ moves from the anode end to the cathode end of the rod, resulting in nanorod motion in the opposite direction. We find that whereas the electrokinetic mechanism

is essentially correct the dominant cathode half reaction is actually oxygen reduction rather than H_2O_2 reduction. (Bottom) Optical images of (left to right) NiAu, AuPd, AuRu, and RhPt nanorods. The direction of motion is indicated by the arrow in each case. [Reprinted with permission from Wang, Y.; Hernandez, R. M.; Berrtlett, D. J.; Bingham, J.M.; Kline, T. R.; Sen, A.; Mallouk, T. E. *Langmuir* **2006,** 22, 10451-10456. Copyright © 2006, American Chemical Society]

They described an electrokinetic propulsion mechanism whereby the H^+ ions produced from the oxidation of hudrogen peroxide at the anodic end of the Pt/Au rod migrate towards the cathode resulting in a corresponding movement of the rod in the opposite direction as shown in Figure 1.6.3 (top). Several metallic combinations were tested and the optical images of various bimetallic rods and the direction of motion are shown in Figure 1.6.3 (bottom).

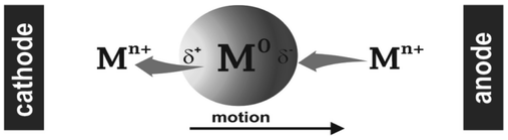

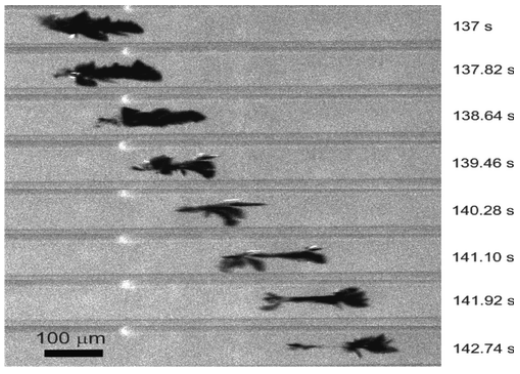

Figure 1.6.4 (Top) Dynamic Bipolar Self-Regeneration Principle. (Bottom) Optical micrographs of a zinc dendrite in a glass capillary filled with a zinc sulfate solution at pH ≈ 5 under the influence of an external electric field. [Reprinted with permission from Loget, G.; Kuhn, A. *J. Am. Chem. Soc.* **2010,** 132-15918-15919. Copyright © 2010, American Chemical Society]

Kuhn's group[41-46] has been very active in this area. First[41] they demonstrated the propulsion of Zn dendrites at a speed of 60µms^{-1}in an electrophoresis capillary containing Aqueous $ZnSO_4$. In this work the dendrites moved in the direction opposite to electroosmotic flow and their morphology appeared to be changing in the course of the movement as shown in Figure 1.6.4, indicating that the transport of the dendrites was due to a dynamic bipolar self-regeneration and not by electroosmosis as in the work of Sen and Mallouk and coworkers. In a later work[42],

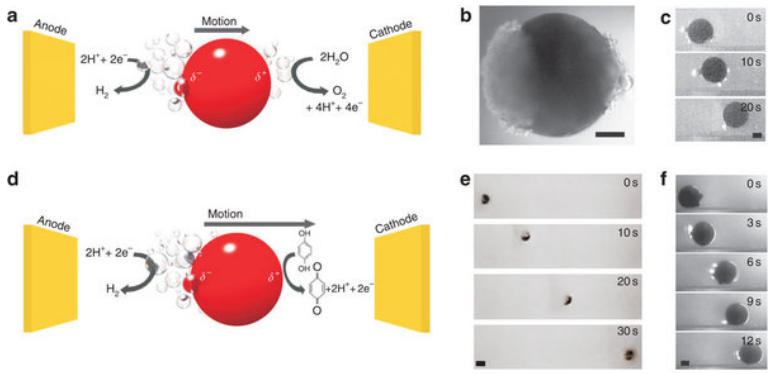

Figure 1.6.5 a–c) Competing bubble production. **a)** Scheme of the water splitting by bipolar electrochemistry. **b)** Optical micrograph of a stainless steel 1 mm spherical metal particle

exposed to a 1.6 kV m^{-1} electric field in aqueous 24 mM H_2SO_4. The left part of the bead is the cathodic pole where H_2 bubbles are produced and the right part is the anodic pole where O_2 bubbles are produced. Scale bar, 250 μm. **c)** Translational motion generated with a 285-μm glassy carbon sphere in a PDMS microchannel exposed to a 5.3 kV m^{-1} electric field in aqueous 7 mM H_2SO_4. Scale bar, 100 μm. **d–f)** Quenching of O_2 bubble production. **d)** Scheme of proton reduction and HQ oxidation. **e)** Translational motion generated on a 1-mm stainless steel bead exposed to a 1.3 kV m^{-1} electric field in 24 mM HCl and 48 mM HQ. Scale bar, 1 mm. **f)** Translational motion generated with a 275-μm glassy carbon sphere in a PDMS microchannel with a 4.3 kV m^{-1} electric field in an aqueous solution of 7 mM HCl and 14 mM HQ. Scale bar, 100 μm. [Reprinted with permission from Loget, G.; Kuhn, A. *Nat. Commun.* **2011,** 2, 535. Copyright © 2011, Rights Managed by Nature Publishing Group]

Kuhn's group demonstrated another mechanism for micro-object propulsion in the presence of an electric field. In this experiment simultaneous oxidation and reduction of water to produce oxygen and hydrogen bubbles respectively on opposite ends of the bipolar object. The volume of oxygen produced at the anodic end is twice that of hydrogen produced at the cathodic end. This uneven production of bubbles around the object results in hydrodynamic forces at the surface of the object that results in a direct movement of the object in a direction towards the cathode as shown in Figure 1.6.5. By designing suitable bipolar electrochemical rotors, the authors were able to achieve rotational movement in addition to linear movement.

In an effort to tract the movement of these micro-objects, the group of Sojic in collaboration with the Kuhn's group replaced the oxidation of water on the anodic side of the objects by an

electrochemical reaction which can result in electrogenerated chemiluminescence (ECL)[46]. This replacement is possible because the nature of electrochemical reactions on bipolar electrode is not critical as long as electroneutality is maintained on its surface. In this experiment $[Ru(bpy)_3]^{2+}$ and tri-n-propylamine (TPrA) were oxidized on the anodic side of the particle to produce the ECL while water was reduced on the cathodic side to produce hydrogen bubbles. This asymmetric electroactivity as a result of bipolar effect results in a simultaneous motion and emission of light by the bipolar object as shown in figure 1.6.6 (left). The progress of the object in a U-shaped glass tube was monitored by taking optical images at different times as shown in figure 1.6.6 (right). The inset shows the height of ECL and therefore the height traveled by the object as a function of time.

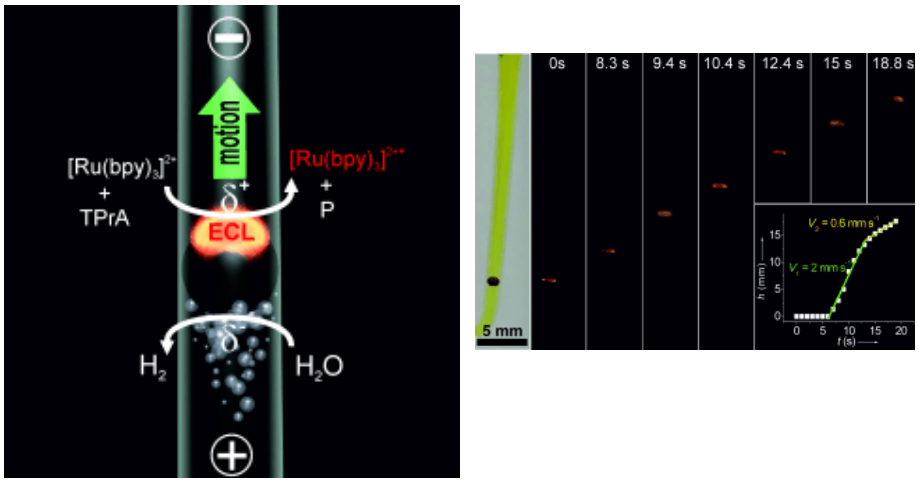

Figure 1.6.6 (Left) Asymmetric light-emitting electrochemical swimmer. Simultaneous reduction of H_2O at the cathodic pole (bottom of the bead) and oxidation of ECL reagents at the anodic pole (top of the bead) induces both motion and light emission from the bead in a glass capillary. P corresponds to a side product of the TPrA radicals formed during the ECL process. (Right) Levitation of a light-emitting GC bead. Series of optical images showing a GC bead emitting ECL at different times during its motion. The bead was placed in a U-shaped cell, filled with 100 mM PBS buffer containing 0.5 mM $[Ru(bpy)_3]^{2+}$, 100 mM TPrA, and a few drops of surfactant. It was exposed to an external electric field of 25.5 V cm^{-1}. The left image was taken under white light and the other images were taken in the dark. Inset: Plot showing the change in height *h* of the bead as a function of time *t*. [Re printed with permission from Sentic, M.; Loget, G.; Manojlovic, D.; Kuhn, A.; Sojic, N. *Angew. Chem. Int. Ed.* **2012,** 11284-11288. Copyright © 2012 WILEY-VCH Verlag GmbH & Co. KGaA, Weinheim]

Because bipolar electrodes are not physically connected to the external instrumentation, their use for analytical purposes can be very challenging due to the lack of any means to monitor reactions on the electrode. Therefore the combination of bipolar electrochemistry with a reporting scheme such as ECL is critical for its implementation in sensing applications [47-58]. When such a combination is successful, bipolar electrodes can provide means, for example, of integrating electrochemical detection schemes in miniaturized analytical devices such as on-chip capillary electrophoresis where high electric fields makes it difficult to control the potential of the working electrode in the traditional three-electrode setup[59]. Manz and coworkers first reported use of ECL generated from a BPE as a detection scheme for analytes present in a microfluidic system[47]. In this work a microfabricated U-shaped Pt BPE was placed across a

capillary electrophoresis separation channel, with its legs acting as anode and cathode. The voltage required to drive electrochemical reactions on both legs was derived from the electric field used in the channel for the separation of different amino acids. The cathodic reaction was H_2O reduction while ECL was generated at the anodic leg. Because the ECL observed was as a result of a reaction between [Ru(bpy)3]$^{2+}$ and the amino acids being separated, the emission of light signaled the presence of the analytes. The Manz approach is, however, limited in the sense that only analytes acting as co-reactansts for [Ru(bpy)3]$^{2+}$ can be detected. Shortly after their report, Crooks' group[48-54] demonstrated that a larger variety of compounds could be detected using the ECl technique based on bipolar electrochemistry. This was accomplished by taking advantage of reactions occurring at both poles of the bipolar electrode. Specifically, the reduction of an analyte at the cathodic pole was signaled by the emission of light due to the oxidation of [Ru(bpy)3]$^{2+}$ and the common co-reactant, TPrA, at the anodic pole. Using this technique the authors first reported the detection of benzyl viologen[48] and other molecules[49, 50]. Recently, the technique has been extended to detect biologically relevant molecules such DNA[51-52], RNA[53], membrane-bound proteins such as folate receptors[54] and tumor biomarkers such as prostate-specific antigen[55].

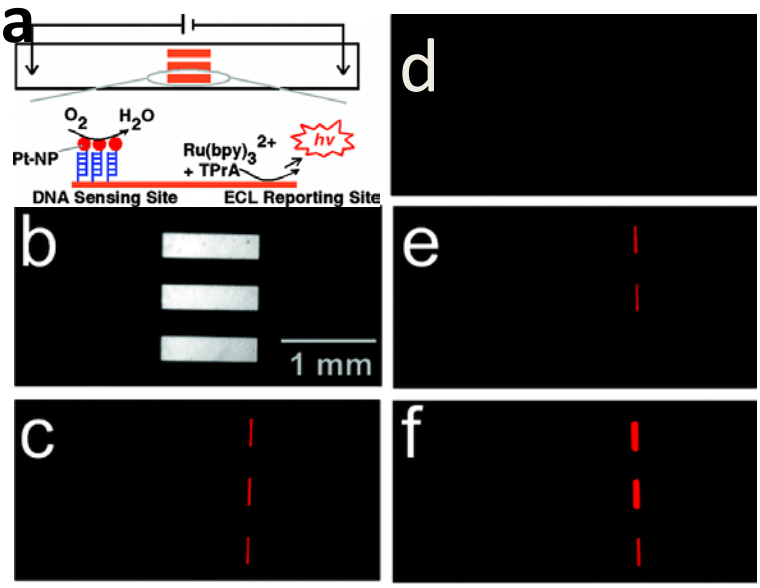

Figure 1.6.7 a) Top-view schematic illustration of the microdevice. **b)** Optical micrograph of the bipolar electrode configuration used to obtain the data in the other panels of this figure. False-color luminescence micrographs showing **c)** the ECL emitted at E_{tot} = 16.0 V when complementary target DNA functionalized with Pt-NPs is hybridized to probe DNA present on the electrode surface; **d)** no ECL emitted at 16.0 V prior to hybridization; **e)** the ECL emitted at 16.0 V when only the top two electrodes of the device are exposed to the labeled target; and **f)** the ECL emission at E_{tot} = 22.0 V for the device in **e)**. [Reprinted with permission from Chow, K-F.; Mavre, F.; Crooks, J.; Chang, B-Y.; Crooks, R. M. *J. Am. Chem. Soc.* **2009,** 131, 8364-8365. Copyright © 2008, American Chemical Society]

Figure 1.6.7a shows the DNA detecting scheme proposed by Crook's group. To demonstrate that the detection process can be made to scale, the authors use three bipolar electrodes made of gold microbands. Prior to assembling the device, the gold bipolar electrodes are modified with thiol-

functionalized DNA probes. After incubation in a solution containing the target DNA that has been functionalized with Pt nanoparticles (figure 1.6.7b) the electrode array is then placed in a microfluidic channel filled with a solution containing $[Ru(bpy)_3]^{2+}$. Upon application of a voltage, red light emission was observed at the anodic pole of all three electrodes due to ECL as shown in Figure 1.6.7c. The ECL observed at the anodic pole is correlated to oxygen reduction at the cathodic pole catalyzed by Pt-NP that was attached target DNA. Thus the emission of light signaled the DNA hybridization. In the absence target, no ECL was observed as shown in figure 1.6.7d. When only the top two of the three electrodes were exposed to the target DNA, no ECl was observed on the bottom electrode as shown in figure 1.6.7e. Figure 1.6.7f shows that when the applied voltage was increased from 16 to 22V, ECL, even though with a lower intensity, light emission could be observed even on the bottom electrode that was not exposed to the target DNA. This is because at such high voltage the oxygen reduction occurs on the bare gold electrode without the help of the Pt-NP catalyst. This group further demonstrated that ECl can be simultaneously emitted from the anodic poles of microarray of 1000 bipolar electrodes. The fact that only two driving electrodes is required to control an array of electrodes demonstrates the simplicity of a bipolar electrochemical setup. This ECL detection scheme has also been used to screen an array of elctrocatalyst[55]. To avoid interference between the ECL reporting cocktail and the analyte solution, a two-channel design for ECL sensing has been reported[56, 57] whereby the anodic and cathodic poles of the bipolar electrode are housed in separate microfluidic channels.

Crooks's group has reported quantitative studies on this bipolar electrochemistry based ECL sensing scheme[57]. Using a split bipolar electrode with the ends connected to an ammeter as shown in scheme… below, a linear correspondence between the ECL intensity at the anodic pole and the rate of reaction at the cathodic pole. More importantly, the measured ECL intensity and

the current through the bipolar electrode were in good agreement with values calculated based on the kinetics of the electrochemical reactions. This kind of split bipolar electrode design for direct measurement of the current passing through the bipolar electrode was first reported by Nyholm and coworkers for the detection of electroactive molecules in a capillary electrophoresis[60] and also in an on-chip microfluidic device[61].

Crooks' group has reported another bipolar electrochemistry-based sensing scheme that is based on the dissolution of the bipolar electrode itself[62].

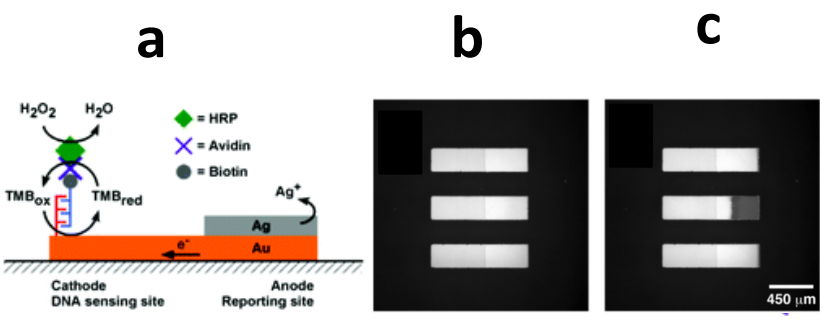

Figure 1.6.8 a) Schematic representation of sensing device. **b)** Optical micrographs of the DNA-sensing device showing (middle) DNA-modified and (top and bottom) thiol-modified electrodes **b)** before and **c)** after E_{tot} = 12.0 V was applied for 90 s. [Reprinted with permission from Chow, K-F.; Chang, B-Y.; Zaccheo, B. A.; Mavre, F.; Crooks, R. M. *J. Am. Chem. Soc.***2010,** 132, 9228-9229. Copyright © 2010, American Chemical Society]

Because the anodic and cathodic reactions on the bipolar electrode must occur at the same rate, the reduction of an analyte at the cathodic pole triggers the dissolution of the bipolar electrode at the anodic pole. In this report, a layer of Ag was deposited on the anodic pole of the bipolar electrode prior to carrying out the sensing experiment. When a voltage was applied, reduction of an analyte molecule at the cathodic pole led to the dissolution of the Ag layer at the anodic pole as shown in figure 1.6.8a. Specifically, the cathodic pole of middle BPE in figure 1.6.8b was first modified with a thiol-functinalized DNA probe. All three electrodes were then exposed to biotin-labeled complementary target DNA and then to avidin-labeled Horseradish peroxidase (HRP). The electrodes were finally placed in a microfluidic channel filled with a solution containing hydrogen peroxide and tetramethylbenzidine (TMB). HRP catalyzes the reduction of hydrogen peroxide while simultaneously oxidizing TMB. Upon application of a voltage across the channel, the oxidized TMB is reduced at the cathodic pole. This reduction process triggers the oxidation of Ag at the anodic pole as shown in the optical micrograph in figure 1.6.8c. Note that there was no Ag dissolution in the top and bottom electrode that was not modified with the probe DNA. Therefore, the Ag dissolution served as a signal for DNA hybridization. Because the Ag dissolution can be observed with the naked eyed, this technique serves as a simple and inexpensive detection scheme. Moreover, the reduced length of the BPE provides a permanent record of the state of the BPE. This detection scheme has recently been used to screen and array of electrocatalysts[63]. In this report three candidates, namely Pt, Indium-doped tin oxide (ITO) and Au, were deposited at the cathodic pole of three bipolar electrodes while the anodic pole consisted of Ag microbands as shown in figure 1.6.9a. The extent of catalytic reduction of oxygen at the cathodic poles of the BPE was correlated to the number of dissolved Ag microbands after a given period.

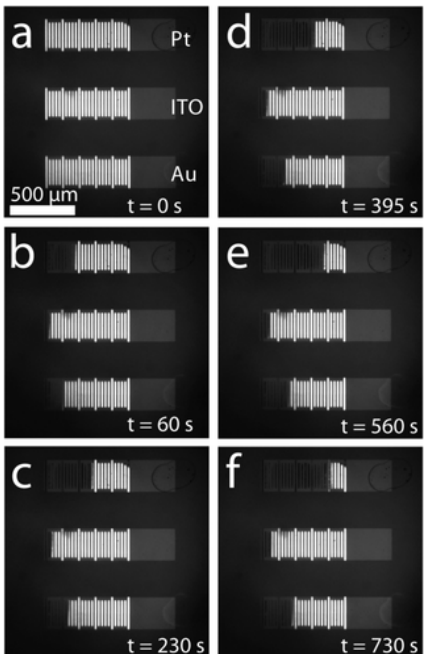

Figure 1.6.9 a) Optical micrograph of three BPEs. The top BPE was spotted with G6-OH(Pt_{225}), the middle BPE was naked ITO, and the bottom BPE was modified with G6-OH(Au_{225}). The BPEs were placed in a microfluidic channel consisting of a silicone gasket and a poly(dimethylsiloxane) block. The channel was 12.5 mm long, 3 mm wide, and 0.5 mm tall and filled with air-saturated 0.10 M acetate buffer (pH 4.0). Two Ag/AgCl electrodes were used to apply E_{tot} **b–f)** Micrographs of the three BPEs after application of E_{tot} for the indicated times. E_{tot} was 10.0 V for the first 60 s of the experiment and 4.0 V thereafter. No further Ag electrodissolution was observed after 730 s (f). [Reprinted with permission from Fosdick, S. E.; Crooks, R. M. *J. Am. Chem. Soc.* **2011,** 134, 863-866. Copyright © 2012, American Chemical Society]

Because of the miniaturized nature of lab-on-a-chip analytical devices, the volume of analytical samples that can be used is usually in the micro- and nanoliter range. This corresponds to very small amounts of (10^{-9} to 10^{-12} mol) of the analyte to be detected. In order to improve the concentration detection limits that can be achieved in these devices, preconcentration or concentration enrichment of the analyte is required prior to separation and detection. In capillary or microchip electrophoresis, preconcentration is achieved mainly by using buffers of various concentration or composition in order to create an electric field gradient. However, this procedure is time consuming and prone to errors even though when done precisely, enrichment factors of up to 1000 can be attained[64]. Yeung and coworkers[65] reported for the first time the use of bipolar electrochemistry to preconcentrate analyte compounds without the need of buffer discontinuity. It has already been mentioned that the high electric fields present in electrophoresis channels make them a very suitable environment for working with bipolar electrodes. In their work, a Pt bipolar electrode was inserted inside the electrophoresis channel and electrolysis of water at the ends of the electrode led to the production of H^+ and OH^- ions. As these ions begin to diffuse across the channel a pH gradient is generated at the extremities of the electrode. As the analytes molecules traverse the gradients their electrophoretic mobilities are affected as they get charged, leading to their accumulation. Crooks group[66-72] has recently explored concentration enrichment techniques that are also based on bipolar electrochemistry. In their preliminary work[66, 67], a Au bipolar electrode was place in a mirofluidic channel containing a low concentration Tris-HCl buffer. The production of OH^- ions at the cathodic pole of the BPE led to the neutralization of the buffer ions. This resulted in gradient in ionic strength at the end of the bipolar electrode that generated an electric field gradient as shown in figure 1.6.10 (top and

middle). The behavior of an anionic fluorescent molecule called BODIPI disulfonate was monitored in the channel. BODIPI initially enters the

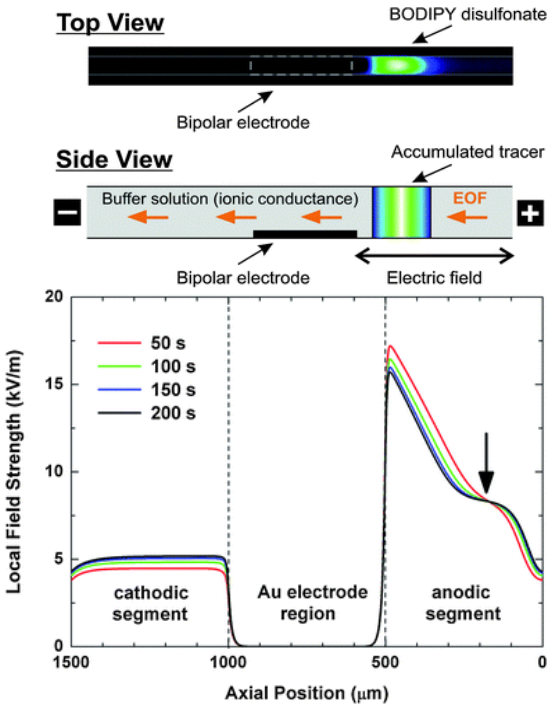

Figure 1.6.10 (Top) Optical fluorescence micrograph of the microchannel with the embedded Au electrode. The micrograph shows the concentration distribution of BODIPY disulfonate in 1 mM Tris–HCl buffer at pH 8.1 after applying a potential bias of 30 V for 240s. (Middle) Schematic illustration of the proposed mechanism of tracer accumulation in the microchannel with a bipolar electrode. (Bottom) Simulated profiles of the local axial electric field for t = 50, 100, 150, and 200 s. Applied field strength: 5 kV m^{-1}. Initial tracer concentration, c_0 = 5 μM. Profiles represent the distribution of field strength along the geometrical axis of the channel (y = 10 μm). [Reprinted from Hlushkou, D.; Perdue, R. K.; Dhopeshwarkaer, R.; Crooks, R. M.; Tallarek, U. *Lab Chip* **2009,** 9, 1903-1913.]

by electroosmotic flow but as it encounters the increasing field gradient generated at the end of the bipolar electrode, its electrophoretic mobility towards the anode anode begins to increase. The analyte molecules begin to accumulate in the region where the two mobilities balance each other as shown in figure 1.6.10 (top). By using split bipolar electrodes this group has been able to study the effect of current through the bipolar electrode on distribution of analyte molecules in the channel[68, 69]. In order to preconcentrate cations using this technique, the authors modified the walls of the microfluidic channel so as to reverse electroosmotic flow[71]. In addition to concentration enrichment this technique has been used for analyte separation in a microfluidic channel[72] based on electrophoretic mobility. The use of bipolar electrodes to preconcentrate and separate analytes provides a very simple method of improving the sensitivity of analyte detection in microfluidic systems. It can therefore be expected to compete with current methods such as the use of buffer discontinuity.

Another growing area of bipolar electrochemistry is the exploitation of the discontinuity in the interfacial potential difference (figure 1.6.1) along the surface of the bipolar electrode to pattern surfaces with chemical gradients[73-79]. This due to the fact that the driving force for electron transfer, and therefore the extent of redox reactions, varies along the surface of the bipolar electrode.The group of Bjorefors first reported the use of bipolar electrochemistry to patterned electrode surfaces. Their preliminary work demonstrated the existence of a potential gradient along the surface of a bipolar electrode[73]. Specifically, a bipolar electrochemical cell containing a gold bipolar electrode was filled with a solution containing a mixture of $[Fe(CN)_6]^{4-}$ and $[Fe(CN)_6]^{3-}$. Upon application of a electric field across the solution, $[Fe(CN)_6]^{4-}$ was oxidized to $[Fe(CN)_6]^{3-}$ at the anodic pole of the electrode while $[Fe(CN)_6]^{3-}$ was reduced to $[Fe(CN)_6]^{4-}$at the cathodic pole. These reactions resulted in changes in refractive index of the solution close to

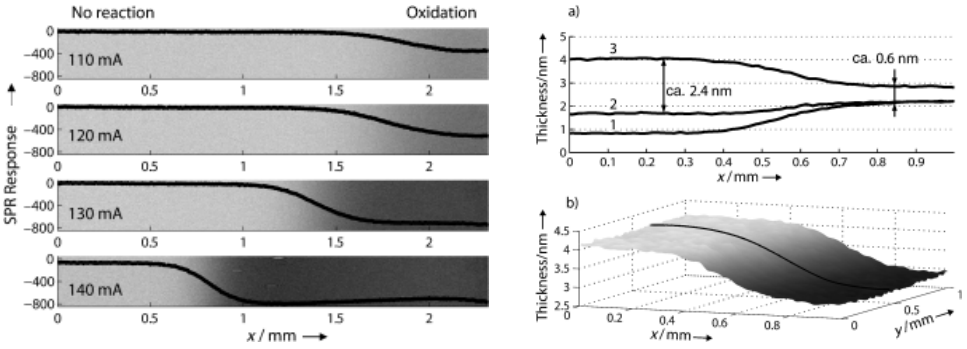

Figure 1.6.11 (Left) Changes in the SPR response owing to the change in the refractive index when $[Fe(CN)_6]^{4-}$ is oxidized to $[Fe(CN)_6]^{3-}$ (at different total currents). The lines show the mean intensity change in the SPR images. (Right) **a)** Line profiles, obtained from imaging-null-ellipsometry measurements, in which the thicknesses of the gradients observed after the different preparation steps are shown. Line 1 exhibits the result of the desorption of mPEG, line 2 shows that obtained after backfilling with aPEG, and line 3 represents the resulting protein gradient. **b)** Thickness map of the protein gradient (the line shows the region from which the line profile was taken). [Reprinted with permission with from Ulrich, C.; Anderson, O.; Nyholm, L.; Bjorefors, F. *Angew. Chem. Int. Ed.* **2008,** 47, 3034-3036. Copyright © 2008 WILEY-VCH Verlag GmbH & Co. KGaA, Weinheim]

the surface of the bipolar electrode. Because the potential and therefore the extent of reaction is different at each position along the electrode, the refractive index varied accordingly. The change in surface plasmon resonanance (SPR) resulting from changes in the refractive index was measured as a function of position as shown in figure 1.6.11(left).The various plots indicate how the position and width of the gradient change with different applied current. These results highlight a very important feature of using bipolar electrochemistry to create surface gradients which is the use of very simple and inexpensive instrumentation to control the position and width of surface gradients[75, 76]. In order to demonstrate the use of bipolar electrochemistry as a straight forward technique for patterning surfaces with gradients in chemical properties, the authors used a gold substrate that had been previously modified with a self assembled monolayer (SAM) of a methoxy-labeled thiol (figure 1.6.11, right, line 1). The thiol was then selectively desorbed at the cathodic pole of the SAM-modified gold electrode by passing a current through the driving electrodes (figure 1.6.10, right, line 2). The electrode was then backfilled with a carboxy-labeled thiol The carboxy group serve as a functionalization site for proteins. Finally the electrode was incubated in a solution containing lysozme to make a protein gradient (figure 1.6.10, right, line 3) Yutaka and coworker have reported bipolar patterning of conducting polymeric materials such as poly(3-methylthiophene) (PMT), poly(aniline) (PANI) and poly(3,4-ethlenedioxythiophene) using a doping technique[76, 77] and "click" chemistry[78]. Shannons group[79] has prepared a chemical composition gradient of CdS on a gold bipolar electrode by electrodeposition.

1.7 Raman spectroelectrochemistry

In order to obtain a more complete analysis about the state of an electrode and the nature of the species produced on its surface, electrochemistry is often coupled with spectroscopic techniques such as UV-VIS absorption, Ellipsometry, electron paramagnetic resonance (EPR) spectroscopy and vibrational spectroscopy. Whereas UV-VIS spectroscopy requires the use of optically transparent electrodes, EPR spectroscopy is limited only to species with unpaired electrons. Therefore vibrational spectroscopy such as IR and Raman are commonly used to provide structural information about electrogenerated species. Of the two vibrational techniques, Raman spectroscopy has received little attention in the past due to the inherent inefficiency of the scattering effect – only 1 in 1,000,000 photons that interact with the sample give rise to a Raman shift. The use of intense light sources such as lasers and highly sensitive detectors such as charge coupled devices (CCD) have been employed to improve the detection limit in Raman spectroscopy. Also, using an excitation light in the visible and near infrared region of the spectrum in makes it convenient to couple Raman spectroscopy with electrochemistry in the sense that the glass cells and aqueous solutions used in electrochemistry are do not absorb light in this region. This is in contrast to IR spectroscopy because IR radiation is strongly absorbed by these materials.

It has been shown that the intensity of Raman signal can be improved by selecting a light source whose wavelength corresponds to an electronic transition in the analyte molecule. This technique is called *resonance raman spectroscopy (RRS)* and can result in 10^4 to 10^6 enhancement factors[80]. This technique has been used to study the electrochemical doping and dedoping processes of polypyrole (PPy) with dodecylbenzenesulfonate (DBS)[81].

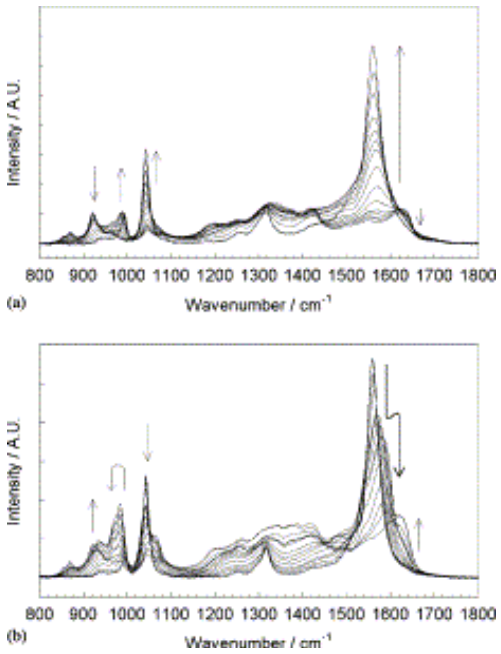

Figure 1.7.1 Overlaid Raman spectra (514.5 nm excitation, background corrected) for **a)** the reduction from +0.5 to −0.9 V and **b)** oxidation from −0.9 to +0.5 V of a cycled PPy/DBS film in deaerated 0.1 M $NaClO_4$. [Reprinted from Crowly, K.; Cassidy, J. *J. Electroanal. Chem.* **2003,** 547, 75-82. Elsevier]

Figure 1.7.1 shows the changes in the Raman spectra corresponding to structural changes in the polymer upon incorporation of the DBS cations present in the electrolytic solution. By selecting excitation lasers of appropriate frequencies, the authors were able to distinguish contributions of the neutal, cationic and diacationic forms of the polymer to the Raman spectra.

Another technique used to improve the intensity of Raman signals is called *surface enhanced Raman spectroscopy (SERS).* In this method the analyte molecules are absorbed onto pre-activated substrates. The substrates, typically Ag, Au, and Cu, are activated by formation of nanostructures on their surfaces. These nanostructures are capable of increasing the local electric

field of the excitation and scattered radiation through surface plasmon waves[82, 83]. In addition to the enhancement resulting from the surface plasmon waves, the Raman signal in SERS is further enhanced by charge-transfer between the analyte molecule and the substrate. The SERS technique is limited to species residing within nanometers of the substrate due to the exponential decay of the surface plasmon waves[84]. Therefore, SERS spectroelectrochemistry is limited to species absorbed on electrode surface or those residing within the double layer. An example of a SERS spectroelectrochemical study involves the potential-dependent tautomerization of a metal complexing ligand, *p*-((8-hydroxyquinoline)azo)benzenethiol (SHQ) adsorbed on a Ag electrode[85]. Figure 1.7.2 shows SERS spectra that were recorded as a function of applied potential from 0.0 to -0.4V vs Ag/AgCl in a electrolytic solution containing Cu^{2+} ions. At 0.0V, the adsorbed SHQ is present on the electrode surface mainly as the enol azo tautomer which is reactive towards Cu^{2+} ions. However, at potentials negative of -0.3V the unreactive keto-hdrazone tautomer is strongly favored and is characterized by the appearance of a carbonyl (C=O) stretching mode at 1642cm^{-1}.

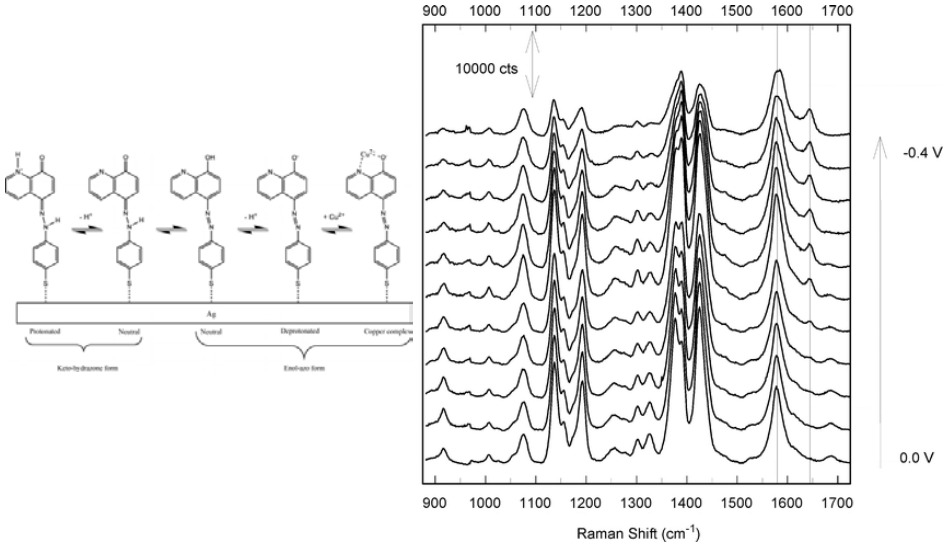

Figure 1.7.2 (Left) Tautomeric forms of p-([8-hydroxyquinoline]azo)benzenethiol (SHQ). (Right) In situ SERS spectra of SHQ immobilized at highly polished Ag electrode surfaces as a function of applied potential (V vs Ag/AgCl). These spectra were background subtracted and offset for plotting, but are not normalized. The unique ν(C = O) peak at 1642 cm^{-1} from the keto−hydrazone tautomer is noted, along with the ν(C = C) at 1580 cm^{-1}, which remains constant with changes in the tautomer populations. [Reprinted with permission from Oklejas, V.; Uibel, R. H.;Horton, R.; J. M. *Anal. Chem.* **2008**, 80, 1891–1901. Copyright © 2008, American Chemical Society]

A recent innovation in the Raman instrumentation is the coupling of a conventional Raman spectrometer to an optical microscope, allowing the characterization of microsized samples. The so called *Raman microprobe spectrometry* or simply *Raman microscopy* has been used to

characterize electrogenerated species at microelectrodes (radius in the 10μm range) where the low concentration of species produced can be otherwise difficult to detect. In this work[86] the electrochemical oxidation of 9,10-dichloroanthracene (DCA) to produce a radical cation, $DCA^{+\cdot}$, was recorded as a function of applied potential in a solution containing 5mM DCA and 0.1M

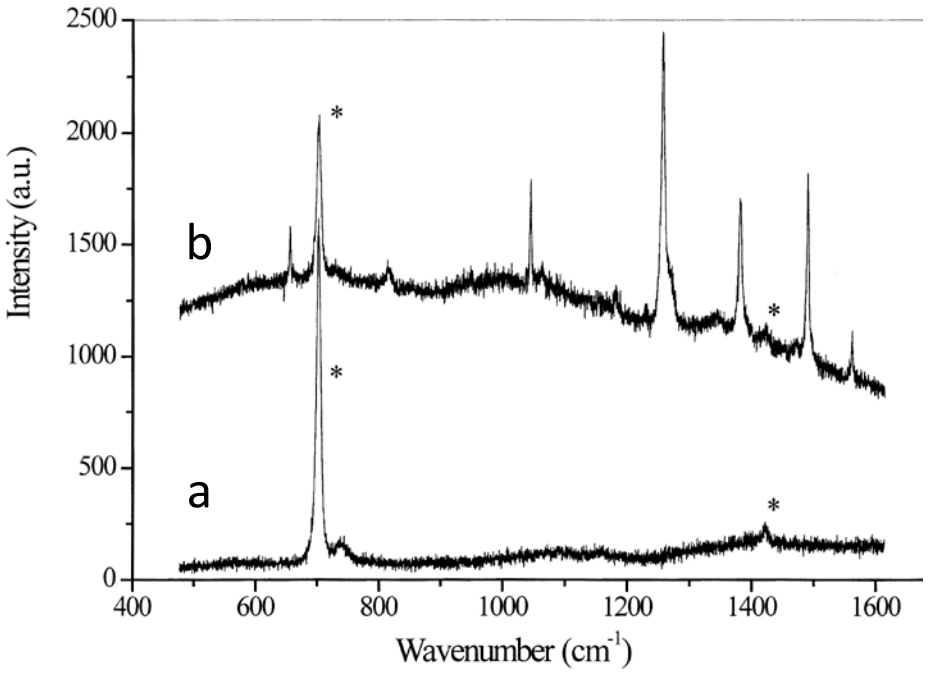

Figure 1.7.3 Raman spectra of DCA in CH_2Cl_2/0.1 mol L^{-1} Bu_4NBF_4 on a gold microelectrode at **(a)** 0 V vs Ag and **(b)** 1.7 V vs Ag. Integration time was 180 s, λ_{exc} = 647 nm, and *P* = 2.4 mW. [Reprinted with permission from Régis, A.; Hapiot, P.; Servagent-Noinville, S. *Anal. Chem.* **2000,** 72, 2216-2221. [Copyright © 2000, American Chemical Society]

Tetrabutylammonium tetrafluoroborate (Bu_4NBF_4) in CH_2Cl_2. Figure 1.7.3A shows the spectrum at 0.0V where no radical cation is produced while Figure 17.3B shows the spectrum the cation produces at 1.7V vs Ag.

Although Raman spectroscopy cannot be used to test catalytic activity directly, it has been found to be very sensitive to the state of metal oxide electrocatalyst. The Raman spectra of these oxides highly dependent on the oxidation state of the metal[87]and are particularly sensitive to structural and phase changes[88, 89]. Raman microscopy has been used to monitor structural and compositional changes in electrode materials for rechargeable Li ion batteries upon the charge/discharge process[90, 91]. The cathode material in these batteries is commonly made of $LiCoO_2$. The performance of the electrode material is known to reduce upon protracted cycling or prolonged storing. This lost of performance is accompanied by a change in the morphology of the $LiCoO_2$ due to lithium disintercalation as

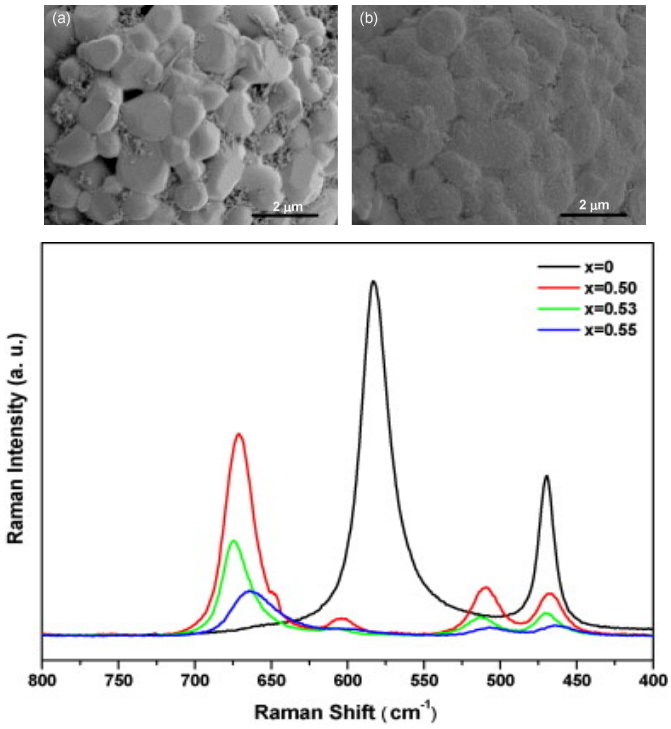

Figure 1.7.4 (Top) SEM image of pristine **a)** and delithiated $Li_{1-x}CoO_2$ (x = 0.50) particles **b)**. (Bottom) Raman spectra of $Li_{1-x}CoO_2$ (x = 0, 0.50, 0.53 and 0.55).[Reprinted from Park, Y.;

Kim, N. H.; Kim, J. Y.; Eom, I-Y.; Jeong, Y. U.; Kim, M. S.; Lee, M. L.; Choi, H. C.; Jung, Y. M. *Vibrational Spectroscopy* **2010,** 53, 60-63.]

shown in figure 1.7.4A[91]. The degradation process is given by the equation

$$LiCoO_2 \rightarrow Li_{1-x}CoO_2 + xLi^+ + xe^- \quad 1.3.1$$

$$3LiCoO_2 + Li^+ + e^- \rightarrow Co_3O_4 + 2Li_2O \quad 1.3.2$$

Figure 17.4 (bottom) shows the Raman spectra of pristine $LiCoO_2$ as well as delithiated $Li_{1-x}CoO_2$. The pristine $LiCoO_2$ exhibits two strong features at 470cm^{-1} and 582cm^{-1}. Upon removal of Li, new features appear at about 510cm^{-1} and 673cm^{-1} that can be assigned to the formation of Li_2O and Co_3O_4.

Finally, combining the Raman spectrometer with a confocal microscope instead of the convential optical microscope leads to spatial resolution of about 1μm which provides an excellent tool for characterizing homogeneity and stoichiometry on the micrometer scale of electrodeposited films.

References

1) Bard, A.B.; Faulkner, L. R. *Electrochemical Methods: Fundamentals and Applications*, 2nd ed., Wiley and Sons, New York, **2001**
2) Bockris, J. O'M.; Redddy, A. K. N. Modern *Electrochemistry 1: Ionics,* 2nd ed., Plenum Press, New York, **1998**
3) Bockris, J. O'M.; Redddy, A. K. N.; Gamdoa-Aldeco, M. *Modern Electrochemistry 1: Fundamentals of Electrodics,* 2nd ed., Kluwer Accademic/Plenum Press, New York, **1998**

4) Bockris, J. O'M.; Redddy, A. K. N. *Modern Electrochemistry 1: Electrodics in Chemistry, Engineering, Biology and Environmental science,* 2nd ed., Kluwer Accademic/Plenum Press, New York, **1998**

5) Gileadi, E. *Physical Electrochemistry: Fundamental, Techniques and Applications,* Wiley and sons, New York, **2011**.

6) Engel, T.; Reid, P. *Physical Chemistry,* 2nd ed., Pearson, **2010.**

7) Duval, J.; Klein, J. M.; van Leeuwen, H. P. *J. Electroanal. Chem.* **2001,** 505, 1-11.

8) Duval, J. F. L.; van Leeuwen, H. P.; Cecilia, J. Galceran, J. *J. Phys Chem. B* **2003,** 107, 6782-6800.

9) Duval, J. F. L.; Minor, M.; Cecilia, J.; van Leeuwen, H. P. *J. Phys Chem. B* **2003,** 107, 3143-4155.

10) Planar D.; Jones, F. G. E.; Dryfe, R. A. W. *J. Electroanal. Chem.* **2010,** 646, 107-113.

11) Eardley, D. C.; Handley, D.; Andrew, P. S. *Electrochim. Acta.* **1973,** 18, 339-848.

12) Goodridge, F.; King, C. J. H. *Electrochim. Acta.* **1977,** 22, 347-352.

13) Goodridge, F.; King, C. J. H.; Wright, A. R. *Electrochim. Acta.* **1977,** 22, 1087-1091.

14) Fleischmann, M.; Ghoroghchian, J.; Pons, S. *J. Phys. Chem.* **1985,** 89, 5530-5536.

15) Fleischmann, M.; Ghoroghchian, J.; Rolison, D.; Pons, S. *J. Phys. Chem.* **1986,** 90, 6392-6400.

16) Picket, J.D. *Electrochemical Reactor Design, 2nd ed.,* Elsevire Scientific Publishing.; New York, 1979; p34.

17) Smotkin, E.; Bard, A. J.; Campion, A.; Fox, M. A.; Mallouk, T.; Webber, S. E.; White, J. M. *J. Phys. Chem.* **1986,** 90, 4604-4607.

18) Smotkin, E.S.; Cerveramarch, S.; Bard, A. J.; Campion, A.; Fox, M. A.; Mallouk, T.; Webber, S. E. *J. Phys. Chem.* **1987,** 91, 6-8.

19) Cerveramarch, S.; Smotkin, E.; Bard, A. J.; Campion, A.; Fox, M. A.; Mallouk, T.; Webber, S. E.; White, J. M. *J. Electrochem. Soc.* **1988,** 135, 567-573

20) Karami, H.; Mousavi, M.; Samsipur, M. *J. Power Sources* **2003,** 124, 303-308.

21) Weisener, K.; Ohms, D.; Benezur-Urmossy, G.; Berthold, M.; Haschka, F. *J. Power Sources* **1999,** 84, 248-258.

22) Mehta, V.; Cooper, J. *J. Power Sources* **2003,** 114, 32-53.

23) Bradley, J-C.; Chen, H. M.; Crawford, J.; Eckert, J.; Ernazarova, K.; Kurzeja, T.; Lin, M.; Mcgee, M.; Nadler, W.; Stephens, S. G. *Nature* **1997,** 389, 268-271

24) Bradley, J-C.; Crawford, J.; Ernazarova, K.; Mcgee, M.; Stephens, S. G. *Adv. Mater.* **1997,** 9, 1168-1171.

25) Bradley, J-C.; Ma, Z.; Clark, E.; Crawford, J.; Stephens, S. G. *J. Electrochem. Soc.* **1995,** 146, 194-198.

26) Bradley, J-C.; Crawford, J.; Mcgee, M.; Stephens, S. G. *J. Electrochem. Soc.* **1998,** 145, L45-L47.

27) Bradley, J-C.; *U. S. Patent 6,* **1998,** 120, 669

28) Bradley, J-C.; Ma, Z.; Stephens, S. G. *Adv. Mater.* **1999,** 11, 374-378.

29) Bradley, J-C.; Ma, Z. *Angew. Chem. Int. Ed.* **1999,** 38, 1663-1666.

30) Bradley, J-C.; Babu, S.; Mittal, A.; Ndangu, P.; Carroll, B.; Samuel, B. *J. Electrochem. Soc.* **2001,** 148, C647-C651.

31) Bradley, J-C.; Babu, S.; Ndangu, P. *Fullerenes, Nanotubes, Carbon Nanoconstruct,* **2005,** 227-237.

32) Babu, S.; Ndangu, P.; Bradley, J-C.; Rossi, M. P.; Gogotsi Y *Microfuid Nanofluid* **2005,** 1, 284-288.

33) Warakulwit, C.; Nguyen, T.; Majimel J.; Delville, M. H. Lapeyre V.; Garrigue, P.; Ravaine, V.; Limtrakul, J.; Kuhn, A. *Nano Lett.* **2008,** 8, 500-504.

34) Loget, G.; Larcade, G, Lapeyre, V.; Garrigue, P.; Warakulwit, C.; Delville, M. H.; Ravaine, V.; Kuhn, A. *Electrochim. Acta* **2010,** 55, 8166-8120.

35) Loget, G.; Lapeyre, V.; Garrigue, P.; Warakulwit, C.; Limtrakul, J.; Delville, M. H.; Kuhn, A. *Chem. Mater.* **2011,** 23, 2595-2599.

36) Loget, G.; Fattah, Z.; Bouffier, A.; Khun, A. *J. Am. Chem. Soc.* **2012,** 134, 20033-20036.

37) Fattah, Z.; Garrigue, P.; Lapeyre, V.; Kuhn, A.; Bouffier, L. *J. Phys. Chem. C* **2012,** 116, 22021-22027

38) Loget, G.; Roche, J.; Bouffier, A.; Khun, A. *Adv. Mater.* **2012,** 24, 5111-5116.

39) Bradley, J-C.; Babu, S.; Carroll, B.; Mittal, A. *J. Electroanal.* Chem. **2002,** 522, 75-85.

40) Wang, Y.; Hernandez, R. M.; Berrtlett, D. J.; Bingham, J.M.; Kline, T. R.; Sen, A.; Mallouk, T. E. *Langmuir* **2006,** 22, 10451-10456.

41) Loget, G.; Kuhn, A. *J. Am. Chem. Soc.* **2010,** 132-15918-15919.

42) Loget, G.; Kuhn, A. *Nat. Commun.* **2011,** 2, 535.

43) Loget, G.; Kuhn, A. *Anal. Bioanal. Chem.* **2011,** 400, 1691-1704.

44) Loget, G.; Kuhn, A. *Lab Chip* **2012,** 12, 1967-1971.

45) Loget, G.; Kuhn, A. *J. Am. Chem. Soc.* **2012,** 82, 15918-15919.

46) Sentic, M.; Loget, G.; Manojlovic, D.; Kuhn, A.; Sojic, N. *Angew. Chem. Int. Ed.* **2012,** 11284-11288

47) Arora, A.; Eijkel, J. C. T.; Morf, W.; Manz, A. *Anal. Chem.* **2001,** 73, 3282-3288.

48) Zhan, W.; Alvarez, J.; Crooks, R. M. *J. Am. Chem. Soc.* **2002,** 124, 13265-13270.

49) Zhan, W.; Alvarez, J.; Crooks, R. M. *Anal. Chem.* **2003,** 75, 313-318

50) Zhan, W.; Alvarez, J.; Sun, L.; Crooks, R. M. *Anal. Chem.* **2003,** 75, 1233-1238.

51) Chow, K-F.; Mavre, F.; Crooks, R. M. *J. Am. Chem. Soc.* **2008,** 130, 7544-7545.

52) Chow, K-F.; Mavre, F.; Crooks, J.; Chang, B-Y.; Crooks, R. M. *J. Am. Chem. Soc.* **2009,** 131, 8364-8365.

53) Wu, M-S.; Qian, G-S.; J-J.; Chen, H-Y. *Anal. Chem.* **2012,** 84, 5407-5414.

54) Wu, M-S.; Xu, B-Y.; Shi, H-W.; Xu, J-J.; Chen, H-Y. *Lab. Chip.* **2011,** 11, 2720-2724.

55) Lin, X.; Zheng L.; Gao, G.; Chi, Y.; Chen, G. Anal. Chem. 2012, 84, 7700-7707.

56) Wu, M-S.; Yuan, D-J.; Xu, J-J.; Chen, H-Y. *Chem. Sci.* **2013,** Advance Article.

57) Chang, B-Y.; Chow, K-F.; Crooks, J. A.; Mavre, F.; Crooks, R. M. *Analyst* 2012**,** 137, 2827-2833.

58) Mavre, F.; Chow, K-F.; Sheridan, E. Chang, B-Y.; Crooks, J.A.; Crooks, R. M. *Anal. Chem.* **2009,** 81, 6218-6225.

59) Nyholm, L. *Analyst*, **2005,** 130, 599-605.

60) Klett, O.; Nyholm, L. *Anal. Chem.* **2003,** 75, 1245-1250.

61) Ordeig, O.; Godino, N.; del Campo, J.; Munoz. X.; Nikolajeff, F.; Nyholm, L. *Anal. Chem.* **2008,** 80, 3622-3632.

62) Chow, K-F.; Chang, B-Y.; Zaccheo, B. A.; Mavre, F.; Crooks, R. M. *J. Am. Chem. Soc.***2010,** 132, 9228-9229.

63) Fosdick, S. E.; Crooks, R. M. *J. Am. Chem. Soc.* **2011,** 134, 863-866.

64) Zhang, C. X.; Thormann, W. *Anal. Chem.* **1998,** 70, 540-548.

65) Wei, W.; Xue, G.; Yeung, E. S. *Anal. Chem.* **2002,** 74, 934-940.

66) Dhopeshwarkaer, R.; Hlushkou, D.; Nguen, M.; Tallarek, U.; Crooks, R. M. *J. Am. Chem. Soc.* **2008,** 130, 10480-10481.

67) Hlushkou, D.; Perdue, R. K.; Dhopeshwarkaer, R.; Crooks, R. M.; Tallarek, U. *Lab Chip* **2009,** 9, 1903-1913.

68) Perdue, R. K.; Laws, D. R.; Hlushkou, D.; Tallarek, U.; Crooks, R. M. *Anal. Chem.***2009,** 81, 10149-10155.

69) Sheridan, E.; Hlushkou, D.; Anand, R. K.; Laws, D. R.; Tallarek, U.; Crooks, R. M. *Anal. Chem.* **2011,** 83, 6746-6753.

70) Anand, R. K.; Sheridan, E.; Sheridan, E.; Hlushkou, D.; Crooks, R. M. *Anal. Chem.* **2011,** 83, 2351-2358.

71) Sheridan, E.; Hlushkou, D.; Sheridan, E.; Hlushkou, D.; Tallarek, U.; Crooks, R. M. . *Anal. Chem.* **2012,** 84, 7393-7399.

72) Laws, D. R.; Hlushkou, D.; Perdue, R. K.; Tallarek, U.; Crooks, R. M. *Anal. Chem.***2009,** 81, 8923-8929.

73) Ulrich, C.; Anderson, O.; Nyholm, L.; Bjorefors, F. *Angew. Chem. Int. Ed.* **2008,** 47, 3034-3036.

74) Ulrich, C.; Anderson, O.; Nyholm, L.; Bjorefors, F. *Anal. Chem.* **2009,** 81, 453-459.

75) Inagi, S.; Ishiguro, Y.; Atobe, M.; Fuchigami. *Angew. Chem. Int. Ed.* **2010,** 49, 10136-10139

76) Ishiguro, Y.; Inagi, S.; Fuchigami, T. *J. Am. Chem. Soc.* **2012,** 134, 4034-4036.

77) Ishiguro, Y.; Inagi, S.; Fuchigami, T. *Langmuir* **2011,** 27, 7158-7162.

78) Shida, N.; Ishiguro, Y.; Fuchigami, T,; Inagi, S. *ACS Macro Lett.* **2012,** 1, 656-659.

79) Ramakrishnan, S.; Shannon, C. *Langmuir* **2010,** 26, 4602-4606.

80) Jeanmaire, D. L.; Suchanski, M. R.; Van Dyne, R. P. *J. Am. Chem. Soc.* **1975,** 97, 1699.

81) Crowly, K.; Cassidy, J. *J. Electroanal. Chem.* **2003,** 547, 75-82

82) Kreibig, U.; Vollmer, M. *Optical Properties of Metal Clusters*, vol. 25. Springer-Verlag:Heidelberg, **1995,** Pg. 532.

83) Schatz, G. C.; van Dyne, R. P. Electromagnetic Mechanism of Surface Enhanced spectroscopy, vol. 1. John Wiley: New York, 2002, Pg.759

84) Dick, L. A.; Haes, A. J.; Van Duyne, R. P. *J. Phys. Chem. B* **2000,** 104, 11752–11762

85) Oklejas, V.; Uibel, R. H.;Horton, R.; J. M. *Anal. Chem.* **2008**, 80, 1891–1901

86) Régis, A.; Hapiot, P.; Servagent-Noinville, S. *Anal. Chem.* **2000,** 72, 2216-2221.

87) Edward , M.; Wachs, I. E. *J. Phys. Chem. C* **2007,** 111, 14410-14425.

88) Yeo, B. S.; Bell, A. T. *J. Am. Chem. Soc.* **2011,** 133, 5587-5593

89) Yeo, B. S.; Bell, A. T. *J. Phys. Chem. C* **2012,** 116, 8394-8400.

90) Markevich, G.; Salitra, G.; Aurbach, D. *Electrochem. Commun.* **2005,** 7, 1298-1304.

91) Park, Y.; Kim, N. H.; Kim, J. Y.; Eom, I-Y.; Jeong, Y. U.; Kim, M. S.; Lee, M. L.; Choi, H. C.; Jung, Y. M. *Vibrational Spectroscopy* **2010,** 53, 60-63.

Chapter 2

Spectroelectrochemical Characterization of Bipolar Electrodes

2.1 Introduction

Over the past few decades, there has been an increased interest in patterning surfaces with chemical or physical properties mainly due to the development of sophisticated patterning techniques such as lithography[1, 2]. Although these techniques are robust and can produce well–defined patterns, they often lead to patterns with very sharp boundaries between the distinct chemical or physical regions on the substrate. However, depending on the application, a pattern with gradual changes in its property over a certain length in space may be desired instead. This can be achieved using a material gradient, characterized by gradual variations in a physicochemical property. Such gradients can be used in numerous applications. For example, they can be used to drive a phenomenon such as moving liquids across a given surface. These gradients can also be used in combinatorial science for property screening with lower research and production cost[3, 4]. The later application can be used in the design and discovery of new catalysts and drugs[5] or to monitor protein adsorption[6, 7]. Several techniques for creating material gradients have been reported, most of which rely on processes such as deposition[8], diffusion[9, 10] and immersion[11, 12] and microfluidics[13, 14]. Larsen and coworkers recently reported a concentration gradient of alkyne-terminated molecules on an azide-funtionalized polymer substrate using “electro click chemistry”[15].

Bipolar electrochemistry has emerged recently as a powerful technique to generate patterns with gradual variations in physicochemical properties on electrode surfaces. The operating principles of bipolar electrochemistry have been described in section 1.6. Typically, when a potential difference is applied across a solution containing an electronically conducting substrate that is not physically connected to the external power supply, a potential gradient or electric field develops across the solution due to its resistance. When this electric field exceeds a certain threshold value, the substrate will behave as a bipolar electrode-one that simultaneously acts as a cathode and as an anode. The substrate can act as a bipolar electrode because there will exist regions in the solution where its potential is greater than that of the substrate (cathodic pole) and regions where its potential is lower that than that of the substrate (anodic pole). The anodic and cathodic poles are separated by a single position where the solution potential equals the substrate potential. As illustrated in figure 1.2.1, the potential difference between a point on the bipolar electrode and the solution varies laterally along the surface. Because an interfacial potential difference is the driving force for electrochemical reactions, the rates of redox reactions are highest at the edges of the bipolar electrode and decrease towards the center. This variation in interfacial potential difference can be used to generate surface gradients of various chemical and physical properties. The major advantage of this technique is that it is fast and the experimental setup is very simple comprising of only a pair of driving electrodes and a simple power supply. Moreover reactions on the surface of the bipolar electrode can be easily controlled by simply adjusting the electric field in solution. This enables the control of the position and length of gradients on bipolar electrodes as will be demonstrated in this work.

Bjorefors and coworkers (section 1.6, ref 73) first reported the use of bipolar electrochemistry to create a surface gradient of molecular functionality by selective desorption of a self assembled monolayer (SAM) of an alkanethiol on the surface of a gold electrode. Imaging surface plasmon resonance (iSPR) and imaging-null-ellipsometry were employed in order to visualize the gradient.

The self assembly of alkanethiols on metal substrates constitutes a fundamental component in numerous applications including molecular electronics[17, 18] and surface modification due to their ability to pack densely and their resistance to mechanical and chemical stress. They provide anchor sites for redox active molecules, thereby enabling electrochemical patterning of electrode surfaces[19] for electroanalysis. Unlike the work of Bjorefors and coworkers we report a non-destructive patterning of a SAM of a thiol-funtionalized moiety, 2-Anthraquinonyl sulfide (2-AQS) which can be transformed electrochemically to 2-Hydroanthraquinonyl sulfide (2-H_2AQS). The conversion of 2-AQS to 2-H_2AQS occurs at the cathodic pole of the bipolar electrode. Because there exists a potential gradient on the surface of the bipolar electrode the relative population of 2-AQS to 2-H2AQS will vary accordingly resulting in a gradient in both species. Surface enhanced Raman spectroscopy (SERS) was used to monitor the extent of the redox reactions as a function of axial position along gold and silver bipolar electrodes. This allowed the gradients formed to be visualized and evaluated. Moreover, by using the traditional three-electrode setup in conjunction with SERS, the dependence of SERS response on the applied potential was found to follow the Nernst equation. This finding provided a correlation between the SERS response and the potential difference that exists at the interface between the solution and the bipolar electrode. Finally, it

was demonstrated that by changing the applied voltage between the driving electrodes so as to alter the electric field in solution, the position and length of the gradient can be varied.

2.2 Materials and Methods

2.2.1 Chemicals and Materials. 2-chloroanthraquinone (Aldrich), N,N-dimethylacetamide (Aldrich) and butanethiol (Aldrich) were of analytical grade and were used as received. Bipolar electrodes were made from silver foil (99.9% purity, Aldrich). The driver electrodes for the bipolar electrochemical cell were made from stainless steel foil (Alfa Aesar). Alumina slurry and microfiber polishing cloth were purchased from Buehler. Millipore-Q purified deionized waterwater (18.2MΩ·cm) was used to prepare all solutions and rinse electrodes. A 0.1M Britton – Robinson buffer was used at the electrolyte for all electrochemical measurements.

2.2.2 Synthesis of 2-anthraquinonylbutylsulfide (2-AQS) 2-AQS was synthesized according to a procedure described by Nishiyama et al[1]. 2.4g of 2-chloroanthraquinone, 1.0g of butanethiol and 0.4g of KOH were refluxed in 150mL of N, N-dimethylacetamide in a round-bottom flask for 4hrs. After cooling, concentrated HCl was added to precipitate the product. The precipitate was collected in a fine frit filter and then recrystallized in ethanol to yield pure yellow crystals of 2-AQS. The 2-AQS product was characterized by ^{1}H and ^{13}C nuclear magnetic resonance (NMR) spectroscopy (400MHz, $CDCl_3$) and gas chromatography-mass spectroscopy (GC-MS). ^{1}H NMR: δ 0.97 (3H, t), δ 1.52 (2H, sex), δ 1.72 (2H, quin), δ 3.06 (2H, t), δ 7.51-8.20 (7H, multi). ^{13}C NMR: δ 13.80 (1C, s), δ 22.21 (1C, s), δ 30.64 (1C, s), δ

31.55 (1C, s), δ 77.23 (1C, t), δ 123.30-145.00 (11C, multi), δ 182.00 (1C, t). GC-MS: m/z 240.01, 296.06 (M+, base peak).

2.2.3 Substrate preparation. Electrodes were mechanically polished using 0.05μm-size Alumina paste and then sonicated in distilled water for 5 min. They were then rinsed sequentially with distilled water, absolute ethanol and distilled water. In order to enhance the Raman signal, the surface of the Ag electrode was electrochemically roughened by performing three oxidation reduction cycles (ORC), scanning the potential between -300mV and 300mV at scan rate of 5mV/sec in a solution containing 0.1M KCl and 0.1M $LiClO_4$. Unlike the Ag electrode, up to50 ORC between -200 and 1200mV were needed to make the Au electrode SERS active. The roughened electrode was then incubated in an ethanolic solution of 1mM 2-AQS overnight.

2.2.3 Electrochemical measurement Before all electrochemical measurements, the electrolytic solution was degassed with Argon for about 20min and a blanket of argon was maintained above the solution during the measurements. All bipolar electrochemical measurements were performed in a home-built single compartment cell (ca. 20mL total volume) using a Hewlett-Packard model 6010 regulated DC power supply to control the potential applied between the two stainless steel driver electrodes separated by 4.5cm. The electrically floating 2-AQS-modified Ag or Au electrode was placed symmetrically between the two driver electrodes. After immersing all three electrodes in the 0.1M B&R (pH 7.00) buffer electrolyte, a potential was applied across the driver electrodes. The entire cell was mounted on the Raman microscope stage and this potential was maintained while the Rama spectra were recorded. The microscope objective was moved to different positions on the

surface of the bipolar electrode to probe the distribution of the interfacial potential and therefore the extent of reactions on the surface of the electrode.

All unipolar electrochemical measurements were performed using a standard three-electrode configuration in a home-built glass cell. In all cases the 2-AQS-modified Ag or Au electrodes was used as working electrodes while Pt gauze was used as the counter electrode. All measurements were made against a Ag/AgCl(sat) (Bioanalytical Systems, Inc.) reference electrode. The electrochemical cell was controlled using an Epsilon electrochemical work station (Bioanalytical Systems, Inc.).

2.2.5 Raman spectroscopy Raman scattering was excited using the 514nm output (ca. 34mW) from an air cooled argon ion laser (model 163-C42, Spectra-Physics lasers, Inc.). The spectra were collected and analyzed using a Renishaw InVia Raman microscope and associated software. A leica 50x (0.75NA) objective was used to focus the excitation light onto the sample. The scattered radiation was collected by the same objective through a spectrometer with entrance slits of about 12-15μm. The exposure time for each spectrum was 30 seconds and only a single scan was made. A 1200 lines mm^{-1} grating was used for all measurements providing a resolution of $\pm 1 cm^{-1}$. The instrument was calibrated for the Raman shift by referencing to that of Si.

2.3 Result and discussion

2.3.1 Demonstration of Principle Figure 2.3.1 a shows a typical setup for conducting a bipolar electrochemical experiment. In this simple demonstration two driving electrodes (made of stainless steel) dipped into an aqueous $CuSO_4$ solution are connected to the terminals of a power supply. The bipolar electrode, also made of stainless steel, is placed

between the driving electrodes. Upon application of a voltage of 8V (figure 2.3.1b), faradaic reactions are initiated on the driving electrodes with Cu deposition on the cathode and water oxidation at the anode. However, of special interest are the reactions that occur on the bipolar electrode that lies between the driving electrodes. The side of the bipolar electrode facing the driving cathode acts as the anode and water oxidation occurs on this side. On the other hand, the side facing the driving anode acts as the cathode and Cu deposition occurs on this side. Figure 2.3.1c shows an enlarged view of the bipolar electrode. It shows that the amount of Cu deposited on the bipolar electrode is higher at the edge and gradually decreases towards the center. That is, a gradient in the amount of Cu is created at the cathodic pole. The formation of this gradient clearly demonstrates the variation in the interfacial potential difference along the bipolar electrode that results in a variation of the driving force for electrochemical reactions along the surface of the electrode.

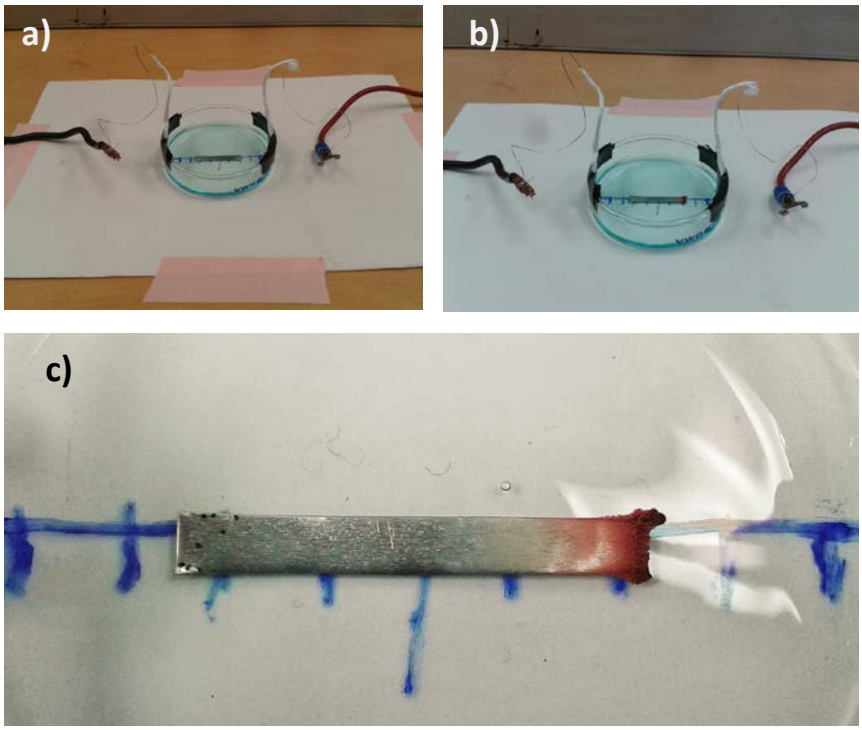

Figure 2.3.1 Demonstration of the effect of bipolar electrochemistry. **(a)** Bipolar electrochemical cell containing an aqueous $CuSO_4$ solution, a stainless steel bipolar electrode and two stainless steel driver electrodes connected to the terminals (black, negative; red, positive) a power supply. **(b)** Faradaic reactions (copper deposition and water oxidation) upon application of a voltage of 8V across the driver electrodes. **(c)** Magnified image of **(b)** showing a gradient in the amount of copper deposited on the anodic pole of the bipolar electrode.

In order to maintain electroneutrality on the surface of bipolar electrode, the anodic and cathodic reactions must occur simultaneously. The driving force needed for two faradaic reactions to occur simultaneously at the extremities of the bipolar electrode is the potential difference, ΔE_e, defined as the fraction of the applied voltage E_{appl}, dropped across the length

of the BPE according to equation 1.5.1. In a first-order approximation, the minimum value of ΔE_e is given by the difference of the formal potentials of the two redox couples involved in the faradaic reactions. For example, consider the demonstration

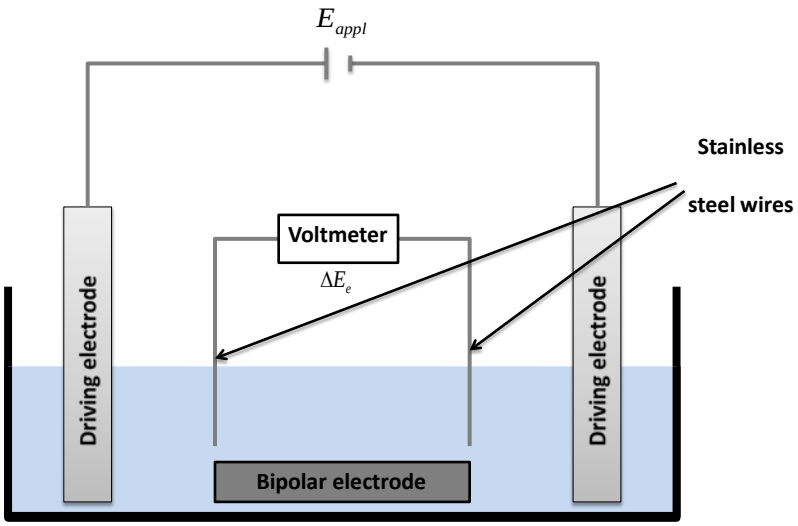

Figure 2.3.2 Illustration of the experimental setup used to measure the potential difference, ΔE_e, between the edges of the bipolar electrode for a given applied driving voltage, ΔE_{appl}.

in figure 2.3.1 involving the reduction of Cu^{2+} at the cathodic pole and the oxidation of water at the anodic pole:

Cathode:

$$Cu^{2+}{}_{(aq)} + 2e^- \rightarrow Cu_{(S)} \qquad E^0_{Cu^{2+}/Cu} = 0.34V \; vs \; NHE \qquad 2.3.1$$

Anode:

$$2H_2O_{(l)} \rightarrow 4H^+_{(aq)} + O_{2\,(g)} + 4e^- \qquad E^0_{O_{2/H_2O}} = 1.23V\ vs\ NHE \tag{2.3.2}$$

It follows that

$$\Delta E_{e,min} = \left| E^0_{Cu^{2+}/Cu} - E^0_{O_{2/H_2O}} \right| = 0.89V \tag{2.3.3}$$

Therefore, for these two reactions to occur to an appreciable extent ΔE_e must be greater than $0.89V$. Unfortunately, there is no direct method for measuring ΔE_e. However, it can be determined indirectly using a method illustrated in figure 2.3.2. In essence, two stainless steel wires connected to the terminals of a Voltmeter were dipped into the bipolar electrochemical cell containing the electrolytic. The separation between the wires corresponds to the length of the bipolar electrode. Because the voltmeter has a very high internal resistance, little current can flow through it. This means no faradaic reactions occur at the stainless steel wires, which will otherwise decrease the electric field or potential drop, ΔE_e, in the solution over the bipolar electrode. Equation 1.5.1 indicates that ΔE_e and therefore the extent of faradaic reactions is directly proportion to the applied voltage, E_{appl}. In order to demonstrate this point, ΔE_e was measured as a function of E_{appl} and the results are provided in figure 2.3.3 (black square). These results were compared to the calculated (red circles in figure 2.3.3) values that are based solely on geometrical arguments according to equation 1.5.1. The results indicate that the measured value of ΔE_e is less than the calculated value. This can be explained by the fact that a fraction of the applied voltage, E_{appl}, is lost at the interface between the driving electrodes and the solution.

Important information that can be obtained from equation 1.5.1, which can be very useful when designing experiments based on bipolar electrochemistry, is that for given electric field

(E_{appl}/l) higher values of ΔE_e and therefore greater extent of faradaic reactions can be obtained by using longer electrodes. This hypothesis was tested experimentally for three different electrolyte concentration and the results are provided in figure 2.3.4. The values of ΔE_e were measured using the set up in figure 2.3.2. The results clearly demonstrate that for a voltage of 8V applied between two driving electrodes separated by a length of 5cm, ΔE_e increased linearly as a function of the distance between the stainless steel wires connected to the voltmeter. It should be noted that the distance between the wires corresponds to the length of the bipolar electrode. Figure 2.3.4 also shows that for a bipolar electrode of a given length, a higher value of ΔE_e can be achieved by using a solution with lower concentration.

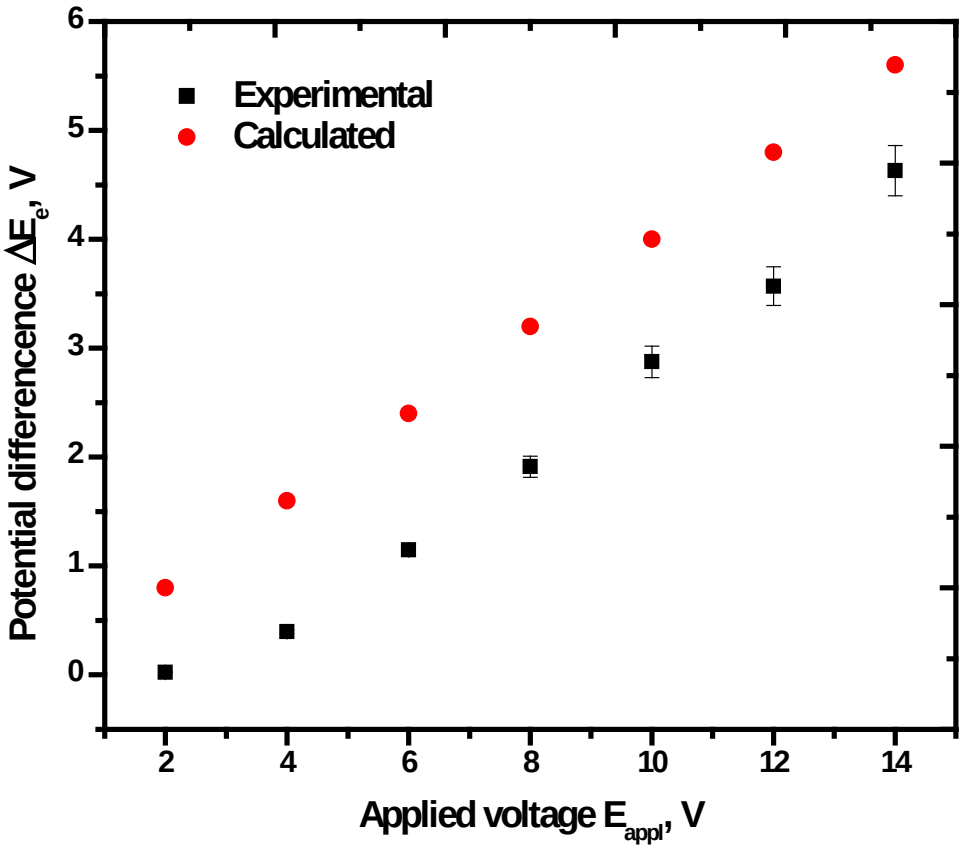

Figure 2.3.3 Plot of potential difference, ΔE_e between the edges of the bipolar electrode using the setup shown in figure 2.3.2. The solution contained 0.1M KNO_3.

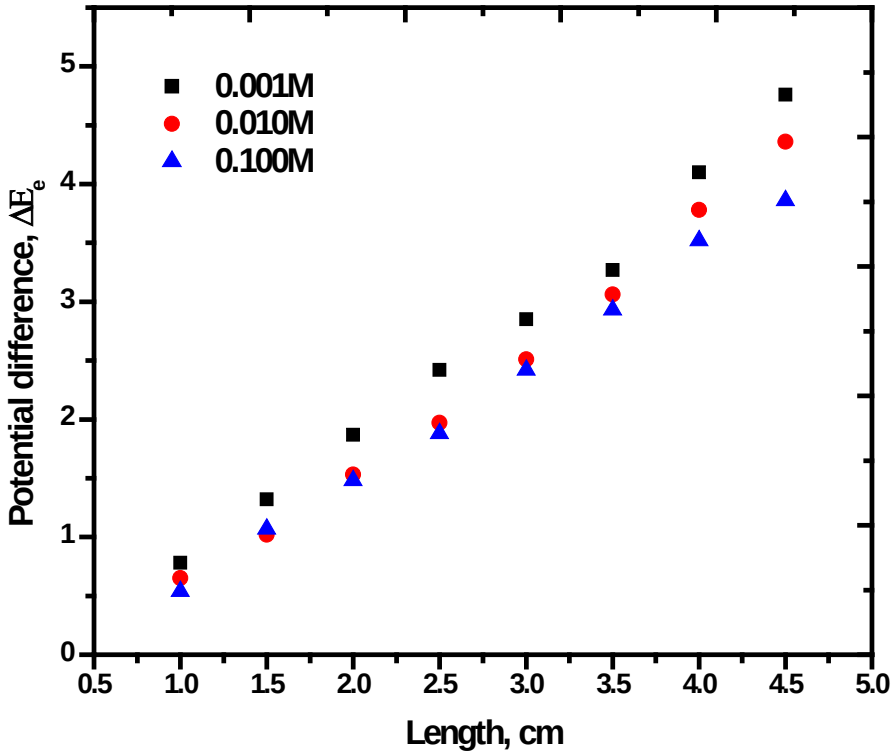

Figure 2.3.4 Plot of potential difference, ΔE_e as a function of length of bipolar electrode measured using the set up in figure 2.3.2. The solution used contained various concentrations of KNO_3.

2.3.2 Electrochemical Characterization of 2-AQS SAM on Gold and Silver Electrodes

Prior to using 2-AQS as a model compound to illustrate the surface-patterning capability of bipolar electrochemistry, its redox activity was investigated on Au and Ag electrodes. Figure 2.3.5 shows the cyclic voltammogram (CV) recorded in 0.1M B&R buffer (pH 7.00) with an Au electrode modified by a 2-AQS SAM from 1mM ethanolic solution. The reduction and oxidation waves at -0.5V and -0.48V respectively, present in the CV indicate that the 2-AQS immobilized on the Au surface is redox active. These potentials are independent of the scan

rate up to 100mV/s. Moreover, as shown in the inset, the peak currents are linearly dependent on the scan rate, indicating that the redox reaction is due to an adsorbed species.

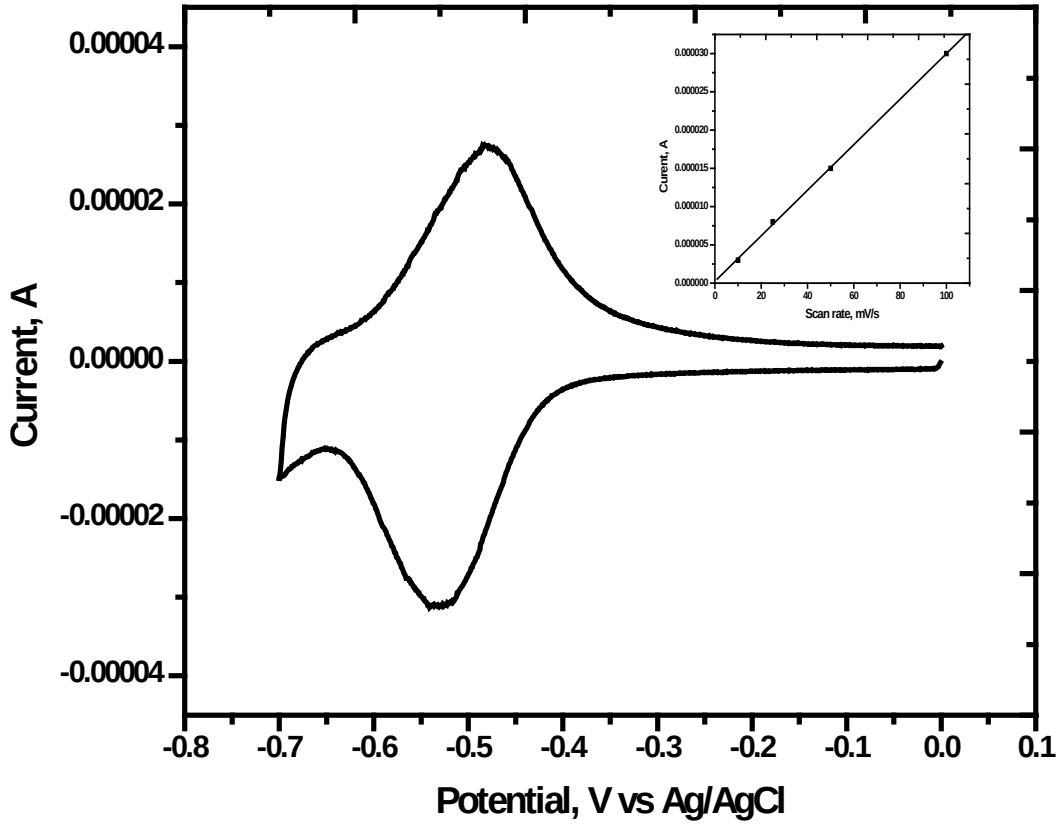

Figure 2.3.5 Cyclic voltammogram of 2-AQS on an Au electrode in B&R buffer (pH 7.00). Inset shows the scan rate of the anodic peak currents.

Figure 2.3.6 shows the CV of 2-AQS SAM on an Ag electrode recorded in 0.1M B&R buffer (pH 7.00). Clearly, the shape of the CV reveals an apparently irreversible behavior that is characterized by the absence of significant current on the reversal scan. This behavior persists for scan rate up to 200mV/sec. At higher scan rates, however, a reversible behavior is

observed. In all cases the peak potential shifted to more negative values with increasing scan rate indicating slow electron-transfer kinetics [20]. The electrochemical trend seen in this case is characteristic of an EC mechanism whereby an electron transfer is followed by a chemical reaction[21]. This behavior is frequently observed in the electrochemistry of derivatized quinone compounds. It is thought that a very fast protonation step, relative to electron transfer, follows the electrochemical reduction of the quinone molecule in buffered electrolytes at neutral pH resulting in an apparent irreversible voltammetric behavior.

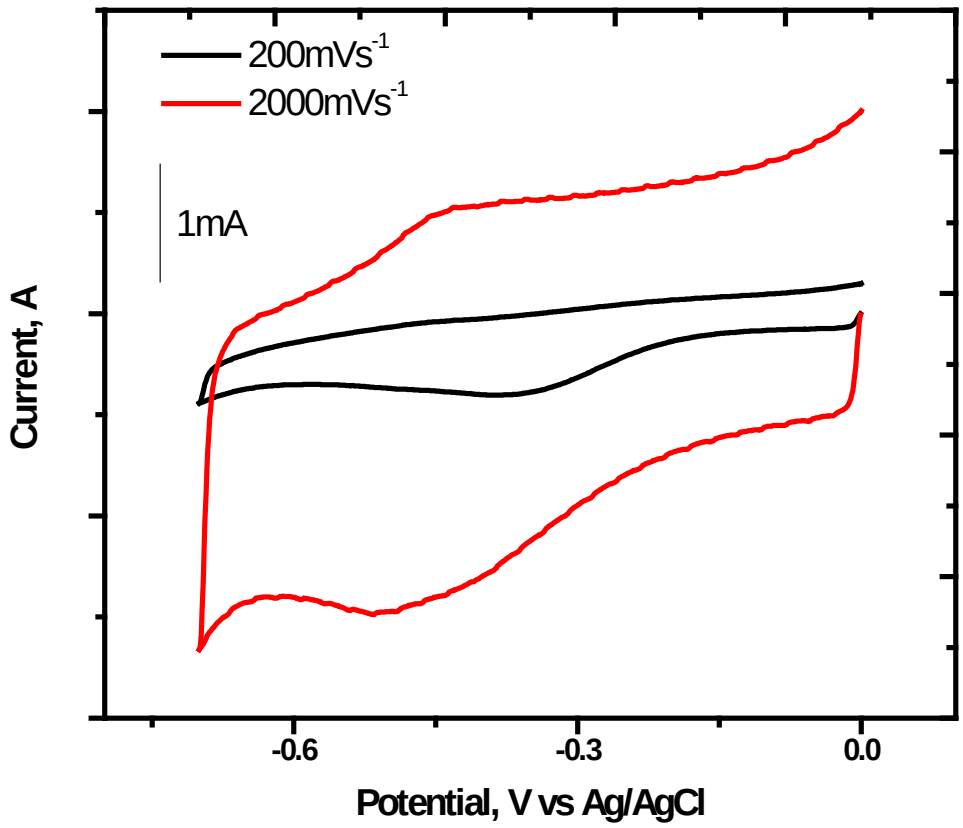

Figure 2.3.6 Cyclic voltammogram of 2-AQS on an Ag electrode in B&R buffer (pH 7.00).

2.3.3 Evaluation of Reaction Gradients on Bipolar Electrodes Using SERS

The use of SERS to visualize reaction gradients on bipolar electrodes was demonstrated for Au and Ag substrates. Figure 2.3.7 shows *in situ* SERS spectra collected at the cathodic edge of an Au bipolar electrode, previously modified with a 2-AQS SAM, before and after application of a voltage across a 0.1M B&R buffer (pH 7.00) containing the bipolar electrode.

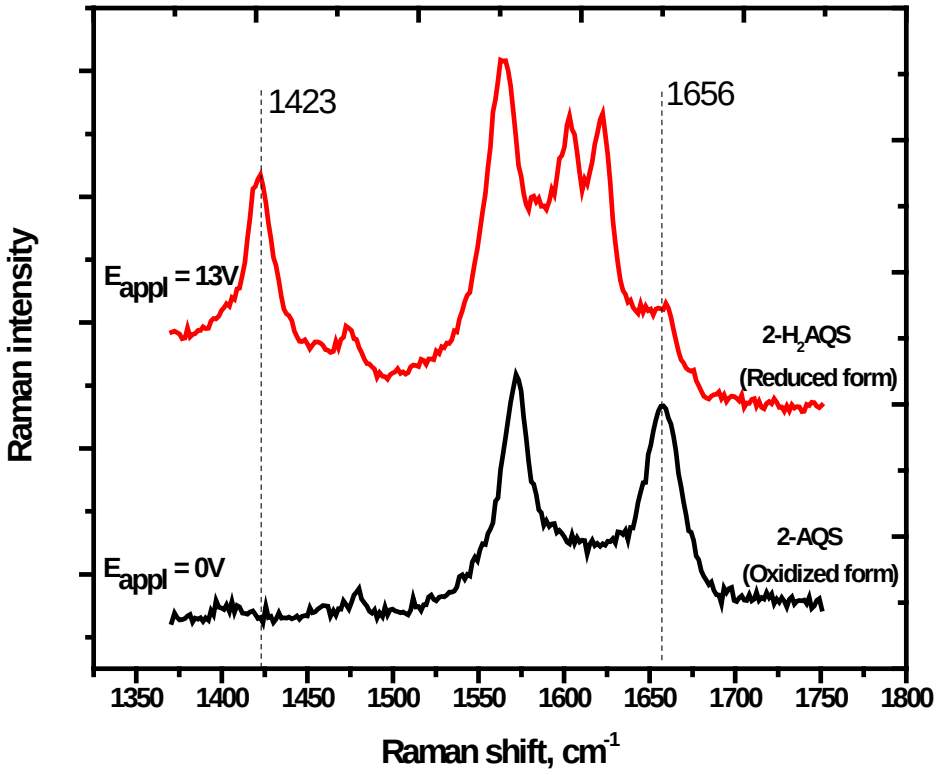

Figure 2.3.7 *In situ* SERS spectra of 2-AQS SAM on an Au bipolar electrode in B&R buffer (pH 7.00). The spectrum were obtained at the edge of the cathodic pole before (black) and after (red) application of a voltage of 13V across the electrolyte.

The spectrum of 2-AQS at open circuit potentials is characterized by a feature at 1656 cm^{-1}, associated with the C=O stretch. When a voltage of 13V is applied across the solution, the C=O band disappears and a new band emerges at about 1423cm^{-1}. This band is assigned to the O-H bend arising from 2-H_2AQS, the reduced form of 2-AQS.The changes in the spectrum after an applied voltage are consistent with data previously reported for 2-AQS SAM on a gold working electrode in the traditional three-electrode setup upon application of a negative potential [19]. More importantly, the changes provide strong evidence that faradaic reactions are initiated on a wireless conducting substrate when a sufficiently high electric field is present in the electrolytic solution. In order to investigate the interfacial potential distribution along the surface of the Au bipolar electrode, Raman spectra were collected at various positions along the electrode, going from the cathodic edge towards the center while maintaining the applied voltage at 13V. The results are shown in figure 2.3.8. Note that the intensity of the O-H bend at 1423cm^{-1} resulting from 2-H_2AQS is strongest at the position $x = 2mm$ and gradually decreases at positions farther away ($x = 10mm$) from the cathodic extremity. On the other hand, the intensity of C=O stretch at 1656cm^{-1} due to 2-AQS is lowest at $x = 2mm$ and increases towards $x = 10mm$, where the interfacial potential difference is not enough to drive faradaic reaction to detectable extents. The variation in the SERS spectra of the immobilized 2-AQS along the Au bipolar electrode is consistent with a potential-dependent change in the relative surface population of 2-AQS and 2-H_2AQS. That is, the interfacial potential difference along the bipolar electrode in not constant but varies with position, going from a higher value at the edge and decreasing to a minimum towards the center. Therefore, the amount of 2-H_2AQS generated due to the reduction of 2-AQS is highest at the edge of the cathodic pole where the potential difference between the bipolar electrode and the solution is

highest and decreases to zero towards the center of the bipolar electrode where the potential difference is at a minimum.

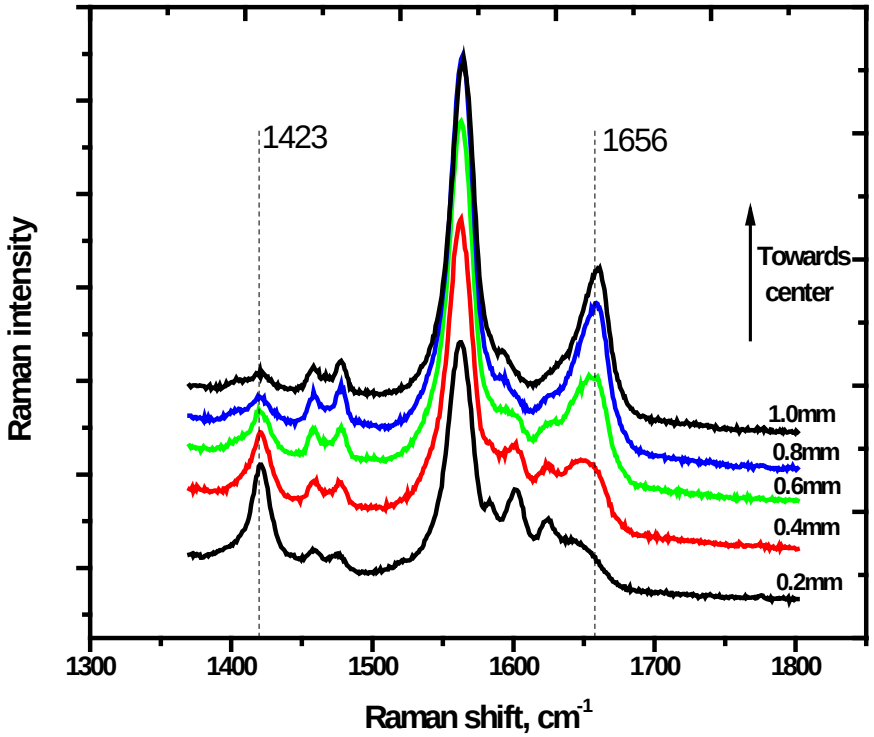

Figure 2.3.8 In situ SERS spectra of 2-AQS SAM on an Au bipolar electrode in B&R buffer (pH 7.00). The spectra were obtained at various positions on the cathodic pole, moving from the edge at $x = 2mm$ towards the center at $x = 10mm$. The applied potential E_{appl} was maintained at 13V.

To estimate the amount of 2-AQS left relative to the amount of 2-H_2AQS formed as a function of position on the Au bipolar electrode, the ratio of the integrated peak intensities from the C=O stretch at 1655cm^{-1} relative to the O-H bend at 1423cm^{-1} was plotted as a function of position as shown in figure 2.3.9. The results displayed in this plot clearly

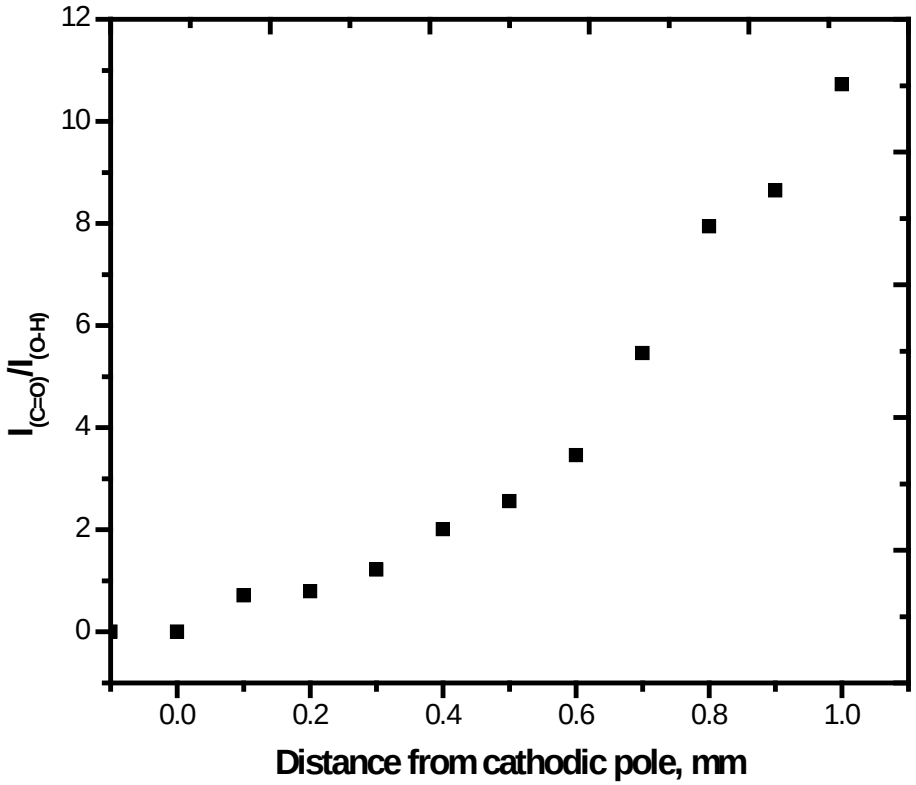

Figure 2.3.9 Relative amount of 2-AQS to 2-H_2AQS ($I_{(C=O)}/I_{(O-H)}$) as a function of position on Au bipolar electrode.

demonstrate that a reaction gradient exists on the surface of the Au electrode which is attributed to the distribution of the potential difference between the electrode and the solution.

To demonstrate the versatility of the bipolar effect, reaction gradients were also evaluated of Ag substrates. Figure 2.3.10 shows *in situ* SERS spectra collected at the edge of the cathodic pole of a 2-AQS modified Ag bipolar electrode before and after application of a

voltage of 8V across the electrolytic solution. Once again, the disappearance of the C=O stretch at 1658cm^{-1} and the appearance of the O-H bend at 1423cm^{-1} provides clear proof that

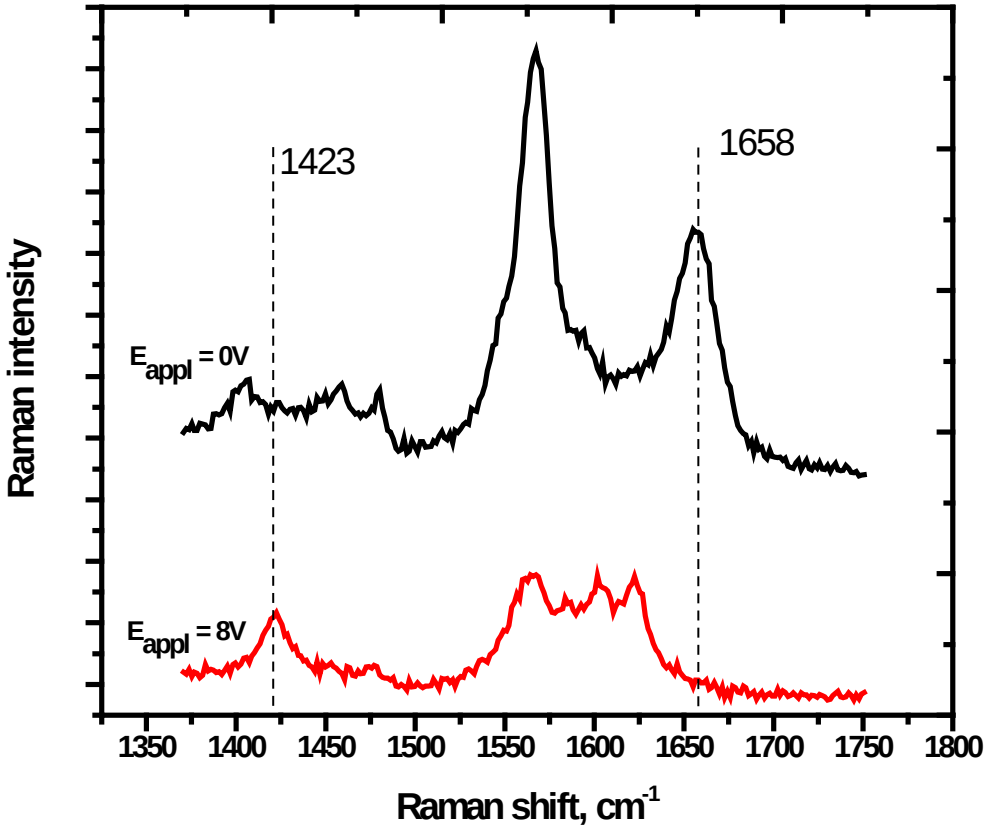

Figure 2.3.10 In situ SERS spectra of 2-AQS SAM on an Ag bipolar electrode in B&R buffer (pH 7.00). The spectrum were obtained at the edge of the cathodic pole before (black) and after (red) application of a voltage of 8V across the electrolyte.

faradaic reactions can be initiated on any conducting substrate in contact with an electrolyte when a electric field is applied to the solution.

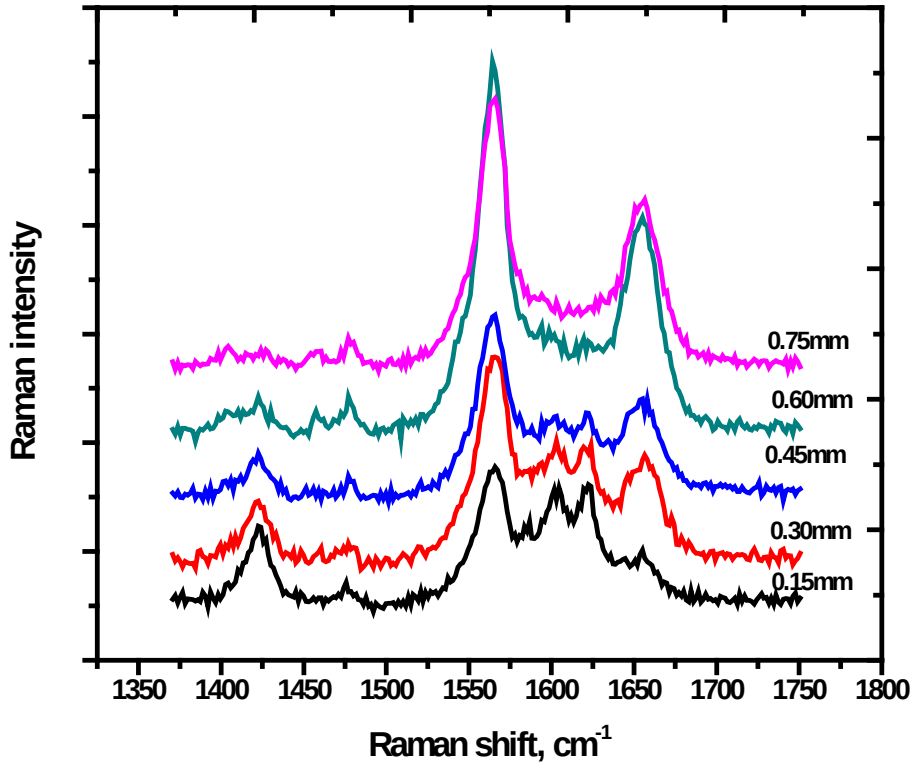

Figure 2.3.11 In situ SERS spectra of 2-AQS SAM on an Ag bipolar electrode in B&R buffer (pH 7.00). The spectra were obtained at various positions on the cathodic pole, moving from the edge at $x = 0.15mm$ towards the center at $x = 0.75mm$. The applied potential E_{appl} was maintained at 8V.

Figure 2.3.11 shows the SERS spectra recorded from various positions on the 2-AQS modified Ag bipolar electrode which reveals the variation of the interfacial potential

difference between the electrode and the solution. The relative population of 2-AQS to 2-H_2AQS on the Ag bipolar electrode following the redox reaction, was obtained by from the ratio of the integrated peak intensities from the C=O stretch at 1656cm^{-1} relative to the O-H bend at 1423cm^{-1} was plotted as a function of position as shown in figure 2.3.12.

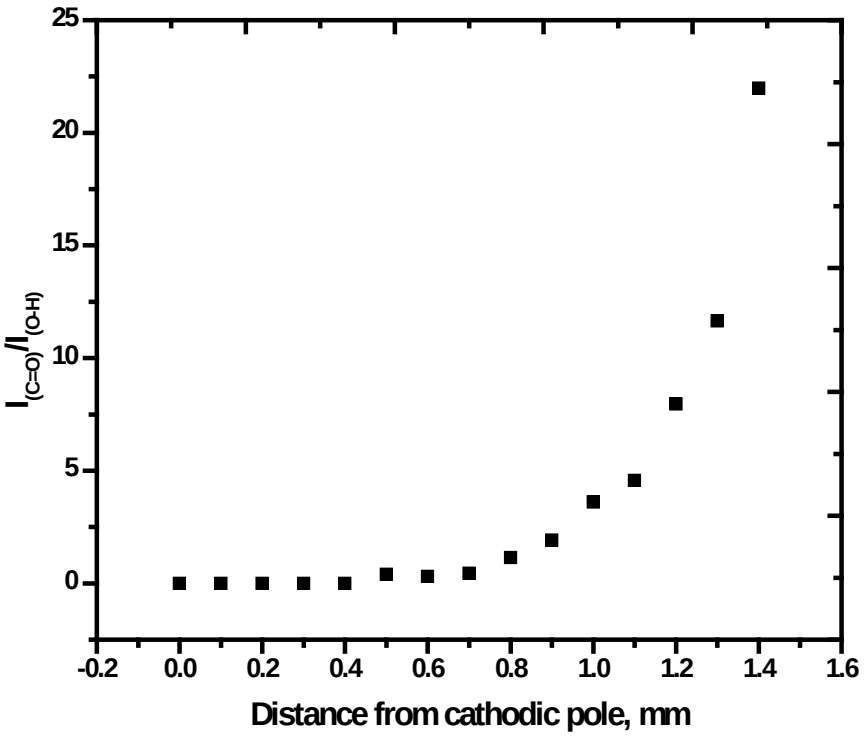

Figure 2.3.12 Relative amount of 2-AQS to 2-H_2AQS ($I_{(C=O)}/I_{(O-H)}$) as a function of position on Ag bipolar electrode.

2.3.4 Relationship between SERS Response and Electrode Potential

To investigate the dependence of the SERS response on the interfacial potential difference,

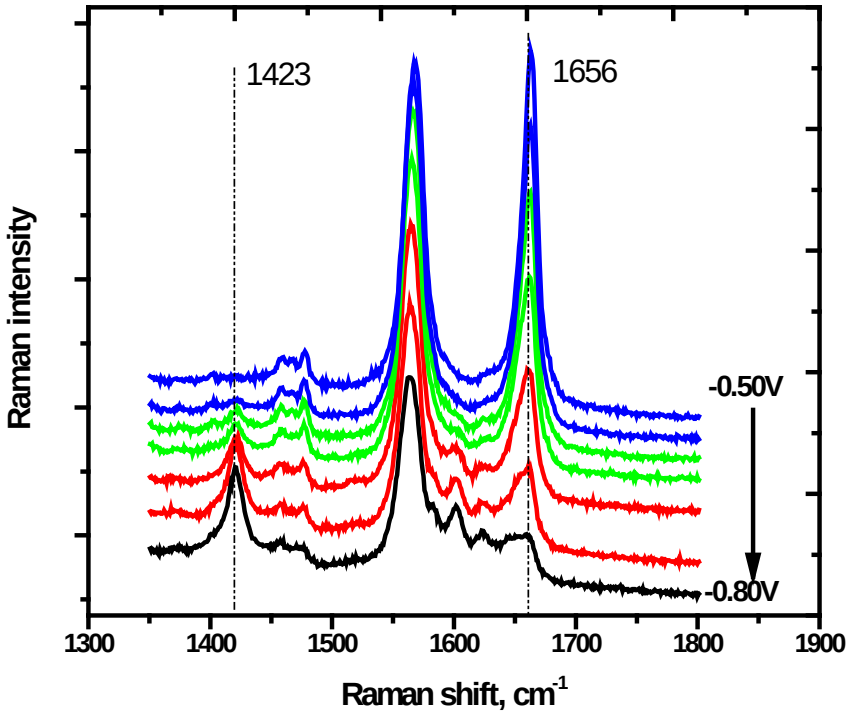

Figure 2.3.13 *In situ* SERS spectra of 2-AQS SAM on an Au working electrode recorded in B&R buffer (pH 7.00) at different potentials in a three-electrode setup.

the 2-AQS SAM-modified Au substrate was used as the working electrode in a three-electrode setup and SERS spectra were recorded as a function of applied potential. The results are shown in figure 2.3.13. It can be noticed that the C=O stretch at 1656cm^{-1} belonging to 2-AQS gradually attenuates while the O-H bend at 1423cm^{-1} belonging to 2-H_2AQS grows stronger with increasing negative applied potentials. Therefore, it can be concluded that the changes observed in the SERS spectra are as a result of the shift in electrode potential from an equilibrium value.

The Raman intensity profile along the bipolar electrode (figure 2.3.9) can be represented in terms of overpotential, η(x) as shown in figure 2.3.14 (top x-axis) according to the following equation equation

$$\eta_{(x)} = E_{(x)} - E_e = V\,(x - x_0) = \frac{\Delta E_e}{l_e}\,(x - x_0) \qquad 1.5.2$$

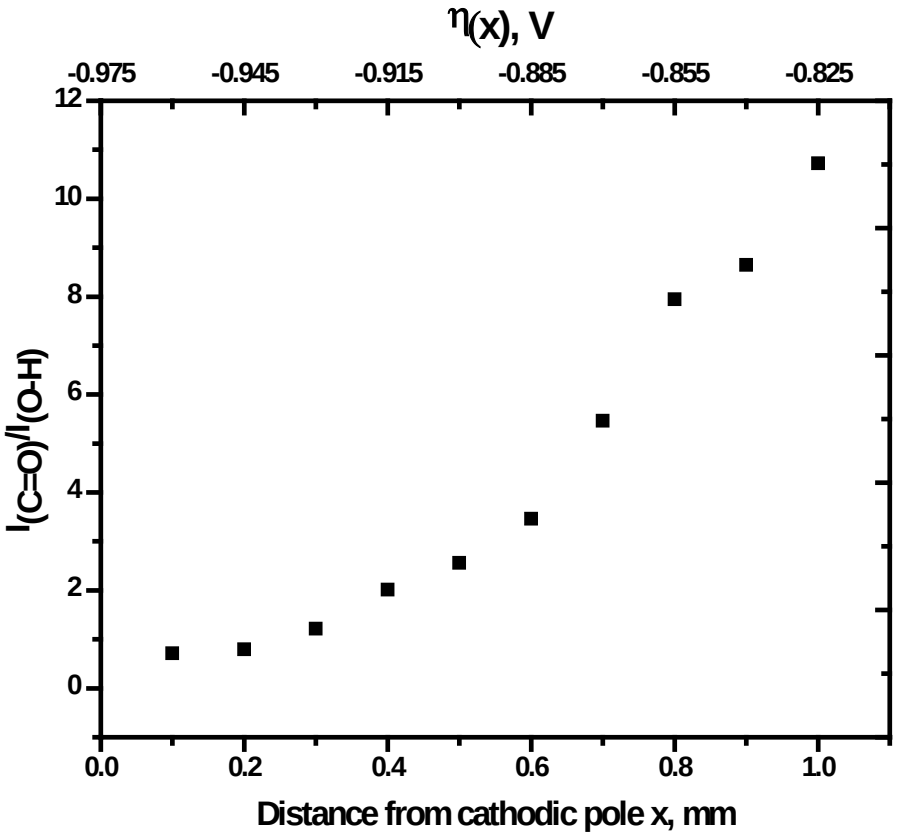

Figure 2.3.14. Relative amount of 2-AQS to 2-H_2AQS ($I_{(C=O)}/I_{(O-H)}$) as a function of position (bottom x-axis) and overpotential, $\eta_{(x)}$ (top x-axis) on Au bipolar electrode.

When the dependence of the Raman response on the overpotential η(x) is looked at, it appears to be to follow a Nernstian behavior. The relative contribution of 2-AQS and 2-H_2AQS to the Raman response is proportional to the relative surface concentration of both species[24, 25] such that the ratio between the surface concentrations of $\Gamma_{2\text{-AQS}}/\Gamma_{2\text{-H2AQS}}$ can be obtained from the ratio of integrated peak intensities of the C=O stretch at 1658cm^{-1} due to 2-AQS, relative to the O-H bend at 1423cm^{-1} due to 2-H_2AQS. The logarithm of this ratio as a function of the overpotential can be expressed according to the Nernst equation as follows

$$\eta(x) = \eta_{1/2} + \frac{0.059}{n} log \frac{\Gamma_{2-AQS}}{\Gamma_{2-H_2AQS}} \qquad 2.3.4$$

$$\eta(x) = \eta_{1/2} + \frac{0.059}{n} log \frac{I_{(C=O)}}{I_{(O-H)}} \qquad 2.3.5$$

Accordingly, figure 2.3.15 was generated using Raman peak intensity ratios obtained from measurements made on the bipolar electrode. The slope obtained from this plot is -0.055V which is about 0.025V higher that the value of 0.030V that is expected for a two-electron transfer process. The intercept of the plot which corresponds to the formal potential $\eta_{1/2}$ is - 0.48V which is in good agreement with the value obtained by cyclic voltammetry. To investigate the disparity between the slope obtained from the this plot and the expected value, cyclic voltammograms were recorded in the pH range 5-9 and the formal potential was plotted as a function of pH as shown in figure 2.3.16. The formal potential $E_{1/2}$ changed by -0.61V pH^{-1}. This result and together with that obtained from the figure 2.3.15 suggest a 1-electron-1-proton reaction of the 2-AQS on the Au electrode.

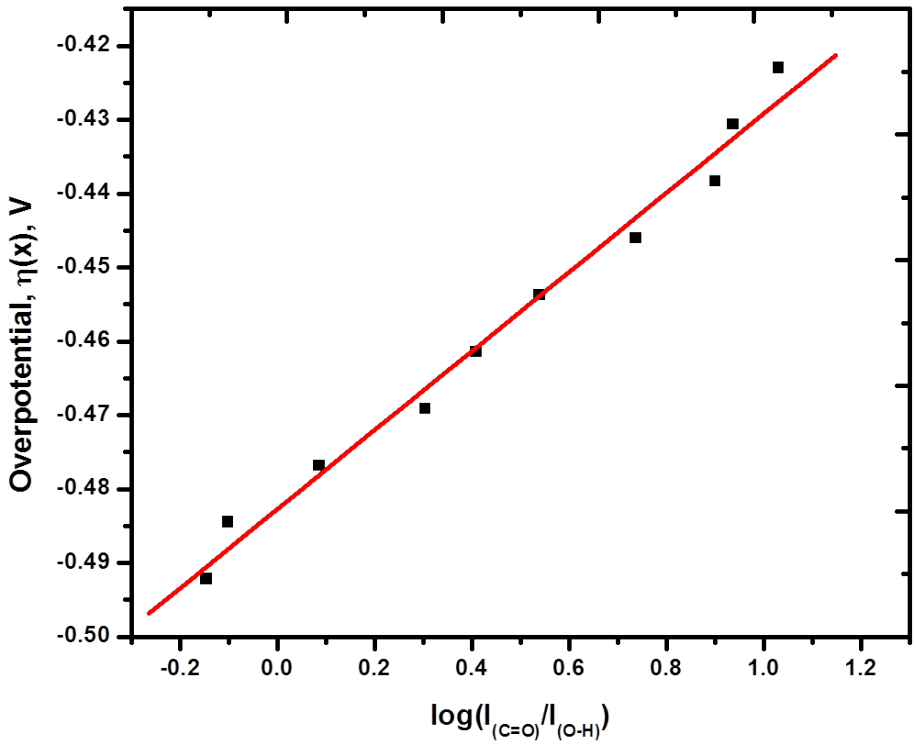

Figure 2.3.15. Plot of η(x) as a function of log ($I_{(C=O)}/I_{(O-H)}$). The data was obtained from figure 2.3.14.

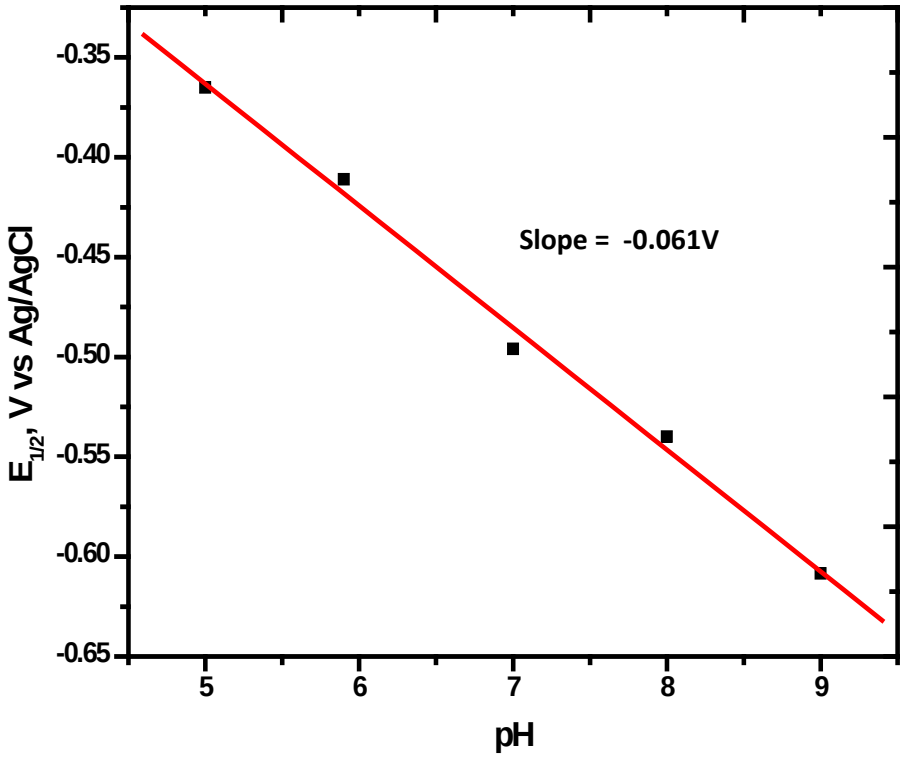

Figure 2.3.16. Plot of $E_{1/2}$ as a function of pH obtained from cyclic voltammograms of 2-AQS modified gold electrodes.

The dependence of the Raman response on potential was also investigated on a 2-AQS-modified Ag electrode in a three-electrode set up as the results are shown in figure 2.3.17. Once again, the C=O stretch at 1656cm^{-1} attenuated while the O-H bend at 1423cm^{-1} grew in intensity with increasing negative applied potential indicating that Raman spectral changes observed in the bipolar setup are due to changes in the interfacial potential along the surface of the bipolar electrode. The Raman response profile as a function of position on the 2-AQS-

modified Ag bipolar electrode was then presented in terms overpotential η(x) (top x-axis) according to equation 1.5.2 as shown in figure 2.3.18.

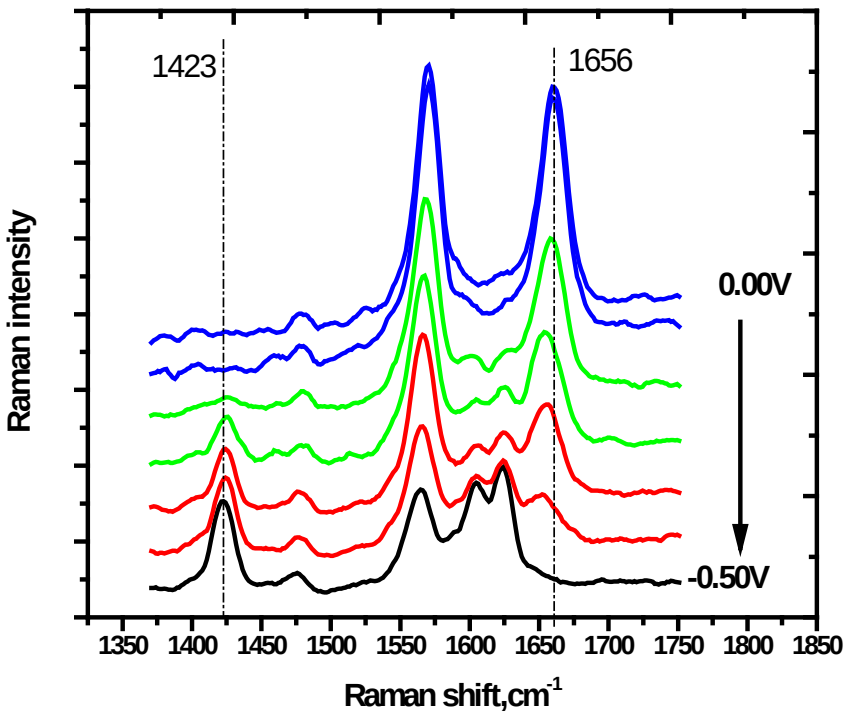

Figure 2.3.17 *In situ* SERS spectra of 2-AQS SAM on an Ag working electrode recorded in B&R buffer (pH 7.00) at different potentials in a three-electrode setup

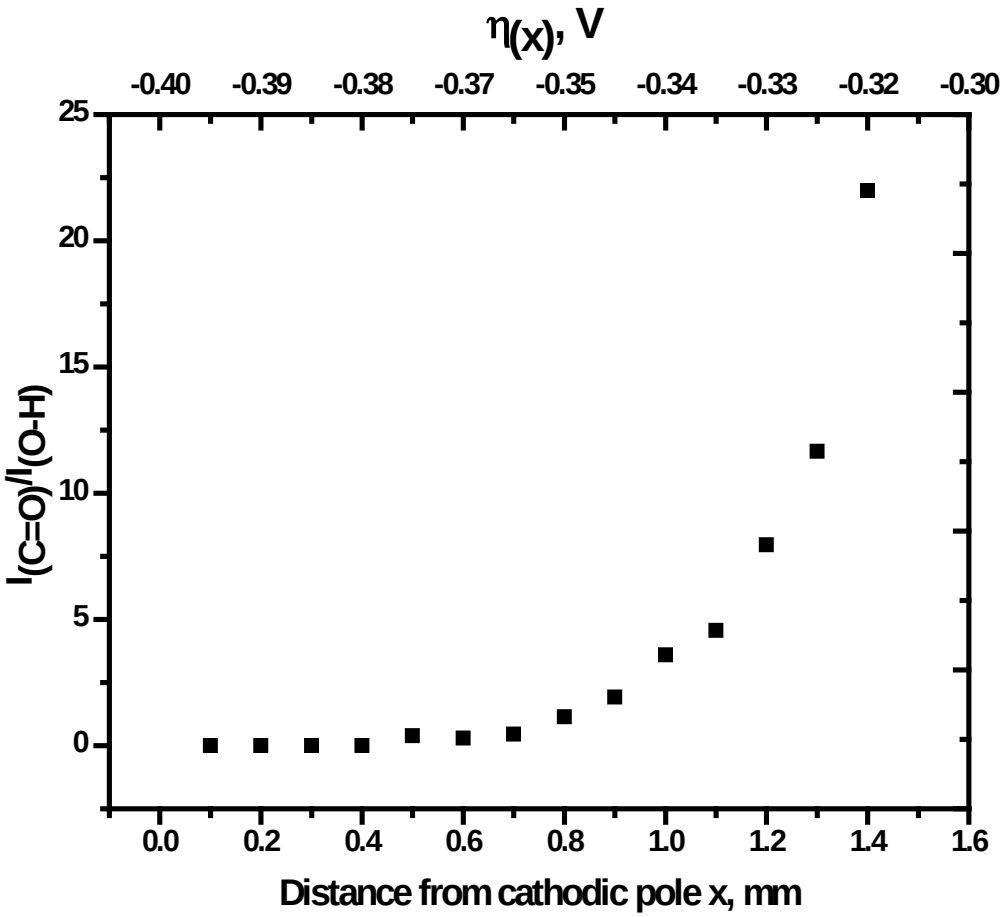

Figure 2.3.18. Relative amount of 2-AQS to 2-H_2AQS ($I_{(C=O)}/I_{(O-H)}$) as a function of position (bottom x-axis) and overpotential, $\eta_{(x)}$ (top x-axis) on Ag bipolar electrode.

Figure 2.3.19 shows the plot of overpotential as a function of the logarithm of Raman peak intensity ratio generated according to equation 2.3.5. The slope of -0.031V was obtained from this plot is in agreement with the value of -0.030V expected for a two-electron redox reaction. The formal potential obtained from the intercept is -0.43V which is in agreement with the value obtained from the cyclic voltammogram.

Cyclic voltammograms were also recorded for the 2-AQS-modified Ag electrode in the pH range of 5-9 in a three-electrode setup and a plot of the changes in formal potential as function of pH is shown in figure 5.3.20. A slope of -0.055V was obtained from this plot. This finding together with the results from the measurements made on the bipolar electrode suggests a two-electrode, two-proton reaction for 2-AQS on Ag.

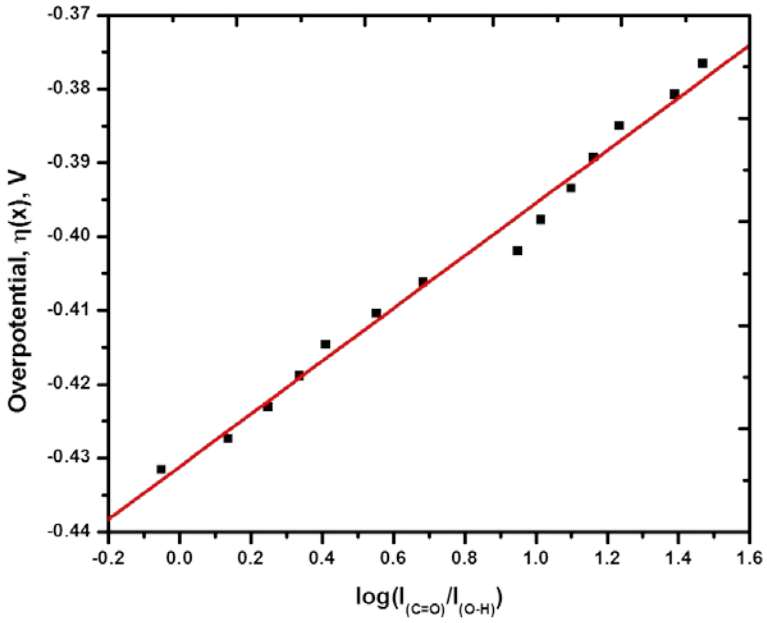

Figure 2.3.19. Plot of η(x) as a function of log ($I_{(C=O)}/I_{(O-H)}$). The data was obtained from figure 2.3.18.

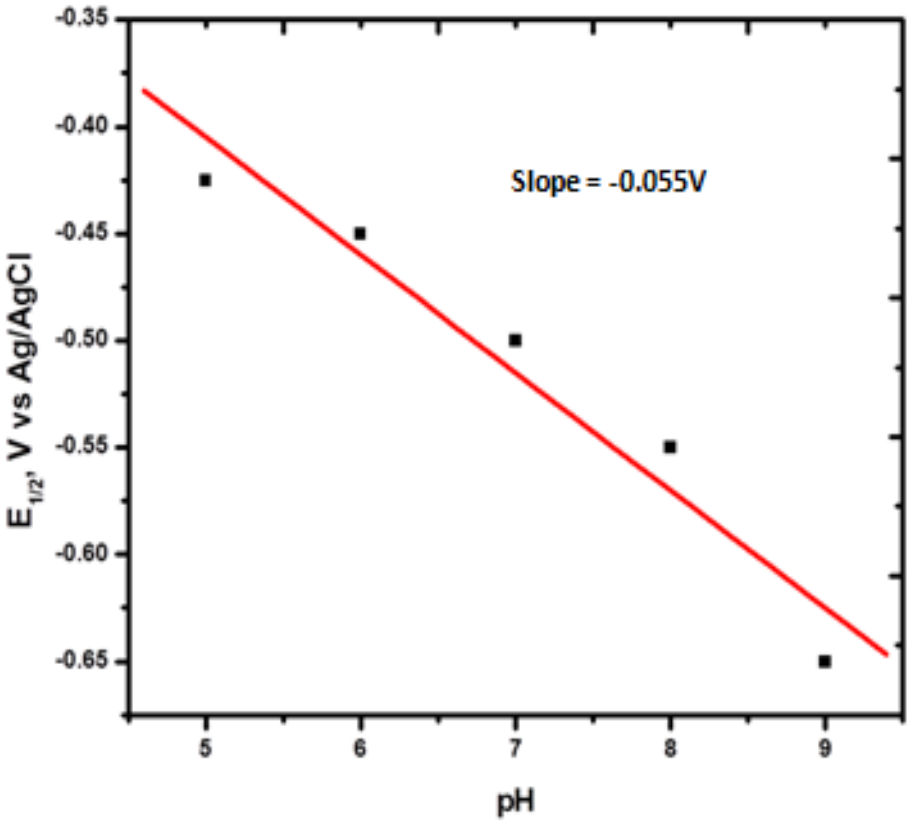

Figure 2.3.20. Plot of $E_{1/2}$ as a function of pH obtained from cyclic voltammograms of 2-AQS modified gold electrodes.

2.3.3. Effect of varying the applied potential

Figure 2.3.21 demonstrates the effect of the applied voltage, E_{appl} on reaction gradients on

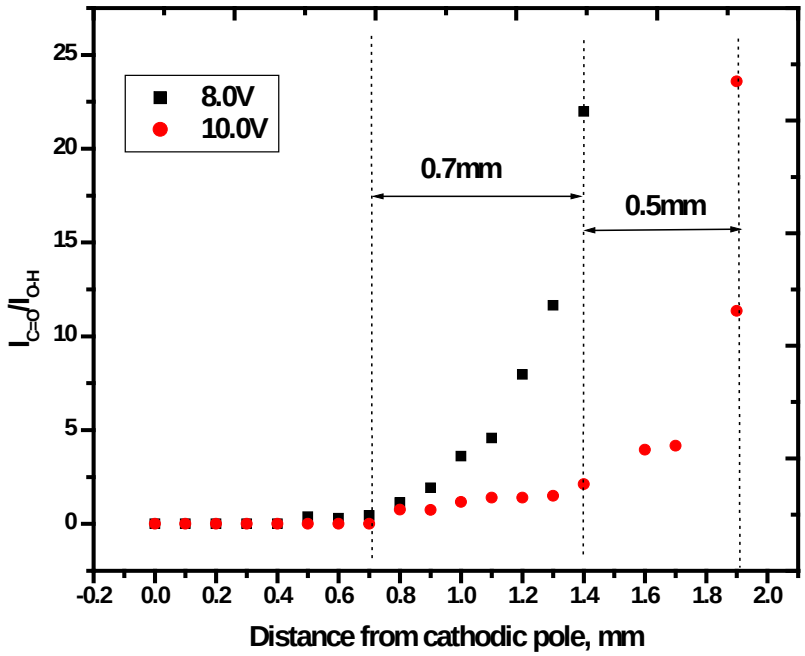

Figure 2.3.21 Changes in the relative amount of 2-AQS to 2-H_2AQS, $I_{(C=O)}/I_{(O-H)}$, as a function of applied potential, E_{appl}.

bipolar electrodes. When the voltage was increased from 8V to 10V, the width of the gradient decreased and the position of the gradient shifted towards the center of the electrode surface. This behavior can be attributed to a larger potential drop across the solution at higher applied voltages as demonstrated in figure 2.3.3.

2.4 Conclusion

Preliminary results on the spatial distribution of the solution potentials in a bipolar electrochemical cell have been presented in this work. These results will facilitate the understanding of faradaic reactions occurring on bipolar electrodes that will provide insight concerning the possibility to control and optimize redox reactions for analytical purposes and gradient formation. It was also shown that Raman spectroscopy is a reliable reporter electrochemical reactions on bipolar electrodes. Because the extent of redox reactions is depends on the potential difference experienced by the redox molecules, the Raman response can be used to interrogate the interfacial potential difference that exists between the bipolar electrode and the solution. It was also demonstrated information that can be obtained from the three-electrode setup can be obtained simply from the geometry of the bipolar electrode. To demonstrate the versatility of the bipolar effect, experiments were carried out on 2-AQS SAM modified Au and Ag bipolar electrodes. Similar patterns were observed on both electrodes demonstrating that the bipolar effect can be observed on any conducting substrate. Finally it was demonstrated that the position and width of the reaction gradient can be easily controlled

References

1) Whitesides, G. M.; Xia, Y. Annnu. *Rev. Mater. Sci* **1988,** 28, 153-184.

2) Piner, R. D.; Zhu, J.; Xu, F.; Hong, S.; Mirkin, C. A. *Science* **1999,** 283, 661-663.

3) Van Dover, R. B.; Scheemeya, L. F.; Fleming, R. M. *Nature **1998,*** 392, 162-164.

4) Jandeleit, B.; Schaefer, D. J.; Powers, T. S.; Turner, H. W.; Weinberg, W. H. *Angew. Chem. Int. Ed.* **1999,** 2494-2532.

5) Miller, O. J.; Harrak, A. E.; Mangeat, T.; Baret, J-C.; Frenz, L.; Debs, B. E.; Mayot, E.; Samuels, M. L.; Rooney, E. K.; Dieu, P.; Galvan, M.; Link, D. R.; Griffiths, A. D. *Proc. Natl. Acad. Sci. U. S. A.* **2012,** 109, 378-383

6) Mrksich, M.; Grunwell, J. R.; Whitsides, G. M. *J. Am. Chem. Soc.* **1995,** 117, 12009-12010.

7) Tidwell, C. D.; Ertel, S. I.; Ratner, B. D.; Tarasevich, B. J.; Arte, S.; Allara, D. L. *Langmuir* **1997,** 13, 3404-3413.

8) Carter, S. B. *Nature* **1965,** 208, 1183-1187.

9) Chaudhury, M. K.; Whitesides, G. M. *Science* **1992,** 256, 1539-1541.

10) Riepl, M.; Ostblom, M.; Lundstrom, I.; Svensson, S. C. T.; Deiner van de Gon, A. W.; Schferling, M.; Liedberg, B. *Langmuir* **2005,** 21, 1042-1050.

11) Morganthaler, S.; Lee, S.; Zurcher, S.; Spencer, N. D. *Langmuir* **2003,** 19, 10459-10462.

12) Tomlinson, M. R.; Efimenko, K.; Genzer, J. *Macromolecules* **2007,** 39, 9049-9056.

13) Jeon, N. L.; Dertinger, S. K. W.; Chiu, D. T.; Choi, I. S.; Stroock, A.; Whitesides, G. M. *Langmuir* **2000,**16, 8311-8316.

14) Park, S. H.; Krull, U. *Anal. Chim. Acta* **2006,** 564, 133-140.

15) Hansen, T.S.; Lind, J. U.; Dauggaard, A. E.; Hvilsted, S.; Andresen, T. L.; Larsen, N. B. *Langmuir* **2010,** 26, 16171-16177.

16) Inagi, S.; Ishiguro, Y.; Atobe, M.; Fuchigami. *Angew. Chem. Int. Ed.* **2010,** 49, 10136-10139

17) Fan, F. R. F.; Yang, J. P.; Cai, L. T.; Price, D. W.; Dirk, S. M.; Kosynkin, D. V.; Yao, Y. X.; Rawlett, A. M.; Tour, J. M.; Bard, A. J. *J. Am. Chem. Soc.* **2002,** 124, 5550-5560.

18) Darwish, N.; Diez-Perez, I.; Gooding, J. J.; Da Silva, P.; Tao, N.; Paddon-Row, M. N. *Angew. Chem. Int. Ed.* **2012,** 51, 3203-3206

19) luo, W.; Chan. E. W. L.; Yousaf, M. N. *J. Am. Chem. Soc.***2010,** 132, 6890-6891.

20) Wong, E. L. S.; Gooding, J. J. *Anal. Chem.* **2003,** 75, 3852.

21) Kang, S. K.; Lee, O-S.; Chang, S-K.; Chung, D. S.; Kim, H.; Chung, T. D. *J. Phys. Chem. C* **2009,** 113, 19981-19985.

22) Nicholson, R. S.; Shain, I. *Anal. Chem.* **1964,** 36, 706-723

23) Nishiyama, K.; Tahara, S-i.; Uchida, Y.; Tanoue, S.; Taniguchi, I. *J. Electroanal. Chem.* **1999,** 478, 83-91.

24) Stolberg, L.; Lipkowski, J.; Irish, D. E. *J. Electroanal. Chem.* **1991,** 300, 563-584.

25) Brolo, A. g.; Irish, D. E.; Szymanski, G.; Iipkowski, J. *Langmuir*, **1998,** 14, 517-527.

Chapter 3

Spectroelectrochemical Characterization of Cobalt Oxide

3.1 Introduction

Cobalt oxide materials have been extensively studied due to their numerous interesting properties which have been exploited for applications such heterogeneous catalysts[1-4], electrochromic[5-7] and magnetic[8-11] devices. As a mixed oxide, $LiCoO_2$ is currently being used as cathode materials for rechargeable Li-ion batteries[12-14] while thin films of CoO(OH) electrodeposited on NiO(OH) are used to stabilize and enhance the conductivity of the positive electrode in rechargeable alkaline Ni-Cd batteries[15-17].

Several methods for the preparation of cobalt oxide species have been developed. These include thermal decomposition of cobalt salt[18], chemical[19, 20] and photochemical[21] synthesis, reactive sputtering in O_2 plasma[22], chemical vapor deposition[23], as well as electrochemical techniques. Electrochemical methods are particularly attractive because they allow synthesis at low temperatures which are compatible with most substrate materials and large-area films can be easily prepared. Moreover, by controlling the deposition parameters, it is possible to achieve a high level of tunability in the chemical composition, film thickness, oxidation states as well as optical and magnetic properties of electrodeposited materials. For example cathodic electrodeposition from dissolved cobalt salts gives rise to cobalt hydroxide, $Co(OH)_2$[24] whereas anodic electrodeposition gives rise to oxides such as Co_3O_4[25] and CoO(OH)[26]. In this work, we investigate the effect of electrode potential, film thickness, substrate on the nature and properties

of electrodeposited cobalt oxide films. The amorphous nature of the deposited films makes is hard to characterize using x-ray powder diffraction technique. Therefore Raman spectroscopy was used to evaluate the cobalt oxide films. The effect of laser power on the films was also investigated.

3.2 Materials and Methods

3.2.1 Materials

$Co(NO_3)_2$, $NaNO_3$ (>99% ACS reagent, Aldrich Chemical) and KOH (87.1%, Fisher Scientific Company) were used as received. The driver electrodes for the bipolar electrochemical cell were made from stainless steel foil (Alfa Aesar). Millipore-Q purified deionized water (18.2MΩ·cm) was used to prepare all solutions and rinse electrodes.

3.2.2 Substrate preparation

Gold foil electrodes were mechanically polished successively with 400 -, 600 -, 800 - and 1200 - grit SiC paper sonicated in distilled water for 5 min. They were then rinsed sequentially with distilled water, absolute ethanol and distilled water. A layer of cobalt oxide was formed on the gold electrode electrodeposition from solutions containing dissolved Co^{2+} ions. The as- deposited cobalt oxide film was rinsed with distilled water and dried in a flowing stream of Nitrogen and used as the working in subsequent measurements in 0.1M KOH or 0.1M NaOH.

3.2.3 Electrochemistry

All electrochemical measurements were performed using a standard three-electrode configuration in a home-built glass cell. In all cases we used a gold foil as the working electrode, a Platinum counter electrode and either a Ag/AgCl(sat) (Bioanalytical Systems, Inc.) or a Hg/HgO (3M) (Gamry Instruments) reference electrode. The electrochemical cell was controlled using an Epsilon electrochemical work station (Bioanalytical Systems, Inc.).

3.2.4 Raman Microscopy

Raman scattering was excited using the 514nm output (ca. 34mW) from an air cooled argon ion laser (model 163-C42, Spectra-Physics lasers, Inc.). The spectra were collected and analyzed using a Renishaw InVia Raman microscope and associated software. A leica 50x (0.75NA) objective was used to focus the excitation light onto the sample. The scattered radiation was collected by the same objective through a spectrometer with entrance slits of about 12-15μm. The exposure time for each spectrum was 30 seconds and only a single scan was made. A 1200 lines mm^{-1} grating was used for all measurements providing a resolution of $\pm 1 cm^{-1}$. The instrument was calibrated for the Raman shift by referencing to that of silicon.

3.3 Result and discussion

3.3.1 Cathodic Deposition

Figure 3.3.1 shows the Raman spectrum of cobalt hydroxide. This compound can crystallize into two polymeric forms, green/blue metastable α-$Co(OH)_2$ and pink β-$Co(OH)_2$ hexagonal layered structures[27]. The β-phase shows a brucite structure with cobalt ions occupying the alternate rows of the octahedral sites while the α-phase shows a hydrotalcite-like structure consisting of

positively charged β-$Co(OH)_{2-x}$ layers intercalated with balancing anions from the electrolyte. The as-prepared α-$Co(OH)_2$ precipitates at the cathode in the presence of Co^{2+} ions under basic condition and its Raman spectrum is shown in figure 3.3.1 (left). It is characterized by two features at 454 and 519cm^{-1}. These bands have been attributed to the Co-O (A_g) symmetric stretching mode and the O-Co-O bending

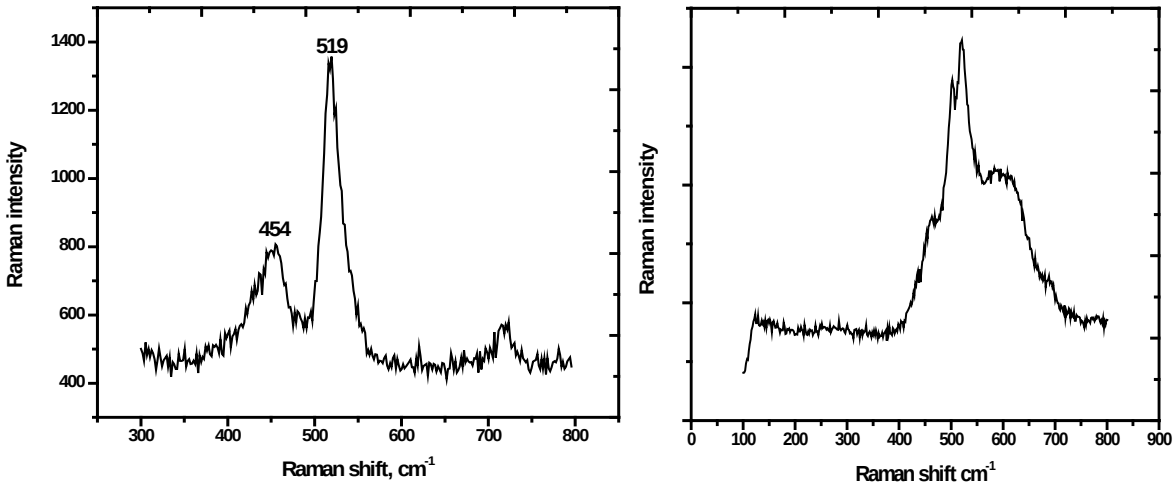

Figure 3.3.1 Raman spectrum of α-$Co(OH)_2$ (left) and β-$Co(OH)_2$ (right)

respectively[28]. Also shown in figure 3.3.1 (right) is the Raman spectrun of commercially available β-$Co(OH)_2$. It is similar to α-$Co(OH)_2$ except that the features are much broader with an overlap between the bands at 454 and 519cm^{-1}.

Considerable effort has been invested into the synthesis of cobalt hydroxide which show different properties depending on their shape and microstructure. Needle-like structures have been prepared and converted to cobalt oxide nanotubes that exhibit ultra high electrochemical capacity that can be used as electrodes for Li-ion batteries[29].

3.3.2 Anodic deposition

Figure 3.3.2.1 shows the Raman spectrum of a cobalt oxide film deposited on a Au substrate from a solution containing 0.5mM $Co(NO_3)_2$. It is characterized by features at 197, 485, 520, 620 and 691cm^{-1}. These features are assigned to F_{2g}, E_g, F_{2g}, F_{2g} and A_{1g} respectively[30] and have been assigned to Co_3O_4 which crystallizes in the spinel structure. This spectrum is very similar to that of commercial Co_3O_4.

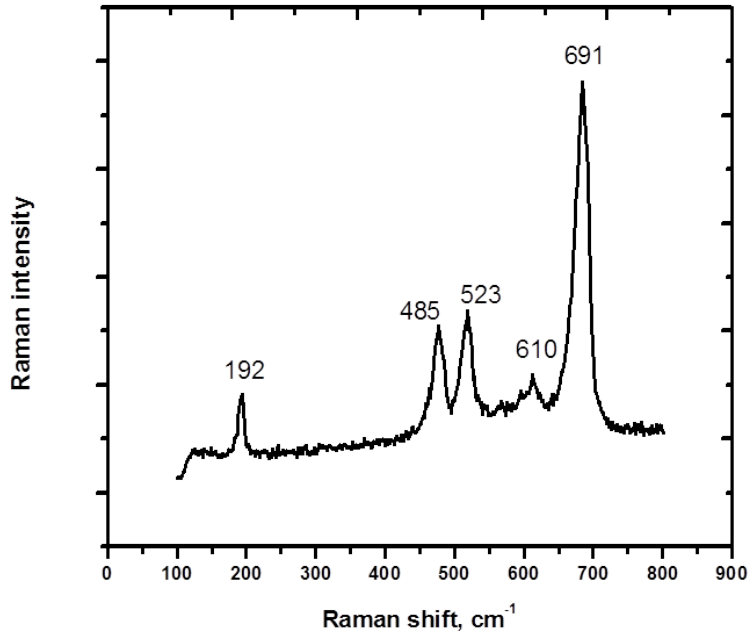

Figure 3.3.2.1 Raman spectrum of electrodeposited cobalt oxide (Co_3O_4) from 0.5mM $Co(NO_3)_2$ in borate buffer (pH 9.2)

Cobalt oxide species have recently received tremendous attention as potential candidates for water oxidation catalysts[3]. A detailed study of their catalytic activity is reported in chapter 4. They are expected to replace costly noble metal oxides in commercial electrolyzers and fuel cells because cobalt is an earth-abundant metal and is therefore inexpensive. The oxidation-induced precipitation cobalt oxide species can be used to prepare water oxidation electrocatalyst as demonstrated in the cyclic voltammogram shown in figure 3.3.2.2 (left). In the presence of Co^{2+} ions, a broad feature centered around 0.7V (enlarged CV in figure 3.3.2.2 (right) is observed on the anodic scan followed a strong catalytic wave. Notice the absence (figure 3.3.2.2 (left), red line) of the catalytic wave in solutions containing no Co^{2+} ions. This demonstrates the cobalt oxide is responsible for the catalytic wave.

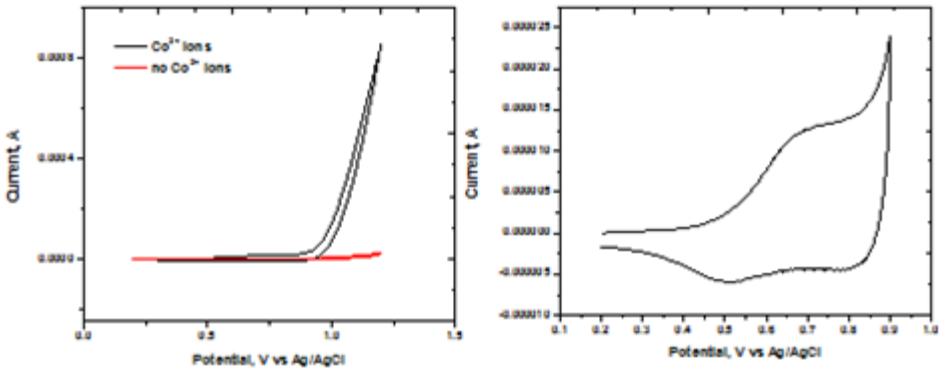

Figure 3.3.2.2 Cyclic voltammogram (left) of glassy carbon electrode in 0.1M borate buffer alone, pH 9.2 (red), 0.5mM cobalt nitrate in 0.1M borate buffer pH 9.2 (black). Cyclic voltammogram (right) at higher sensitivity to reveal redox feature prior to catalytic wave in the presence of cobalt ions.

In order to understand the mechanism of water oxidation by cobalt oxide species considerable effort has been devoted to the identification of the active phase of the catalyst. Recently, electron paramagnetic resonance spectroscopy studies have shown that Co^{4+} centers are required to catalyze the oxygen evolution reaction[31, 32].

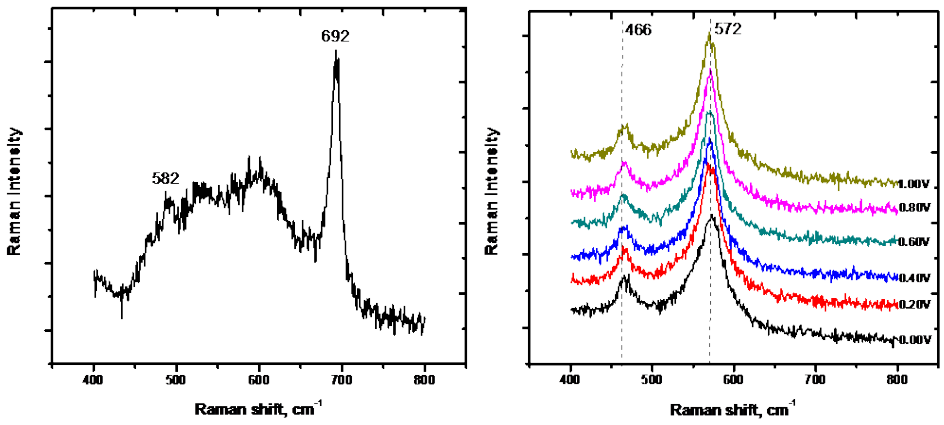

Figure 3.3.2.3 Raman spectrum of as-deposited cobalt oxide from an electrolytic solution containing 12mM $Co(NO)_3$ and 0.1M sodium acetate buffer (pH 7.80) (left) and as-deposited cobalt oxide recorded as a function of applied potential in 0.1M KOH (right)

In this work, in situ Raman spectroscopy was used to investigate the composition of the cobalt oxide deposited on gold foil from a solution containing 12mM $Co(NO)_3$ and 0.1M sodium acetate buffer (pH 7.80). Figure 3.3.2.3 (left) shows the *in situ* Raman spectrum of the as-deposited cobalt oxide at open circuit potential. The spectrum is very similar to that Co_3O_4 presented in figure 3.3.2.1 Because the Co_3O_4 easily dissolves under acidic conditions, it was further investigated in 0.1M KOH. Figure 3.3.2.3 (right) shows the in situ Raman spectra recorded as a function of potential. It can be seen that Co_3O_4 is immediately converted to a new species even at 0.00V and the spectrum remains constant upon increasing the potential.

This implies that the composition of the deposited films remains constant once oxidized at 0.00V. The two features observed at 466 and 572cm^{-1} have been respectively assigned to the E_g and A_{1g} modes of CoO_2 based on Raman studies on the delithiation of $LiCoO_2$. This is in agreement with the fact that the active phase of the cobalt oxide catalysts contains Co^{4+} centers.

Similar studies have been performed on bulk cobalt using bipolar electrochemistry and the results are presented in chapter 4. We used bulk cobalt in this study because the electrodeposited cobalt oxide films show poor adhesion to the Au substrate and easily peel off with increasing film thickness.

3.3.3 Electrochromic Behavior of Cobalt Oxide

Cobalt oxide species prepared by electrodeposition from a solution containing 12mM $CoCl_2$, 0.5M NaOH and 12mM gluconate. The electrochromic behavior of the as-prepared cobalt oxide as investigated in 0.5M NaOH by recording cyclic voltammograms between 0.0V and 0.8V and the results are presented in figure 3.3.3.1

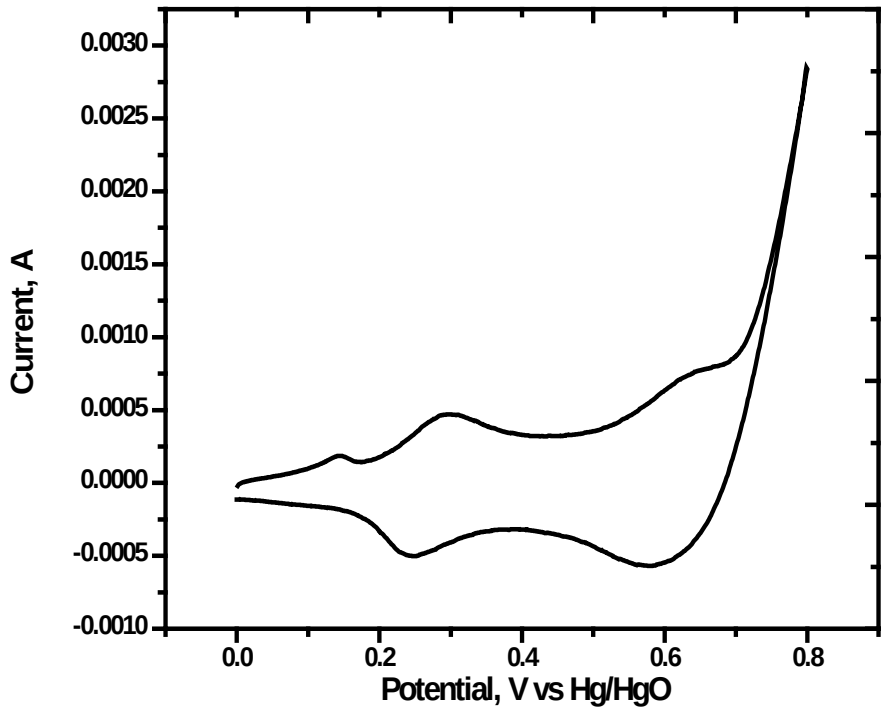

Figure 3.3.3.1 Cyclic voltammogram of as deposited cobalt oxide in 0.1M NaOH.

The redox transitions in the voltammogram were also accompanied by color changes that were reversible between anodic and cathodic scans. The two major colors were reddish green (translucent) at more negative potentials and dark blue (opaque) at more positive potentials as shown in figure 3.3.3.2. The three features observed in the cyclic voltammogram on the anodic scan at 0.15V, 0.30V and 0.65V can be assigned to the formation of Co_3O_4, CoO(OH) and CoO_2 respectively. These features are followed by a strong catalytic wave at about 0.70V associated with oxygen evolution. The cathodic scan shows three peaks at 0.60V, 0.23V and 0.1V and

Figure 3.3.3.2 Photograph of as deposited films of cobalt oxide recorded during cyclic voltammetry in 0.1M NaOH.

are associated to the formation of CoO(OH), Co_3O_4 and CoO (or $Co(OH)_2$) respectively due to the reduction of species formed during the anodic scan.

Cobalt oxide species are currently being investigated as anodic electrochromic materials to replace costly tungsten oxide (WO_3) for electrochromic devices such as "smart" windows in buildings and rearview mirrors in cars[6, 36].

3.3.4 Effect of Laser Power on Cobalt Oxide Film

Due of the inherent weakness of the Raman scattering effect, intense light sources such are lasers are being used as the excitation source. Although the effect of lasers can be damaging to

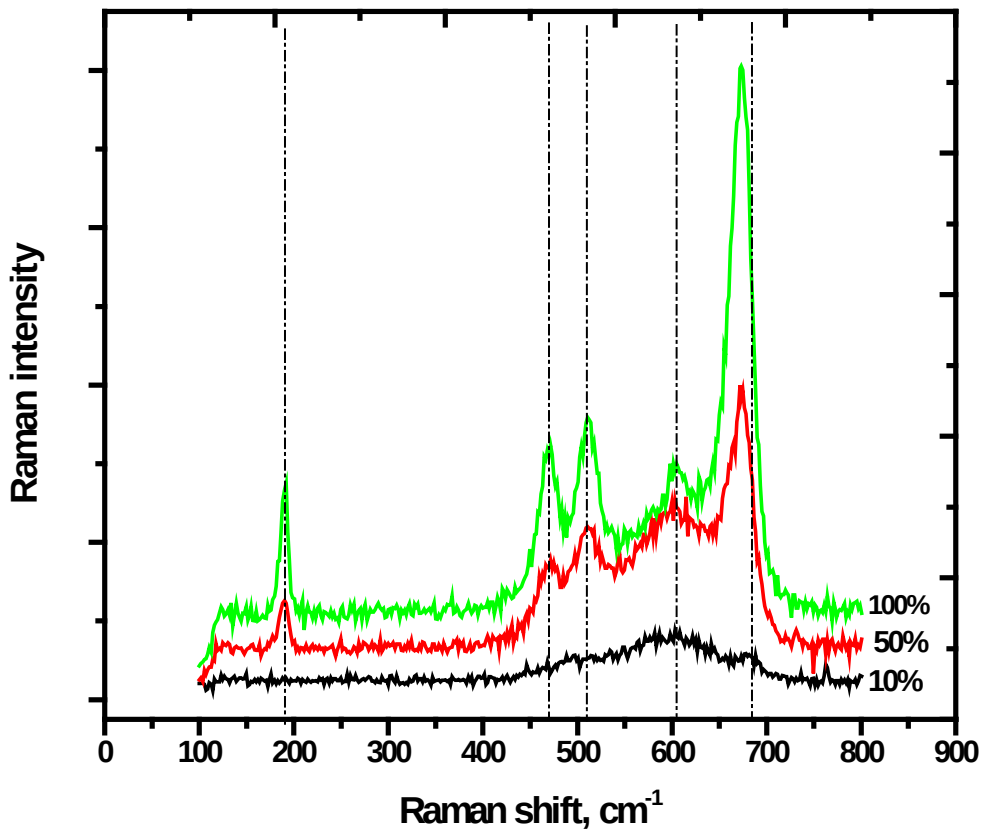

Figure 3.3.4.1. Raman spectra of as-deposited cobalt oxide as a function of laser power. The laser power was 33mW.

certain samples as a result of localized increase in temperature, the sensitivity of laser irradiation can be of advantage if laser-induced crystallization becomes possible[37, 38]. The heating effect is very common in micro-Raman experiments because the laser is focused on a spot with a diameter of only a few micrometers. Sample deterioration and structural changes due to heating by the laser depend on parameters such as exposure time, laser wavelength, laser power, surface

area, color and thermal conductivity. The effect of laser power on cobalt oxide compounds has recently been investigated may serve as a quick diagnostic tool for amorphous phases[39, 40]. We recorded the Raman spectrum of as-deposited cobalt oxide as a function of laser power and the results are shown in figure 3.3.4.1. It can be seen that the peaks become sharper and more intense at higher laser powers. This clearly demonstrates structural changes in the cobalt oxide material which we associate to the transformation from an amorphous phase at low laser powers to a crystalline phase at higher laser powers. It has been suggested that improved crystallinity at higher laser powers is accompanied by the oxidation of CoO with a face-centered cubic structure to Co_3O_4 with a spinel-type structure[39].The transformations in figure 3.3.4.1 are also accompanied by the peaks being shifted to lower frequencies at higher laser powers . This finding is consistent with reports that increased temperatures are known to cause a red-shift of Raman active vibrations in metal oxides[40].

3.4 Conclusion

It has been shown that various forms of cobalt oxide can be prepared from solutions containing Co^{2+} ions depending on the electrodeposition potential. Cathodic potentials yield cobalt hydroxide $Co(OH)_2$ whereas anodic potentials give rise to predominantly cobalt oxide species such as Co_2O_3, Co_3O_4 CoOOH and CoO_2 with Co_3O_4 being the thermodynamically stable oxide at open circuit potentials. It was also shown that cobalt oxide exhibits different colors at different potentials, making it a potential candidate for electrochromic devices. Finally, the effect of laser heating on cobalt oxide was investigated. It was observe that cobalt oxides materials undergo a phase transition from amorphous to crystalline at high laser powers possibly accompanied by oxidation.

References

1) Castro, E. B.; Gervasi, C. A.; Vilche, J. R. *Appl. Electrochem.* **1998,** 28, 835-839.

2) Singh, R. N.; Mishra D.; Anindita*;* Sinha A. S. K.; A. Singh, *A. Electrochem. Commun.* **2007,** 9, 1369–1373.

3) Kanan, M. W.; Nocera, D. *Science* **2008,** *321,* 1072-1075.

4) Esswein, A. J.; McMurdo, M. J.; Rpss, P. N.; Bell, A. T.; Tilley, T. D. *J. Phys. Chem. C* **2009,** 113, 15068-15072.

5) Yoshino, T.; Baba, N. *Solar Energy Materials and Solar cells* **1995,** 39, 391-397.

6) Shim, H-S.; Shinde, V. R.; Kim, H. J.; Sung, Y-E.; Kim, W. B. *Thin Solid films* **2008,** 516, 8573-8578.

7) Con, H-P.; Ren, X-C.; Yao, H-B.; Wang, P.; Colfen, H.; Yu, S-H. *Adv. Mater.* **2012,** 24, 1309-1315.

8) Yarger, M. S.; Steinmiller, E. M. P.; Choi, K. S. *Chem. Commun.* **2007,** 0, 159-161.

9) Keene, T. D.; Light, M. E.; Hursthouse, M. B.; Price, D. J. *Dalton Trans.* **2011,**40, 2983-2994.

10) Takada, S.; Fujii, M.; Kohiki, S.; Babasaki, T.; Deguchi, H.; Motome, M.; Oku, M. *Nano. Lett.* **2001,** 1, 379-382.

11) Salabas, E. L.; Rumplecker, A.; Kleitz, F. Radu, F.; Schueth, F. *Nano. Lett.* **2006,** 6, 2977-2981

12) Markevich. E.; Salitra, G.; Aurbach, D. *Electrochem. Comm.* **2005,** 7, 1298-1304.

13) Park, Y.; Kim, H-K.; Kim, J.Y.; Eom, I-Y.; Jeong, Y. U.; Kim, M. S.; Lee, S. M.; Choi, H. C.; Jung, Y. M. *Vib. Spectrosc.* **2010,** 53, 60-63.

14) Cabana, J.; Moncoduit, L.; larcher, D.; Palacin, M. R. *Adv. Mater.* **2010,** 22, E170- E192.

15) Kleinsorgen, K.; Lichtenberg, *J. Power Sources* **1996,** 62, 207-211.

16) Mendoza, L.; Albin, V.; Cassir, M.; Galtayries, A. *J. Electroanal. Chem.* **2003,** 548, 95-107.

17) Li, X.; Dong, H.; Zhang, H. *Mater. Chem. Phy.* **2008,** 111, 331-334.

18) Rakhi, R. B.; Chen, W.; Cha, D.; Alshareef, H. N *Nano Lett.* **2012,** 12, 2559-2567,

19) Kandalkar, S. G.; Lokhande, C. D.; Mane, R. S.; Han, S-H *Appl. Surf. Sci.* **2007,** 253, 3952-3956

20) Kandalkar, S. G.; Dhawale, D. S.; Kim, C-K.; Lokhande, C. D. *Synth. Met.* **2010,** 160, 1299-1302

21) Alvarado, S. R.; Guo, Y.; Reberu, T. P.; Bakac, A.; Vela, J. J. Phys. Chem. C. 2012, 116, 10382-10389.

22) Schumacher, L. C.; Holzhueter, I. B.; Hill, I. R.; Dignam, M. *J. Electrochim. Acta* **1990,** 35, 975-984.

23) Tyczkowski, J.; Kapica, R.; Lojewska, *J. Thin Solid Films* **2007,** 515, 6590-6595.

24) McNally, E. A.; Zhitomirsky, I.; Wilkinson, D. S. *Mater. Chem. Phys.* **2005,** 91, 391-398.

25) Vital, R.; Gomathi, H.; Rao, G. P. *J. Electroanal. Chem.* **2001,** 497, 47-54

26) Pauporte, T.; Mendoza, L.; Cassir, M.; Bernard, M. C.; Chivo, J. *J. Electrochem. Soc.* **2003,** 2, C49-C53.

27) Ma, R.; Liu, Z.; Takada, K.; Fukuda, K.; Ebina, Y.; Bondo, Y.; Sasaki, T.; Inorg. Chem. 2006, 45, 3964-3969.

28) Yang, J.; Liu, H.; Martens, W. N.; Frost, R. *J. Phys. Chem. C.* **2010,** 114, 111-119.

29) Lou, W. X.; Deng, D.; Lee, J. Y.; Feng, J.; Archer, L. A. *Adv. Mater.* **2008,** 20, 258.

30) Khadzhiev, V.; Iliev, M.; Vergilov, I. *J. Phys. C: Solid State Phys.* **1988,** 21, L199.

31) McAlpin, J. G.; Surendranath, Y.; Dinca, M.; Stich, T. A.; Stoian, S. A.; Casey, W. H.; Nocera, D. G.; Britt, R. D. *J. Am. Chem. Soc.* **2010,** 132, 6882-6883.

32) Gerken, J. B.; McAlpin, J. G.; Chen, J. Y. C.; Rigsby, M. L.; Casey, W. H.; Britt, R. D.; Stahl, S. S. *J. Am. Chem. Soc.* **2011,** 133, 14431-14442

33) Inaba, M.; Iriyama, Y.; Ogumi, Z.; Todzuka, Y.; Tasaka, A. J. *Raman Spectrosc.* **1997,** 28, 613-617.

34) Markevich, E.; Salitra, G.; Aurbach, D. *Electrochem. Commun.* **2005,** 7, 1298-1304

35) Park, Y.; Kim, N. H.; Kim, J. Y.; Eom, I-Y.; Jeong, Y. U.; Kim, M. S.; Lee, S. M.; Choi, H. C.; Jung, Y. M. *Vib. Spectrosc.* **2010,** 53, 60-63.

36) Svegl, F.; Orel, B.; Hutchins, M. G.; Kalcher, K. *J. Electrochem. Soc.* **1996,** 143, 1532-1539.

37) Witke, K.; Klaffke, D.; Skopp, A.; Schreckenbach, J. P. *J. Raman. Spectrosc.* **1998,** 29, 411.

38) Laikhtman, A.; Hoffman, A. *J. Appl. Phys.* **1997,** 82, 243-248.

39) Gallant, D.; Pezolet, M.; Simard, S. *J. Phys. Chem. B* **2006,** 6871-6880.

40) Shebanova, O. N.; Lazor, P. *J. Raman Spectrosc.* **2003,** 34, 845-852.

Chapter 4

A Rapid Screening Platform for the Composition and Catalytic Activity of Cobalt Oxide Species for Water Oxidation

4.1 Introduction

The release of greenhouse gases into the environment from fossil fuels and the increased energy consumption due to population growth and industrial development has motivated scientist all over the globe to develop efficient technologies in order to produce carbon free and renewable energy alternatives. Of all the renewable energy sources available, only sunlight has the capacity to meet the current energy demand[1]. However, the diurnal nature of the sun requires that its energy be tapped and stored so that it can be used on non-sunny days[2]. One approach to achieve this goal is the sunlight-driven electrochemical splitting of water, thereby storing solar energy in the chemical bonds of the hydrogen and oxygen[1-5] that are produced according to the following reactions.

$$Anode: \quad 2H_2O \rightarrow O_2 + 4H^+ + 4e^- \qquad E_a = 1.23V \ vs. \ SHE \tag{4.1.1}$$

$$Cathode: \quad 4H^+ + 4e^- \rightarrow 2H_2 \qquad E_C = 0.0V \ vs \ SHE \tag{4.1.2}$$

$$Overall: \quad 2H_2O \rightarrow O_2 + 2H_2 \qquad E_{rxn} = -1.23V \qquad 4.1.3$$

The hydrogen produced can then be used in applications such as fuel cells. Of the two half reactions shown above, the oxygen evolution reaction is very demanding due to its complex nature. As a result, instead of the thermodynamic potential of 1.23V[6], a potential of about 1.85 is usually needed to effect water splitting. This corresponds to an overpotential of 0.62. To help reduce this overpotential and therefore split water more efficiently, a catalyst must be employed. Current catalysts being used in this process include precious metals such as Pt, Ru and Ir and their oxides[7-10]. Although there have been several reports on the use of cobalt oxide/hydroxide[11-13] coatings for water oxidation, they were not thoroughly investigated until recently following the work of Nocera and coworkers [14]. Unlike Pt, Ru and Ir, cobalt is abundant and therefore inexpensive. As with any other catalyst knowledge of the mechanism of water splitting by this catalyst is imperative for optimizing operating conditions and also for designing new catalysts. Such knowledge depends on the identification and characterization of the active form of the catalyst under given conditions. Therefore a lot of attention has been focused on the changes in composition and structure of cobalt oxide species as a function of potential and how these changes correlate with the activity of the catalyst on water oxidation. The groups of Nocera[15]and Stahl[16] have used X-ray and EPR spectroscopy respectively to characterize cobalt oxide species obtained at various potentials. Samples obtained under oxygen evolution conditions were found to contain Co(VI) species leading to the conclusion that Co(IV) centers are required for water oxidation. In both studies the different cobalt oxide species were prepared sequentially at different applied potentials and were characterized *ex situ*. However, sequential processes are known to be very time-consuming while *ex situ* measurements can lead to the lost of vital

information that could be obtained in an *in situ* technique. The group of Bell[17] also investigated the composition of cobalt oxide catalyst as a function of potential and *in situ* Raman spectroscopy was used to characterize cobalt oxide species formed during linear sweep voltammetry. However, although the problems associated with *ex situ* studies were resolved in this case, it still involved scanning the potential sequentially resulting in a low-throughput analysis. In this work, we describe a simple technique that combines the advantages of both combinatorial studies and *in situ* characterization. That is, the technique is fast and the measurements obtained are truly characteristic of the system. In order to accomplish this work, we rely on the theory of bipolar electrochemistry[18-20] in combination with *in situ* Raman microscopy.

The operating principle of bipolar electrochemistry is illustrated in figure 1.3.1. When a potential difference, E_{appl}, is applied across an electrolytic solution containing a conducting substrate that has no direct contact with the external power supply, the substrate may become a bipolar electrode. That is, one that acts simultaneously as an anode and as a cathode. This occurs when the electric field generated in the solution exceeds a certain threshold value, thereby initiating faradaic reactions at the ends of the substrate. The reason for the bipolar behavior is that because of the solution's resistance to current, the applied potential drops across the solution leading to an interfacial potential difference between the substrate and the solution that varies along the length of the bipolar electrode. Because the interfacial potential varies laterally along the electrode surface, the rate of reactions varies according. This property of BPE has been used to create molecular and solid-state gradients[21-24]. The formation of chemical gradients using bipolar electrochemistry has been demonstrated by Shannon's group[24]. Specifically, a Au wire acting as the bipolar electrode was immersed in a solution containing Cd^{2+} and SO_4^{2-} ions.

Application of a voltage resulted in the deposition of Cd, CdS and S at different locations on the electrode. The surface was screened using Raman microscopy and Auger electron spectroscopy.

Oxides of cobalt such as $Co(OH)_2$, Co_3O_4, CoO(OH) and CoO_2 have been reported as catalyst for water oxidation[11-13,25]. Recently, Stahl and coworkers[16] carried out a systematic study of water oxidation catalyzed by cobalt oxide species at different pH and potentials in an effort to elucidate the mechanism of water oxidation by this catalyst under the various conditions. Their results were in good agreement with thermodynamic data for the formation of different cobalt species. In the work presented in this chapter, we used bipolar electrochemistry as a technique to rapidly screen the composition of the cobalt oxide catalysts by displaying the possible species simultaneously on a bipolar electrode and characterizing them using in situ Raman microscopy. Raman spectra recorded at various positions on the bipolar electrode revealed that the composition of the cobalt oxide is not uniform on the surface. Because the variation in composition as a function of position is a consequence of the potential gradient along the electrode, bipolar electrochemistry can be used to build composition-potential relationships about the catalyst. By evaluating the activity of the various compositions using Scanning electrochemical microscopy (SECM), composition-activity relationships were obtained about the catalyst. This information was used to identify the active phase of the catalyst which will provide insight into the mechanism of water oxidation.

4.2 Materials and Methods

4.2.1 Materials

$NaNO_3$ (>99% ACS reagent, Aldrich Chemical) and KOH (87.1%, Fisher Scientific Company) were used as received. The driver electrodes for the bipolar electrochemical cell were

made from stainless steel foil (Alfa Aesar). Millipore-Q purified deionized water (18.2MΩ·cm) was used to prepare all solutions and rinse electrodes.

4.2.2 Substrate preparation

Cobalt foil electrodes were mechanically polished successively with 400 -, 600 -, 800 - and 1200 - grit SiC paper sonicated in distilled water for 5 min. They were then rinsed sequentially with distilled water, absolute ethanol and distilled water. A layer of cobalt oxide was formed on the cobalt electrode in a conventional (unipolar) electrochemical cell by 8 oxidation-reduction cycles from 0 to 0.60V (vs Ag/AgCl) in 0.5M $NaNO_3$ at 50mV/s. The cobalt oxide electrode was rinsed with distilled water and dried in a flowing stream of nitrogen and used as the working in the traditional three electrode cell and as the bipolar electrode in the bipolar electrochemical cell in subsequent experiments. In both cases, 0.1M KOH was used as the electrolyte.

4.2.4 Electrochemistry

All unipolar electrochemical measurements were performed using a standard three-electrode configuration in a home-built glass cell. In all cases we used a cobalt foil as the working electrode, a Platinum counter electrode and either a Ag/AgCl(sat) (Bioanalytical Systems, Inc.) or a Hg/HgO (3M) (Gamry Instruments) reference electrode. The electrochemical cell was controlled using an Epsilon electrochemical work station (Bioanalytical Systems, Inc.).

All bipolar electrochemical measurements were performed in a home-built single compartment cell (ca. 20mL total volume)using a Hewlett-Packard model 6010 regulated DC power supply to control the potential applied between two stainless steel driver electrodes

separated by 4.5cm. The bipolar cobalt electrode was placed symmetrically between the two driver electrodes. After immersing all three electrodes in the 0.1M KOH electrolyte, a potential of 15V was applied across the driver electrodes. The entire cell was mounted on the Raman microscope stage and this potential was maintained while the Rama spectra were collected.

4.2.5 Raman Microscopy

Raman scattering was excited using the 514nm output (ca. 34mW) from an air cooled argon ion laser (model 163-C42, Spectra-Physics lasers, Inc.). The spectra were collected and analyzed using a Renishaw InVia Raman microscope and associated software. A leica 50x (0.75NA) objective was used to focus the excitation light onto the sample. The scattered radiation was collected by the same objective through a spectrometer with entrance slits of about 12-15μm. The exposure time for each spectrum was 30 seconds and only a single scan was made. A 1200 lines mm^{-1} grating was used for all measurements providing a resolution of $\pm 1cm^{-1}$. The instrument was calibrated for the Raman shift by referencing to that of silicon.

5.2.6 SECM Measurements

Scanning electrochemical microscopy (SECM) (CH-900, CH Instruments Inc., Austin, TX) was used to evaluate the oxygen evolution activity of the various phases of the cobalt oxide present on the surface of the bipolar electrode (BPE). The bipolar electrochemical cell containing the substrate, the driver electrodes, and 0.1M KOH electrolyte (degassed), was mounted on the SECM stage and a 10 μm platinum ultra-micro electrode (UME) was used as the working electrode. A platinum gauze counter electrode and a Hg/HgO reference electrode were also dipped in to the bipolar electrochemical cell containing the BPE and the driver electrodes. A voltage of 15V was applied across the BPE for 30seconds. To avoid the electric field in the

bipolar electrochemical from interfering with the SECM tip potential, the oxygen reduction measurements were carried out ex situ. Therefore right before the measurement the power supply was turned off. The potential of the UME was swept from 0 to -0.8V at a rate of 100mV/sec in order to reduce the oxygen evolved from the surface of the BPE. The UME was then moved 1mm from the anodic end towards the center and the solution was degassed with nitrogen before turning on the power supply once again to generate oxygen from the bipolar electrode. The potential of the UME was swept again from 0 to -0.8V and the current due to the oxygen reduction was recorded. This process was repeated until the microelectrode had been moved a total distance of 10mm to the center of the BPE.

4.3 Results and Discussion

4.3.1 Formation of a Gradient in Cobalt Oxide Species

A cobalt substrate unto which a layer cobalt oxide was formed in a solution of 0.5M $NaNO_3$ in a three-electrode electrochemical setup was used as the bipolar electrode. It was placed in a bipolar electrochemical cell containing 0.1M KOH. The cell was then mounted on the stage of the Raman microscope and a potential difference of 15V was applied across the driver electrodes. Figure 4.3.1.1 shows the *in situ* Raman spectra collected at different positions along the bipolar electrode starting from the anodic pole where the oxidizing potential is highest towards the center where the oxidizing potential is lowest. From the anodic pole towards the center of the bipolar electrode, the peak at 463cm^{-1} decreases in intensity while a peak at 691cm^{-1} becomes prominent. These changes clearly demonstrate the composition of the cobalt oxide species along the surface of the bipolar electrode is not uniform but varies with position. The changes observed

in the Raman spectra can be attributed to the gradient in the interfacial potential difference between the electrode and the solution.

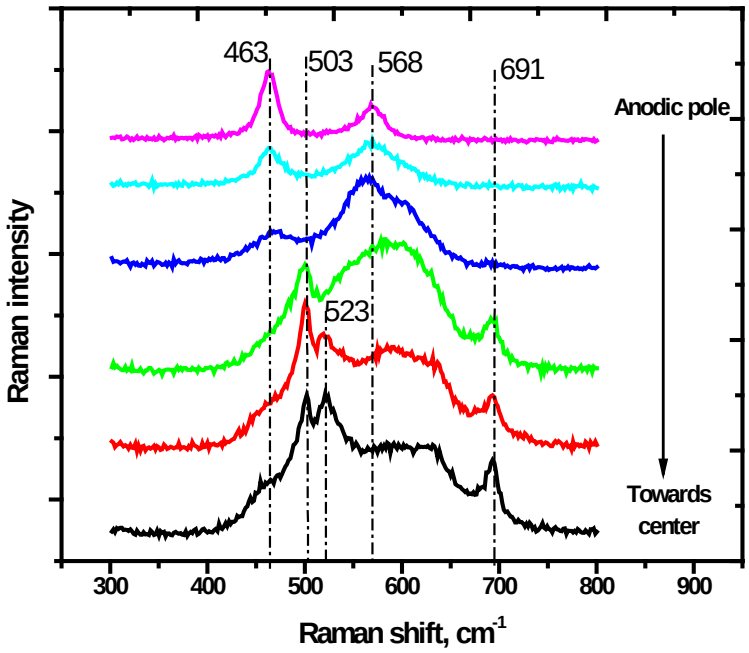

Figure 4.3.1.1 In situ Raman spectra collected at the anodic pole of the bipolar electrode as a function of position for E_{appl} = 16V.

In order to verify that the changes in the Raman spectra as a function of position were due to a distribution of the interfacial potential difference along the bipolar electrode, a traditional three-electrode electrochemical setup was used and the as-deposited cobalt oxide substrate served as the working electrode. Raman spectra were then recorded as a function of increasing applied potential. The spectra recorded for the as-prepared cobalt oxide at open circuit potential is shown in figure 4.3.1.2. In the left spectrum peaks can be observed at 485, 523, 620 and 691 cm^{-1}.

Based on previous work[27, 28], these features have been assigned respectively to the E_g, F_{2g}, F_{2g} and A_{1g} vibrational modes of Co_3O_4 which is black in color. Raman spectra recorded for bluish

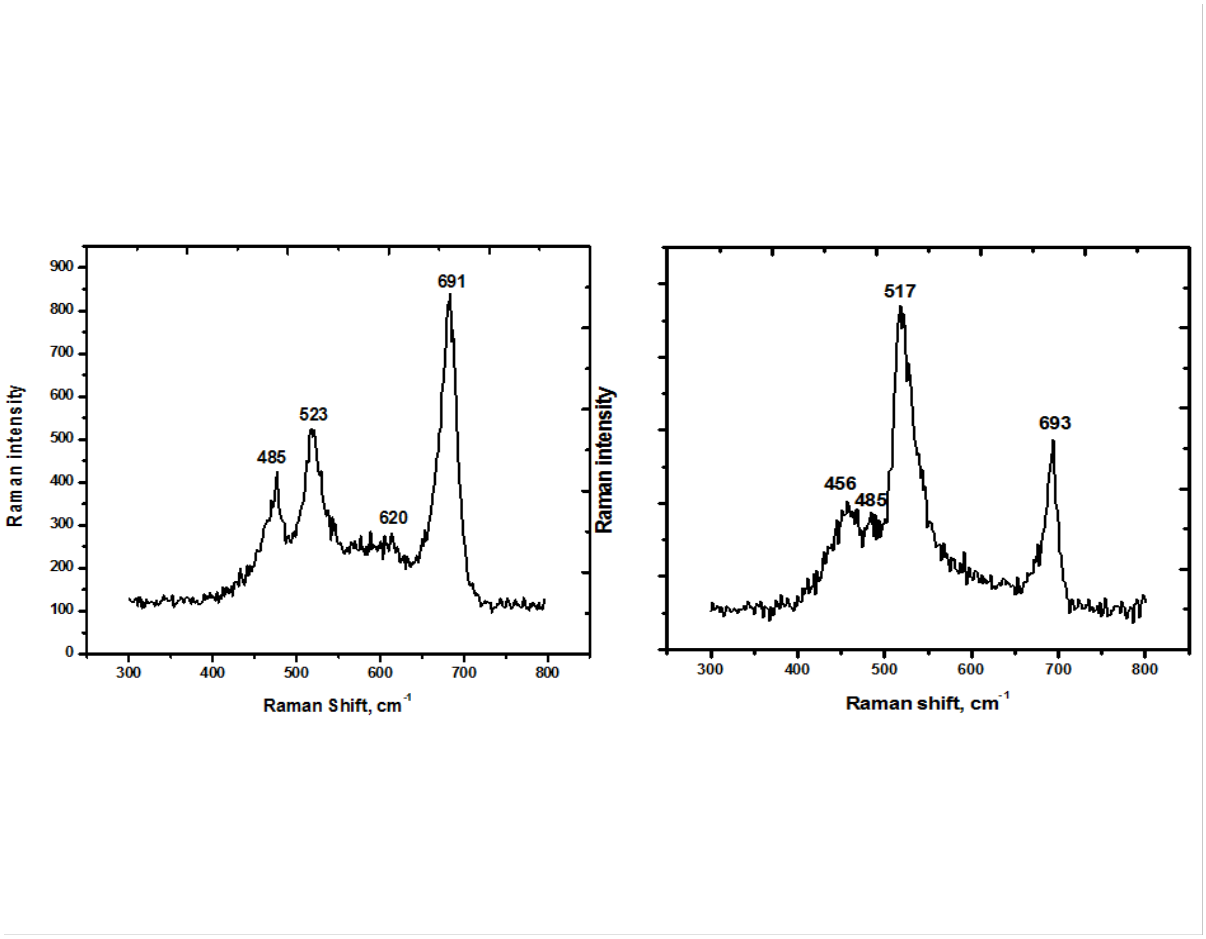

Figure 4.3.1.2 Raman spectra of various spots of as-prepared oxide at open circuit potential. The material was prepared by potential cycling between 0.0 and 0.8V in 0.5M $NaNO_3$. The electrode was Co metal substrate. Although the material consists predominantly of Co_3O_4 (left), which is black in color, the spectrum to the right recorded on bluish black spots indicates the presence of $Co(OH)_2$.

black spots revealed a mixture of Co_3O_4 and $Co(OH)_2$ (figure 4.3.1.2, left) when compared with the spectra of the pure phases reported in chapter 3. Pure $Co(OH)_2$ exhibits Raman bands at 454 and 519cm^{-1} and are assigned to the CoO A_g and OCoO E_g modes respectively[30].

Raman spectra of the as-prepared cobalt oxide recorded in 0.1M KOH at different applied potentials are shown in figure 4.3.1.3.

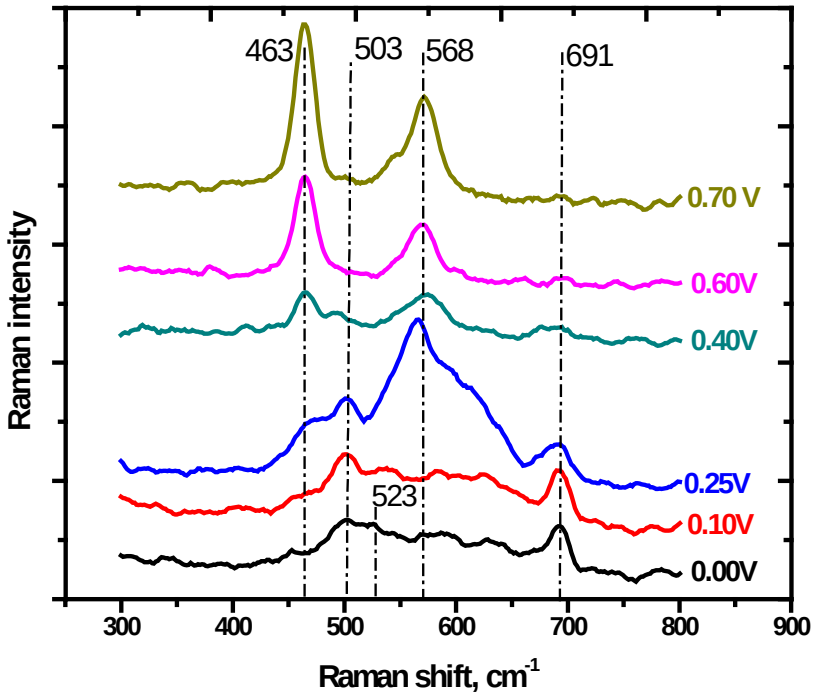

Figure 4.3.1.3 *In situ* Raman spectra of as-deposited cobalt oxide in 0.1 M KOH collected as a function of applied potential in a three-electrode electrochemical cell.

At 0.0V the Raman spectrum is dominated by a band at 692cm^{-1}. This is consistent with the presence of Co_3O_4 species. As the potential is raised to a value of 0.10V, a feature at 503cm^{-1}

becomes more apparent. This feature has previously been reported and is ascribed to the cobalt oxy-hydroxide species, CoO(OH) [29, 30]. The broad feature observed at 0.25V with its center at 563cm^{-1} is due to the amorphous nature of the CoO(OH) species at room temperature[29]. As the potential is further raised to about 0.40V the 503cm^{-1} peak belonging to CoO(OH) attenuates while new peak at emerges at 463cm^{-1}. In addition, the broad feature is replaced by a well defined peak centered at 564cm^{-1}.The attenuation of the peak at 503cm^{-1} belonging to CoO(OH) and the emergence of well-define peaks at 463cm^{-1} and 563cm^{-1} have not been reported before for cobalt oxide species. Bell and coworkers[17] observed only an increase in the intensity of the peak at 503cm-1 at higher applied potential but no new features at 463cm^{-1} and 563cm^{-1}. This led them to the conclusion that CoO(OH) is the active phase of the catalyst. Our observation clearly indicates the formation of new phase other than CoO(OH) at higher potentials. Based on Raman studies of $LiCoO_2$ species[31-33], we assign the peaks at 463cm^{-1} and 563cm^{-1} to the A_{1g} and E_g vibrational modes of CoO_2 which correspond to oxygen vibrations involving O-Co-O bending and Co-O stretching modes respectively. However, the A_{1g} and E_g vibrational modes observed in our work occur at much lower frequencies than those reported for $LiCoO_2$, therefore we rule out the possibility of $KCoO_2$ in our sample where cobalt exists in the 3+ oxidation state. This is consistent with *in situ* Raman studies of the electrochemical oxidation of $LiCoO_2$ to $Li_{1-x}CoO_2$ where it was shown that as the compound is gradually delithiated, the oxidation state of cobalt increases from 3+ to 4+ and the A_{1g} and E_g modes are shifted to lower frequencies[34]. We propose that the presence of CoO_2 in our sample is due to the presence of γ-CoO(OH) as opposed to β-CoO(OH). It has been reported that unlike β-CoO(OH), γ-CoO(OH) undergoes further oxidation to form a Co(IV) species[35]. γ-CoO(OH) is formed from α-$Co(OH)_2$ while β-CoO(OH) is formed from β-$Co(OH)_2$. Evidence of $Co(OH)_2$ is provided by the appearance of

bluish black species alongside the dominant black Co_3O_4 on the as-prepared cobalt oxide as mentioned earlier. The Raman spectrum of this bluish black species is consistent with that of $Co(OH)_2$ as indicated in figure 4.3.1.2. The presence of $Co(OH)_2$ is probable because the as-prepared cobalt oxide was prepared by oxidizing the cobalt metal in $NaNO_3$ from which hydroxide ions are generated upon reduction of the nitrate ions. Blue/green α-$Co(OH)_2$ is known to form at higher pH whereas pink β-$Co(OH)_2$ is formed under acidic conditions. Therefore, α-$Co(OH)_2$ and Co_3O_4 are both[39] oxidized to γ-CoO(OH) which is then oxidized to CoO_2. EPR and X-ray spectroscopic studies have confirmed the presence of Co^{4+} species under oxygen evolution conditions, which is consistent with our report of CoO_2. Moreover the structure of the Co^{4+} containing species was described as a stacked layer of cobalt-oxo/hydroxo clusters, whereby each layer is composed of octahedral edge-sharing cobaltate (CoO_6) motifs. This structure is in agreement with one derived from α-$Co(OH)_2$[16] instead of β-$Co(OH)_2$. Although the two polymorphs of cobalt hydroxide are known to crystallize into a hexagonal layered structure, β-$Co(OH)_2$ exhibits a brucite-like structure while α-$Co(OH)_2$ is characterized by a hydrotalcite-like structure as shown in Figure 4.3.1.4. In β-$Co(OH)_2$ the layers possess no net charge and are made of edge-sharing octahedra consisting of Co^{2+} cations coordinated with six OH^- anions. However in α-$Co(OH)_2$ the layers are positively charged and anions and water molecules reside in the interlayer spaces to balance the positive charge, resulting in a more expanded structure relative to β-$Co(OH)_2$. The structure of is α-$Co(OH)_2$ is consisted with the layered structure of CoO_2 (figure 4.3.1.5) formed by successive oxidation of cobalt hydroxide. The layered and

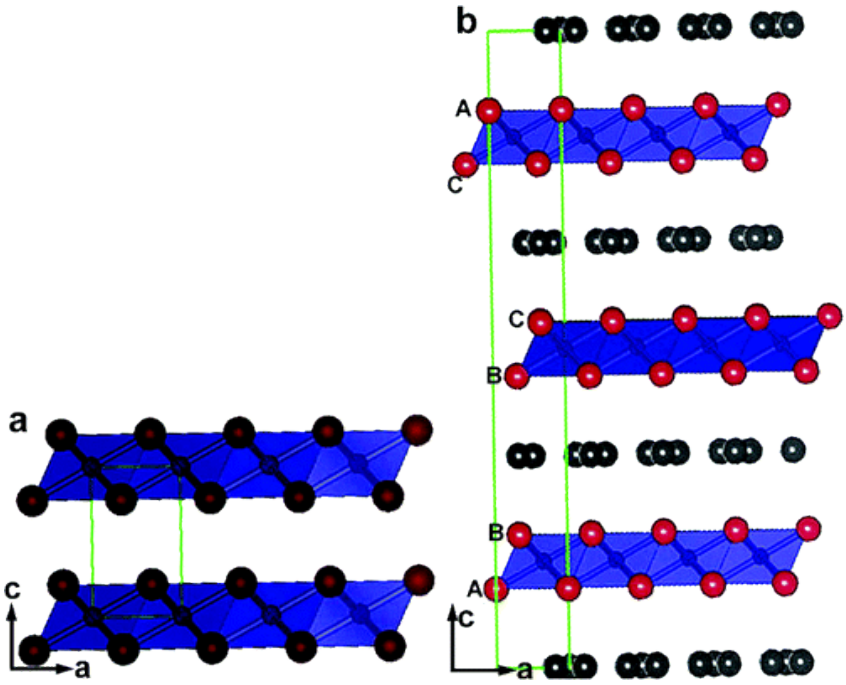

Figure 4.3.1.4 Structure models of (a) β-$Co(OH)_2$ and (b) hydrotalcite-like α-type cobalt hydroxide. Atoms for Co, OH, and guests (interlayer anion, H_2O) are represented by blue, red, gray balls, respectively. In both models, unit cells are indicated by the green rectangles. Labels A, B, and C in model b show the stacking sequence of the hydroxyl. [Reprinted with permission from Ma, R.; Liu, K.; Takada, K.; Fukuda, K.; Ebina, Y.; Bando, Y.; Sasaki, K. *Inorg. Chem.* **2005,** 45, 3964-3969. Copyright © 2006, American Chemical Society]

open structure allows the catalyst to accommodate redox changes without significant changes in the lattice parameters or structural rearrangements.

Beyond 0.40V no new feature were observed in the Raman spectra in figure 4.3.1.3. Increasing the potential to 0.60V only resulted in an increase in the 463cm^{-1} and 568cm^{-1} peak intensities. This indicates a constant composition in the cobalt oxide species at these potentials.

Increasing the potential above 0.70V was accompanied by the production of oxygen bubble and the spectrum recorded at this potential resembled that obtained at 0.6V. This suggests that CoO_2 is the species present during water oxidation. Therefore, it must be the active phase of the catalyst.

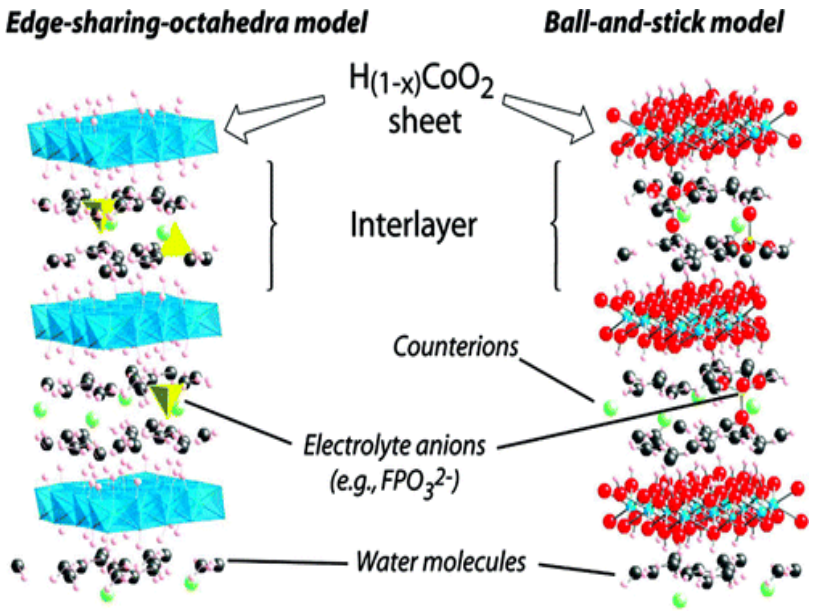

Figure 4.3.1.5 Depiction of cobalt-oxide layered structures that can undergo pH-dependent redox changes without large lattice variations. During catalytic water oxidation, counterion movements and proton transfers can rapidly compensate for changes in layer charge arising from changes in the cobalt oxidation states.[Reprinted with permission from Gerken, J. B. M., J. G.; Chen, J. Y.C; Rigsby, M. L.; Casey, W. H.; Britt, R. D.; Stahl, S. S. *J. Am.Chem. Soc.* **2011**, *133*, 14431-14442. Copyright © 2011, American Chemical Society]

The changes in the Raman spectra of as-prepared cobalt oxide were further characterized by recording a cyclic voltammogram in a three-electrode setup in 0.1M KOH and the results are shown in figure 4.3.1.6. The voltammogram reveals three quasi-reversible redox features which

is consistent with the formation of various cobalt oxide phases. Base on previous work[28, 36-38] we attribute these features to the following redox reactions.

Peaks I/ VII

$$3Co(OH)_2 + 2OH^- \rightleftharpoons Co_3O_4 + 4H_2O + e^- \qquad E_a = 0.05V \qquad 4.3.1.1$$

Peaks II/VI

$$Co(OH)_2 + OH^- \rightleftharpoons CoO(OH) + H_2O + e^- \qquad E_a = 0.30V \qquad 4.3.1.2$$

$$Co_3O_4 + OH^- + H_2O \rightleftharpoons 3CoO(OH) + e^- \qquad E_a = 0.30V \qquad 4.3.1.3$$

Peaks III/V

$$CoO(OH) + OH^- \rightleftharpoons CoO_2 + H_2O + e^- \qquad E_a = 0.55V \qquad 4.3.1.4$$

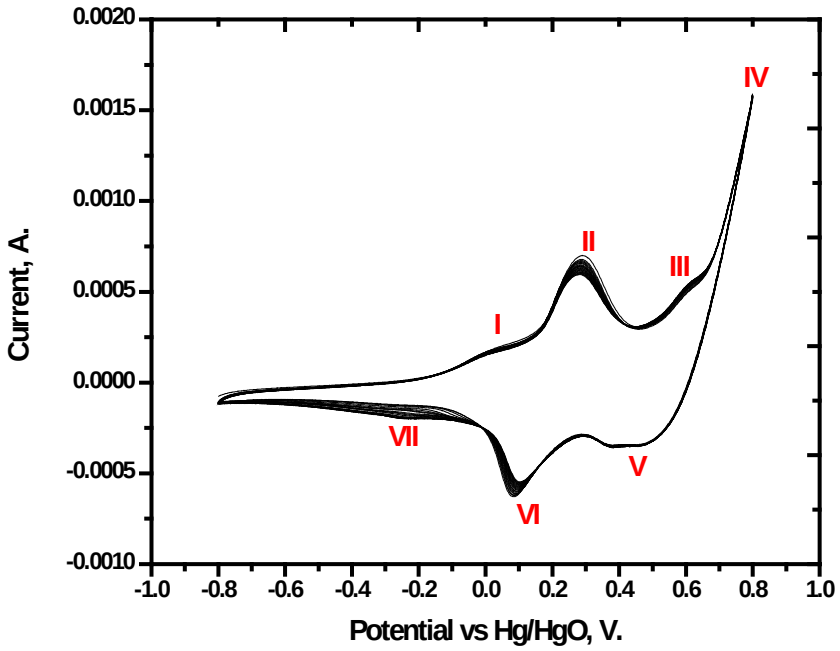

Figure 4.3.1.6 Cyclic voltammogram (20cycles) of as-deposited cobalt oxide in 0.1M KOH. Scan rate = 50mV/sec.

Following the formation of CoO_2 in this cyclic voltammogram is the onset of a strong oxidation peak (IV) beginning at 0.7V which is attributed to the catalytic oxygen evolution reaction (OER) as follows:

$$4OH^- \rightarrow O_2 + 2H_2O + 4e^- \qquad E = 0.70V \qquad 4.3.1.5$$

Considering the oxidation peaks in the cyclic voltammogram and the species assigned to them, it is obvious that the changes observed in the Raman spectra as a function of potential strongly correlates the features observed in the cyclic voltammogram. The three peaks in the anodic scan correspond to the formation of the three phases observed in the *in situ* Raman spectra in figure 4.3.1.3. That is, the changes in Raman spectra correspond to the transformation due to the $Co(OH)_2/Co_3O_4 \rightarrow CoO(OH) \rightarrow CoO_2$. Most importantly, when the Raman response obtained in the three-electrode setup is compared to that of the bipolar electrode, it becomes evident that changes in the Raman response along the bipolar electrode are due to the presence of various cobalt oxide species which is attributed to the variation of interfacial potential difference along its length. The Raman spectrum recorded at the anodic extremity of the bipolar electrode matches that obtained higher potentials in the three-electrode setup which was assigned to CoO_2. On the other hand, the spectrum recorded towards the center of the bipolar electrode matches that recorded at lower potentials in the three-electrode setup which was assigned to Co_3O_4. Therefore, the interfacial potential difference between the bipolar electrode and the solution can be correlated to the applied potential in the three-electrode setup.

4.3.2 SECM Results

After using *in situ* Raman spectroscopy and cyclic voltammetry to reveal the identity of of the cobalt oxide species present on the bipolar electrode, Scanning electrochemical microscopy was used to assess their catalytic activity of each species for water oxidation and the results are shown in figure 4.3.2.1. This figure shows the tip current due to reduction of the oxygen generated from the bipolar electrode at various positions. Figure 4.3.2.1a shows the in situ Raman spectra collected at the positions on the bipolar indicated in the column to the left of figure 4.3.2.1a. The potentials corresponding to the positions were calculated using equation using equation 1.5.2 and are also shown in the column to the left of Figure 4.3.2.a. Looking at Figure 5b, we see a constant background current from the center ($x = 10mm$) of the BPE towards the anodic pole ($x = 7mm$). According to the in situ Raman spectra, this region is dominated by the species Co_3O_4 and CoO(OH). The potential range calculated from equation 2 is 0 to 0.39V. This is consistent with the cyclic voltammogram in Figure 4.3.2.6 which contains two anodic waves in the potential range of -0.1 to 0.4V. From $x = 7mm$ to $x = 5mm$, even though

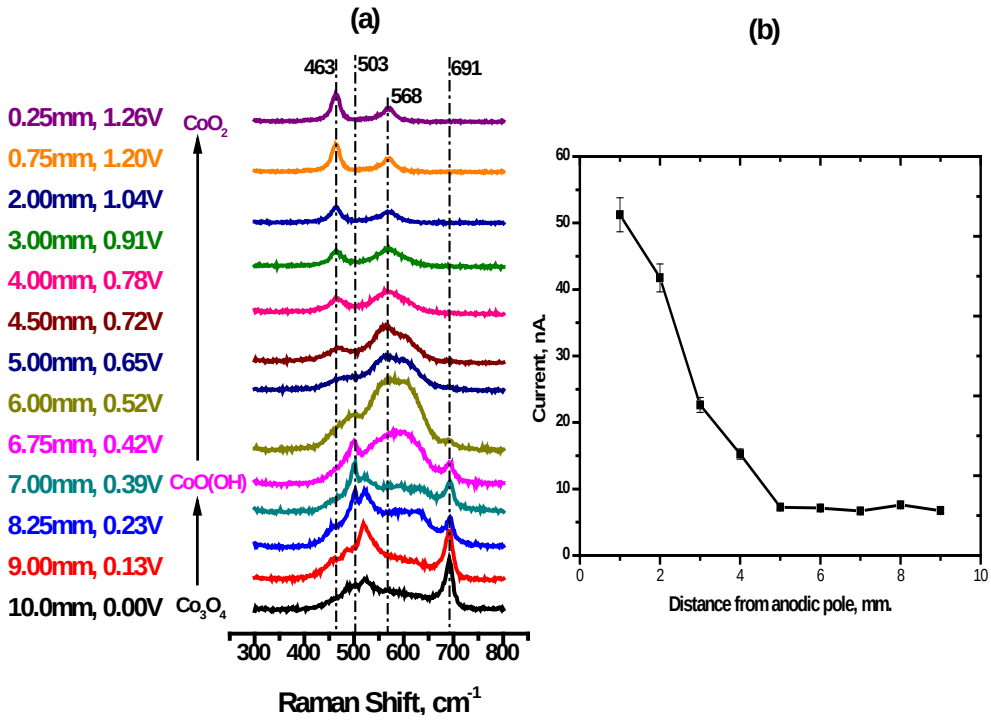

Figure 4.3.2.1 Column to the left: Calculated potentials as a function of position at the anodic pole of the bipolar electrode. **a)** In situ Raman spectra recorded at positions shown in the left column. **b)** Tip current due to oxygen reduction at the anodic pole as a function of position.

the *in situ* Raman spectra indicates the formation of some CoO_2, the current is still at the background level indicating the absence oxygen evolution from the BPE at these positions. The calculated potential range over this distance is 0.39 to 0.65V. The cyclic voltammogram contains an oxidation wave in this potential range corresponding to the formation of CoO_2. However, the SECM probe current starts to rise above background levels at distances less than $x = 5mm$ and continues to rise approximately linearly towards the anodic extremity. Notice that the spectral changes in the Raman spectrum of CoO_2 that accompany this increase in current, and therefore

the activity of CoO_2. The $463cm^{-1}$ peak becomes more intense relative to the $568cm^{-1}$ with increased interfacial overpotential on the bipolar electrode. The intensity ratio of these two peaks increases linearly with increased overpotentental, accompanied by the SECM probe current as shown in figure 4.3.2.2. These changes in the Raman intensity peak ratio are consistent with

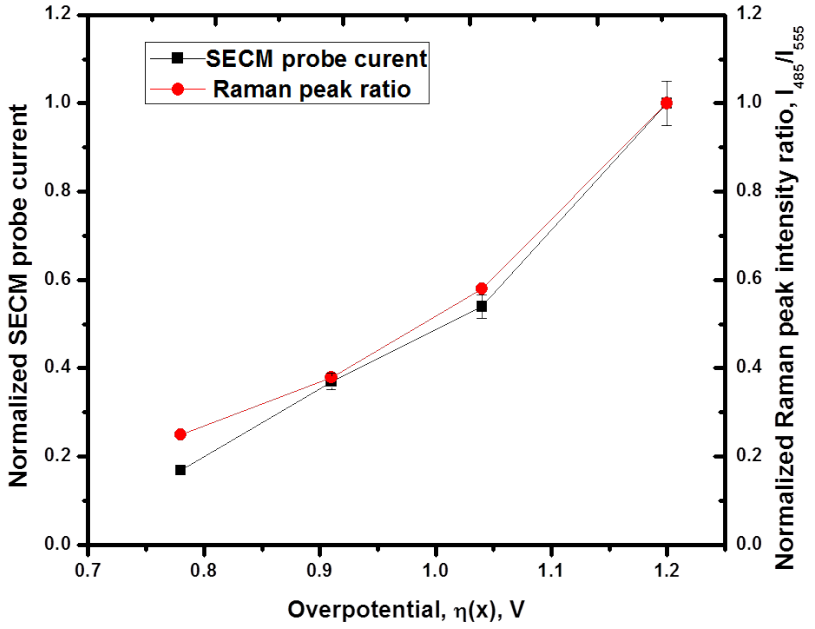

Figure 4.3.2.2. Variation of SECM probe current (black squares) and Raman intensity ratio, $I_{463}/I_{568,}$ (red circles) for the CoO_2 species as a function of overpotential η(x).

structural transformations in the CoO_2 species that in turn favor increased catalytic activity at higher overpotentials. The possibility that the increased activity at higher overpotentials is due to an increased amount of CoO_2 formed can be ruled out because the sum of the intensities of the $463cm^{-1}$ and $568cm^{-1}$ peaks remains constant with increased overpotential.

The fact that a tip current is observed only after the formation of CoO_2 is consistent with reports that the mechanism of water oxidation requires high oxidation state intermediates. EPR studies[15, 16] on cobalt oxide anodes for water oxidation have provided clear evidence if Co^{4+} ions during under conditions of oxygen evolution. In addition, we believe that at higher potentials, CoO_2 undergoes a structural transformation that results in an increased catatalytic activity. This transformation can be attributed to the remodeling of spinel-type structures in Co_3O_4 materials to layered structures which have been identified during high catalytic turnovers by Nocera and coworkers[16].

4.4 Conclusion

In this study the theory of bipolar electrochemistry was exploited as a simple and fast method to display various phases of a cobalt oxide catalyst for water oxidation. This allowed a rapid identification of the species, namely Co_3O_4, CoO(OH) and CoO_2 *in situ* Raman microscopy. These results are in good agreement with data obtained from cyclic voltammetry. Finally the catalytic activity of the phases present on the bipolar electrode was screened using Scanning electrochemical microscopy. CoO_2 was found to be the active phase as opposed to CoO(OH) reported in the literature. This is consistent with the requirement of Co^{4+} intermediates for water oxidation. Evidence of further structural transformation within the CoO_2 material leading to increased catalytic activity was provided by changes in its Raman spectrum at higher potentials.

References

1) Lewis, N. S.; Nocera D. G. *Proc. Natl. Acad. Sci. U. S. A.* **2006,** 103, 15729-15735.

2) Cook, T. R.; Dogutan, D. K.; Reece, S. Y.; Surendranath, Y.; Teets, T. S.; Nocera, D. G. Chem. Rev. 2010, 110, 6474-6502.

3) Nelson, N.; Ben-Shem, A. *Nat. Rev. Mol. Cell. Biol.* **2004,** 5, 971-982.

4) Dau, H.; Limberg, C.; Reier, T.; Risch, M.; Roggan, S.; Strasser, P. *ChemCatChem* **2010,** 2, 724-761.

5) Najafpour, M. M.; Moghaddam, A. N.; Allakhverdiev, S. I.; Govindjee *Biochimica et Biophysica Acta* **2012,** *1827* , 1110-1121.

6) Bard, A. J.; Faulkner, L. R. *Electrochemical methods: Fundamentals and Applications,* John Wiley & Sons, Inc., New York, 1990.

7) Trasatti, M. R. *Electrochim. Acta* **1984,** 29, 1503-1512.

8) Tarasevich, M. R.; Efremov, B. N. *Electrodes of Conductive Metal Oxides* (Ed.: Trasatti, S.) Elsevier, Amsterdam, 1980, chapt. 5

9) Tilley, S. D.; Cornuz, M.; Sivula, K.; Gratzel, M. *Angew. Chem*. **2010,** 122, 6549-6552.

10) Yongblood, W.J.; Lee, S. H. A.;Kobayashi, Y.; Hernandez-Pagan, E. A,; Hoertz, Moore T. A.;Moore, A. L.; Gust, D.; Mallouk, T. E. *J. Am. Chem. Soc*. **2009,** 131, 926-927.

11) Soto, A. B.; Arce, E. M.; Palomar-Pardave, M.; Gonzalez, I. *Electrochim. Acta* **1996,** 41, 2647-2655.

12) Cui, C. Q.; Jiang, S. P.; Tseung, A. C. C. *J. Electrochem. Soc.* **1992,** 139, 1535-1544.

13) Schmidt, T.; Wendt, H. *Electrochim. Acta* **1994,** 39, 1763-1767.

14) Kanan, M. W.; Nocera, D. *Science* **2008,** *321,* 1072-1075.

15) McAlpin, J. G.; Surrendranath, Y.; Dinca, M.; Stich, M.; Stoian, S.; Casey, H. W.; Nocera, D.; Britt, R. D. *J. Am. Chem. Soc.* **2010,** *132*, 6882-6883.

16) Gerken, J. B. M., J. G.; Chen, J. Y.C; Rigsby, M. L.; Casey, W. H.; Britt, R. D.; Stahl, S. S. *J. Am.Chem. Soc.* **2011**, *133*, 14431-14442.

17) Yeo, B. S.; Bell, A. T. *J. Am. Chem. Soc.* **2011,** 133, 5587-5593

18) Fleischmann, M.; Ghoroghchian, J.; Rolison, D.; Pons, S. *J. Phys. Chem.* **1986,** 90, 6392-6400.

19) Duval, J.; Kleijn, J. M.; van Leeuwen H. P. *J. Electroanal. Chem.* **2001,** 505, 1-11.

20) Duval, J.; Cecilia, J.; van Leeuwen H. P. *J. Phys. Chem.* **2003,** 107, 6782-6800.

21) Ulrich, C.; Anderson, O.; Nyholm, L.; Bjorefors, F. *Angew. Chem. Int. Ed.* **2008,** 47, 3034-3036.

22) Inagi, S.; Ishiguro, Y.; Atobe, M.; Fuchigami. *Angew. Chem. Int. Ed.* **2010,** 49, 10136-10139.

23) Shida, N.; Ishiguro, Y.; Fuchigami, T,; Inagi, S. *ACS Macro Lett.* **2012,** 1, 656-659.

24) Ramakrishnan, S.; Shannon, C. *Langmuir* **2010,** 26, 4602-4606.

25) Esswein, A. J.; McMurdo, M. J.; Rpss, P. N.; Bell, A. T.; Tilley, T. D. *J. Phys. Chem. C* **2009,** 113, 15068-15072.

26) Duval, J.; Kleijn, J. M.; van Leeuwen H. P. *J. Electroanal. Chem.* **2001,** 505, 1-11.

27) Khadzhiev, V.; Illiev, M.; Vergilov, I. *J. Phys. C: Solid State Physics.* **1988,** 21, L199.

28) Keng, P. Y.; Kim, B. Y.; Shim. I.; Sahoo, R.; Veneman, P. E.; Armstrong, H. Y.; Permberton, J. E.; Bull, M. M.; Griebel, J. J.; Ratcliff, E.; Nebesny, K. G.; Pyun, J. *ACS nano*. **2009,** 3, 3143-3157.

29) Pauporte, T.; Mendoza, L.; Cassir, M.; Bernard, M. C.; Chivot, J. *J. Electrochem. Soc.* **2005,** 152, C49-C53.

30) Yang, J.; Liu, H. W.; Martens, W. N.; Frost, R. L. *J. Phys. Chem. C.* **2010,** 114, 111-119.

31) Reimers, J. N.; Dahn, J. J. *Electrochem. Soc.* **1992,** 139, 2091-2097.

32) Markevich, G.; Salitra, G.; Aurbach, D. *Electrochem. Commun.* **2005,** 7, 1298-1304.

33) Park, Y.; Kim, N. H.; Kim, J. Y.; Eom, I-Y.; Jeong, Y. U.; Kim, M. S.; Lee, M. L.; Choi, H. C.; Jung, Y. M. *Vibrational Spectroscopy* **2010,** 53, 60-63.

34) Inaba, M.; Iriyama, Y.; Ogumi, Z.; Todzuka, Y.; Tasaka, A. *J. Raman Spectrosc.* **1997,** 28, 613-617.

35) Barde, F.; Palacin, M. R.; Beaudoin, B.; Delahaye-Vidal, A.; Tarascon, J. M. *Chem. Mater,* **2004,** 16, 299-306.

36) Casella, I. G. *J. Electroanal. Chem.* **2002,** 520, 119-129.

37) Casella, I. G.; Gatta, M. *Electroanal. Chem.* **2002,** 534, 31-38.

38) Spataru, N.; Terashima, C.; Tokuhiro, K.; Sutanto, I.; Tryk, D. A.; Park, S-M.; Fujishima, I. *J. Electrochem. Soc.* **2003,** E337-E341

39) Totir, D.; Mo, Y.; Kim, S.; Antonio, M. R.; Scherson, D. A. *J. Electrochem. Soc.* **2000,** 147, 4594-4597.

Chapter 5

Screening the Oxygen-Evolution Activity of Nickel Oxide Species Generated on a Bipolar Electrode Using in Situ Raman Microscopy and Scanning Electrochemical Microscopy

5.1 Introduction

Efficient electrochemical splitting of water to provide a sustainable supply of hydrogen fuel is being prevented by the lack of suitable catalysts that will lower the substantial overpotential associated with the oxygen evolution reaction (OER) [1]. Although ruthenium and iridium oxides exhibit the lowest overpotentials at practical current densities, they constitute rare-earth metals and are hence, expensive. Therefore, catalysts derived from earth-abundant, first row transition metals, such as cobalt and nickel have been developed and are currently being used in commercial alkaline electrolyzers [2-4]. Although nickel and cobalt exhibit inferior catalytic activity for the OER, they are more resistant to corrosion under alkaline conditions. Despite the impressive progress that has been made in this regard, the mechanism by which these catalysts operate is still a subject of controversy. Moreover the use of nickel oxyhydroxide as the positive electrode material in Ni-Cd alkaline batteries has prompted investigation into structural changes in the material in alkaline electrolytes during the charging/discharging cycle. The disparity in the structure/composition of these catalysts is in part, due to the fact that their activities are known to differ considerably depending on the method of electrode preparation. Nevertheless, the study the OER at oxidized electrode surfaces of adjacent first row transition metal should

provide useful information as to whether or not a common reaction mechanism prevails. It is generally accepted that oxygen evolution precedes at metal anodes following an oxidation-induced precipitation the metal oxide in which the metal ion exhibits a high valency. The metal oxide can be formed directly from the bulk metal or deposited on a substrate from the metal ions dissolved in solution. Preliminary work in developing structure/composition-activity relationships has revealed that structure and valency of the metal oxide differ considerably between the active and resting states of the metal oxide. Identifying the exact nature of the active form is therefore critical in elucidating the mechanism by which these catalysts operate. Knowledge of the water oxidation mechanism will be useful in optimizing the performance of the catalyst while structural insights will help build structure-activity relationships that can provide useful information in the design of new catalysts.

In the chapter 4, cyclic voltammetry and in situ Raman spectroscopic studies of cobalt electrocatalyst provided insight into the identity of the cobalt oxide species of the catalyst at different potentials. More importantly, bipolar electrochemistry was used to simultaneously display the various species for a rapid screening of the active phase using scanning electrochemical microscopy (SECM). It was found that the CoO_2 is responsible for catalytic oxidation of water by cobalt. This finding is consistent with electron paramagnetic (EPR) studies that revealed the presence of Co^{4+} species under oxygen evolution conditions[5, 6]. In this chapter, similar studies are carried out in order to gain insight into the identity of nickel oxide species present during water oxidation. The principles of bipolar electrochemistry have been outlined in details in chapter 1. Basically, a bipolar electrode is an electrode which has no physical contact with the external power supply and oxidation and reduction reactions can occur simultaneously at opposite ends. According to figure 1.6.1, because of the solution's resistance, the applied

potential drops across the solution resulting in an interfacial potential difference between the bipolar electrode and the electrolyte that varies laterally along the length of the electrode. The electrochemical driving force therefore varies accordingly, with the extent of oxidation and reduction reactions being highest at the anodic and cathodic extremities, respectively and decreases to a minimum at the center of the bipolar electrode. Because the composition and structure of redox-active species are strongly dependent on applied potential, bipolar electrochemistry has emerged as an attractive technique for simultaneous display of various forms of electrocatalyst for rapid screening of their activities.

5.2 Materials and Methods

5.2.1 Materials

$NaNO_3$ (>99% ACS reagent, Aldrich Chemical) and NaOH (87.1%, Fisher Scientific Company) were used as received. The driver electrodes for the bipolar electrochemical cell were made from stainless steel foil (Alfa Aesar). Millipore-Q purified deionized water (18.2MΩ·cm) was used to prepare all solutions and rinse electrodes.

5.2.2 Substrate preparation

Bulk nickel substrates were mechanically polished successively with 400 -, 600 -, 800 - and 1200 - grit SiC paper sonicated in distilled water for 5 min. They were then rinsed sequentially with distilled water, absolute ethanol and distilled water. The surface of the polished metal was oxidized electrochemically in 10M $NaNO_3$ by carrying out oxidation-reduction cycles between 0.00 and 0.70V at 0.1V/s for 3hrs. The oxidized nickel substrate was then rinsed with distilled water and dried in a flowing stream of Nitrogen before being transferred into 1M NaOH for further characterization in both the bipolar and traditional electrochemical cells.

5.2.3 Electrochemistry

All unipolar electrochemical measurements were performed using a standard three-electrode configuration in a home-built glass cell. In all cases we used a cobalt foil as the working electrode, a Platinum counter electrode and either a Ag/AgCl(sat) (Bioanalytical Systems, Inc.) or a Hg/HgO (3M) (Gamry Instruments) reference electrode. The electrochemical cell was controlled using an Epsilon electrochemical work station (Bioanalytical Systems, Inc.).

All bipolar electrochemical measurements were performed in a home-built single compartment cell (ca. 20mL total volume)using a Hewlett-Packard model 6010 regulated DC power supply to control the potential applied between two stainless steel driver electrodes separated by 4.5cm. The bipolar nickel hydroxide electrode was placed symmetrically between the two driver electrodes. After immersing all three electrodes in the 1M NaOH electrolyte, a potential of 10V was applied across the driver electrodes. The entire cell was mounted on the Raman microscope stage and this potential was maintained while the Raman spectra were collected.

5.2.4 Raman Microscopy

Raman scattering was excited using the 514nm output (ca. 34mW) from an air cooled argon ion laser (model 163-C42, Spectra-Physics lasers, Inc.). The spectra were collected and analyzed using a Renishaw InVia Raman microscope and associated software. A leica 50x (0.75NA) objective was used to focus the excitation light onto the sample. The scattered radiation was collected by the same objective through a spectrometer with entrance slits of about 12-15μm. The exposure time for each spectrum was 30 seconds and only a single scan was made. A 1200

lines mm^{-1} grating was used for all measurements providing a resolution of $\pm$ 1cm^{-1}. The instrument was calibrated for the Raman shift by referencing to that of silicon.

5.2.5 SECM Measurements

Scanning electrochemical microscopy (SECM) (CH-900, CH Instruments Inc., Austin, TX) was used to evaluate the oxygen evolution activity of the various phases of the cobalt oxide present on the surface of the bipolar electrode (BPE). The bipolar electrochemical cell containing the substrate, the driver electrodes, and 1M NaOH electrolyte (degassed), was mounted on the SECM stage and a 10μm platinum ultra-micro electrode (UME) was used as the working electrode. A platinum gauze counter electrode and an Hg/HgO reference electrode were also dipped in to the bipolar electrochemical cell containing the BPE and the driver electrodes. A voltage of 14V was applied across the BPE for about 10seconds. To avoid the electric field in the bipolar electrochemical from interfering with the SECM tip potential, the oxygen reduction measurements were carried out ex situ. Therefore right before the measurement the power supply was turned off. The potential of the UME was swept from 0 to -0.8V at a rate of 100mV/sec in order to reduce the oxygen evolved from the surface of the BPE. The UME was then moved 0.5mm from the anodic end towards the center and the solution was degassed with nitrogen before turning on the power supply once again to generate oxygen from the bipolar electrode. The potential of the UME was swept again from 0 to -0.8V and the current due to the oxygen reduction was recorded. This process was repeated until the microelectrode had been moved a total distance of 10mm to the center of the BPE.

5.3 Results and Discussion

5.3.1 Theory

A bipolar electrode is a conducting substrate on which anodic and cathodic faradaic reactions can be initiated simultaneously on opposite ends. This happens when a sufficient voltage (E_{appl}) is applied across an electrolytic solution containing the substrate using an externally power supply. Because of the solution resistance the applied potential difference drops approximately linearly across the solution resulting in the potential of the solution being higher than that of the substrate on one end (cathodic pole) and lower than that of the solution on the other end (anodic pole). There exists a single point (x_0) on the bipolar electrode between the cathodic and anodic pole where its potential equal that of the solution. Therefore, the interfacial potential difference between the electrode and the solution, which is the driving force for redox reactions, will vary along the length of the electrode with the highest cathodic and anodic potential differences appearing at the extremities. Because of the potential dependence of the composition of electroactive species, we take advantage of the potential distribution that exist on the surface a bipolar electrode to investigate the various forms of nickel oxide in an effort to identify its active phase as a water oxidation catalyst. According to figure 1.2.1b, we expect Ni to be in its highest oxidation state in the compound formed near the edge.

5.3.2 Formation of a Gradient in Nickel Oxide Species

The as-prepared nickel oxide substrate was used as the bipolar electrode to investigate the potential-dependence of the composition of nickel oxide species. The substrate was placed between two stainless steel driving electrodes dipped in 1M NaOH solution and the reaction cell was mounted of the stage of a Raman microscope. A potential difference of 8V was applied

between the driving electrodes to initiate faradaic reactions on the bipolar electrode. Following the application of the potential difference across the solution, Raman spectra were recorded at various positions at the anodic pole of the bipolar electrode. The results are shown in figure 5.3.2.1. Further from the anodic extremity, the Raman spectra are devoid of any peaks probably due to the low Raman cross section of the species present at these locations on the bipolar electrode. Raman spectra recorded at positions closer to the edge are dominated by two bands at 486 cm^{-1} and 562 cm^{-1} which are assigned to the E_g Ni-O stretching and the $A1_g$ Ni-O bending modes respectively. These changes in Raman spectra are ascribable to the variation in the interfacial potential difference between the Ni bipolar electrode and the NaOH solution. As the anodic extremity is approached, both bands continue to grow in intensity without the appearance of any new peaks. The absence of new peaks indicates a constant composition as a function of position while the increased intensity of the bands 486 cm^{-1} and 562 cm^{-1} indicates an increased amount in the species giving rise to these peaks. To investigate the dependence of the Raman response on the position along the bipolar electrode the as-prepared nickel oxide substrate was used as the working electrode in the traditional three-electrode setup and in situ Raman spectra were recorded as a function of applied potential. The result of this experiment is shown in figure

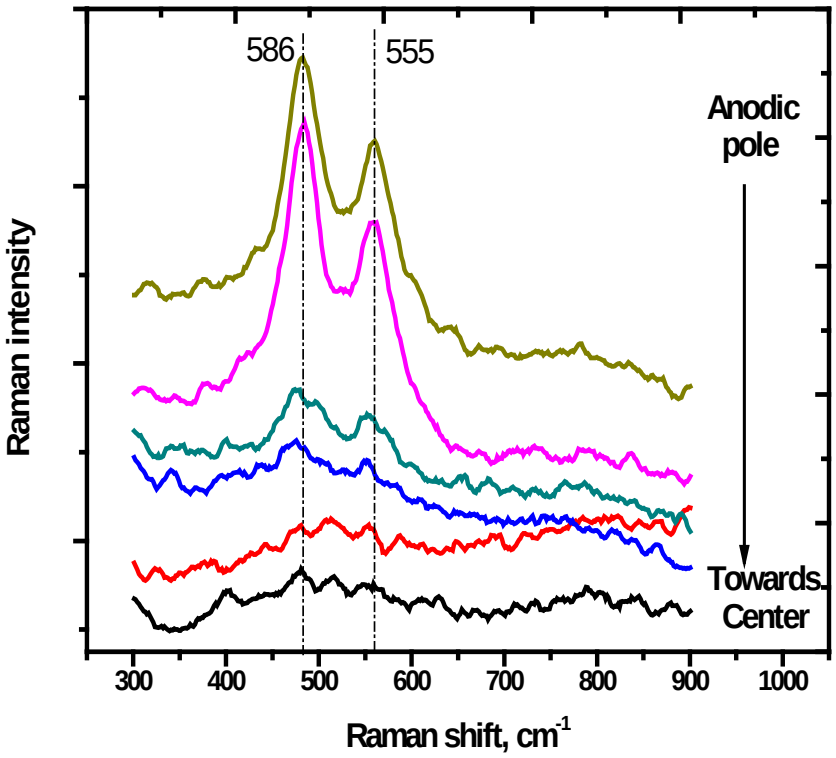

Figure 5.3.2.1 In situ Raman spectra collected at the anodic pole of the Ni bipolar electrode as a function of position for $E_{appl} = 8V$.

5.3.2.2. It has been reported that when a Ni electrode is immersed in an aqueous alkaline solution, its surface becomes covered by a layer of α-$Ni(OH)_2$ even at open circuit potential[7, 8]. The same species is formed to be formed when metallic nickel is electrochemically oxidized in the presence of $NaNO_3$.The absence of Raman bands in the potential range 0.00V to 0.40V where a signal from the α-$Ni(OH)_2$ is expected has been attributed to the low Raman cross-section of this compound[2]. As the potential is increased to 0.50V, the two bands at 486 cm^{-1} and 562 cm^{-1} observed previously in the bipolar

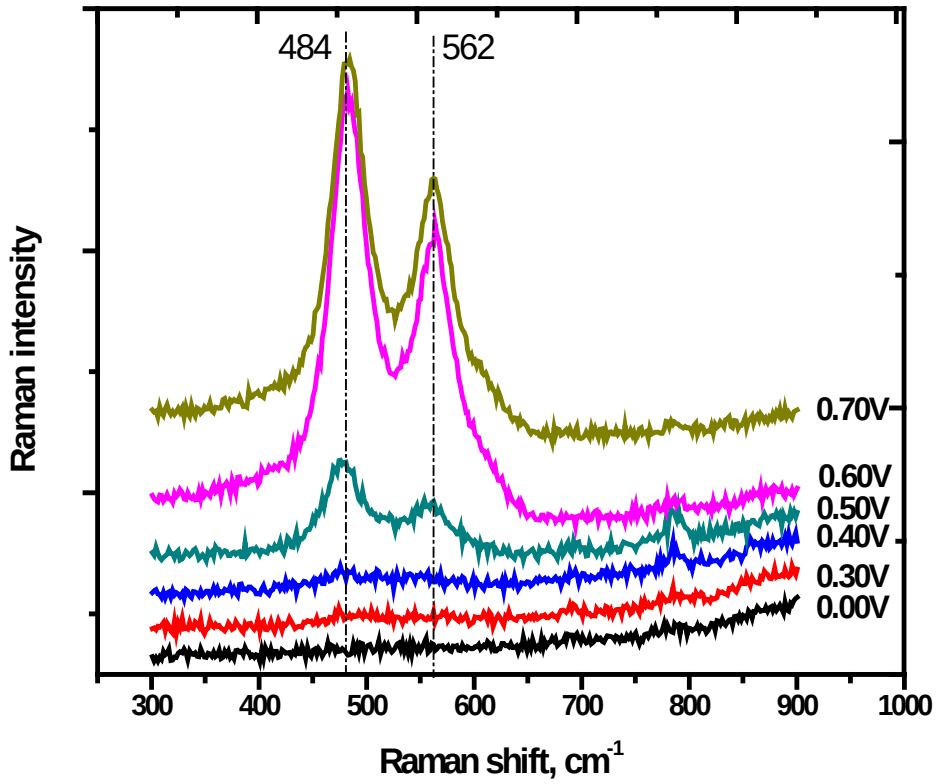

Figure 5.3.2.2 In situ Raman spectra of Ni working electrode in 1M NaOH collected as a function of applied potential in a three-electrode electrochemical cell.

setup become apparent. It is generally accepted that the two Raman bands observed at higher potentials are due to the oxidation of α-$Ni(OH)_2$ to γ-NiO(OH)[10-12]. However, Raman studies have revealed that the oxidation of $Ni(OH)_2$ species is usually accompanied by the attenuation of peaks belonging to the O-H stretch and Ni was reported to attain oxidation states of +3.7 following oxidation[22]. This oxidation state has been confirmed Nocera and coworkers[21]. Therefore the possibility of NiO(OH) being the oxidized species can be ruled out. Based on the

studies reported in chapter 4 that were carried out on Co in alkaline solution, we assigned the oxidized species to NiO_2. As the potential is increased to more positive values, E_g and A_{1g} modes simply grow in intensity although their relative intensities remain constant, indicating a constant composition in the material beyond 0.50V.

The as-prepared nickel oxide species was further characterized be cyclic voltammetry as shown in figure 5.3.3.3. The voltammogram exhibits a single quasi-reversible feature with an anodic peak at 0.43V prior to the catalytic wave at 0.80V which similar to those reported for electrodeposited $Ni(OH)_2$ films[13-15] where a single wave, albeit different potentials, observed in the anodic scan. It has recently been reported that the number of electrons associated with the redox feature in the viltammogram involves at least 1.5 electrons, indicating that the oxidation state of Ni in the oxidized species exhibits an oxidation state greater than +3[21]. Based on this evidence and the Raman studies in this work we propose that the oxidized species in NiO_2. As shown in figure 5.3.2.4, the shape of the CV remains constant even after several scans even though the anodic and cathodic waves grow in amplitude. This indicates that although the amount of surface NiO_2 grows with time, its composition remains constant.

The results obtained so far concerning the nickel oxide catalyst are quite different from those reported in chapter 4 for cobalt oxide. Unlike nickel oxide, following the formation of $Co(OH)_2$, three more phases namely, Co_3O_4, CoO(OH) and CoO_2, form successively prior to the catalytic wave. This indicated that although Co and Ni are both first-row transition metals, the mechanism of their catalytic oxidation of water cannot be generalized. Each of them must be looked upon separately. Thus whereas Co oxide species undergoes substantial composition and structural

changes as a function of potential prior to becoming catalytically active[6, 16, 17], the active phase of the nickel oxide catalyst is achieved at lower potentials with little structural transformations[18-20].

The appearance of the catalytic wave at higher overpotentials for cobalt oxide relative to nickel oxide may be accounted for by the multiple compositional changes involved in the material. The conversion of layered hydrotalcite-like $Co(OH)_2$ to spinel-type Co_3O_4 and back to layered hydroxide-type CoO(OH) and CoO_2 would require substantial structural rearrangements which can be thermodynamically demanding. On the other hand the layered structure persists during anodization of the nickel oxide material.

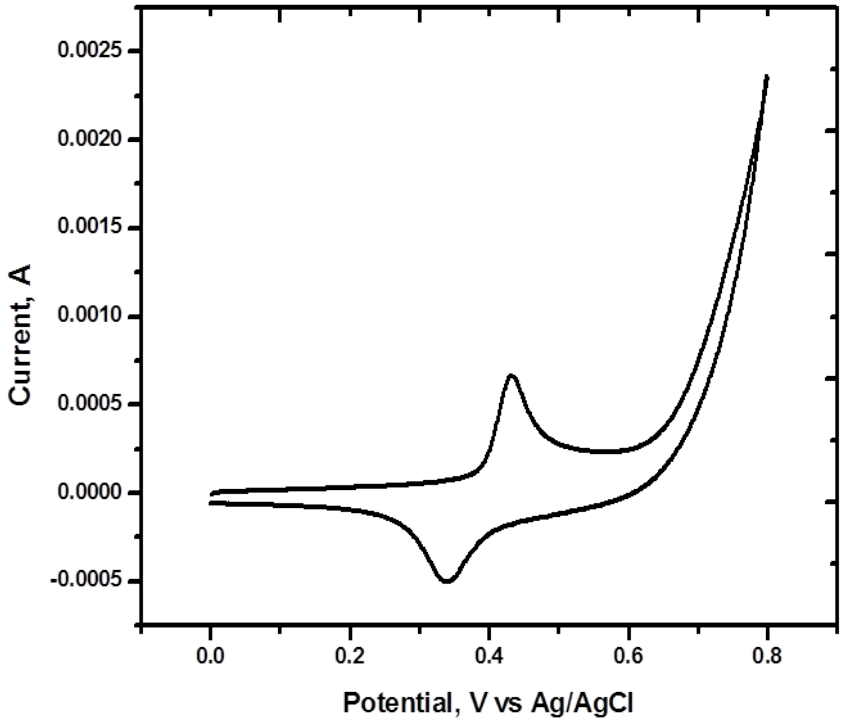

Figure 5.3.2.3 Cyclic voltammogram recorded on bulk Ni 1M NaOH.The potential was scanned continuously at 50mV/sec.

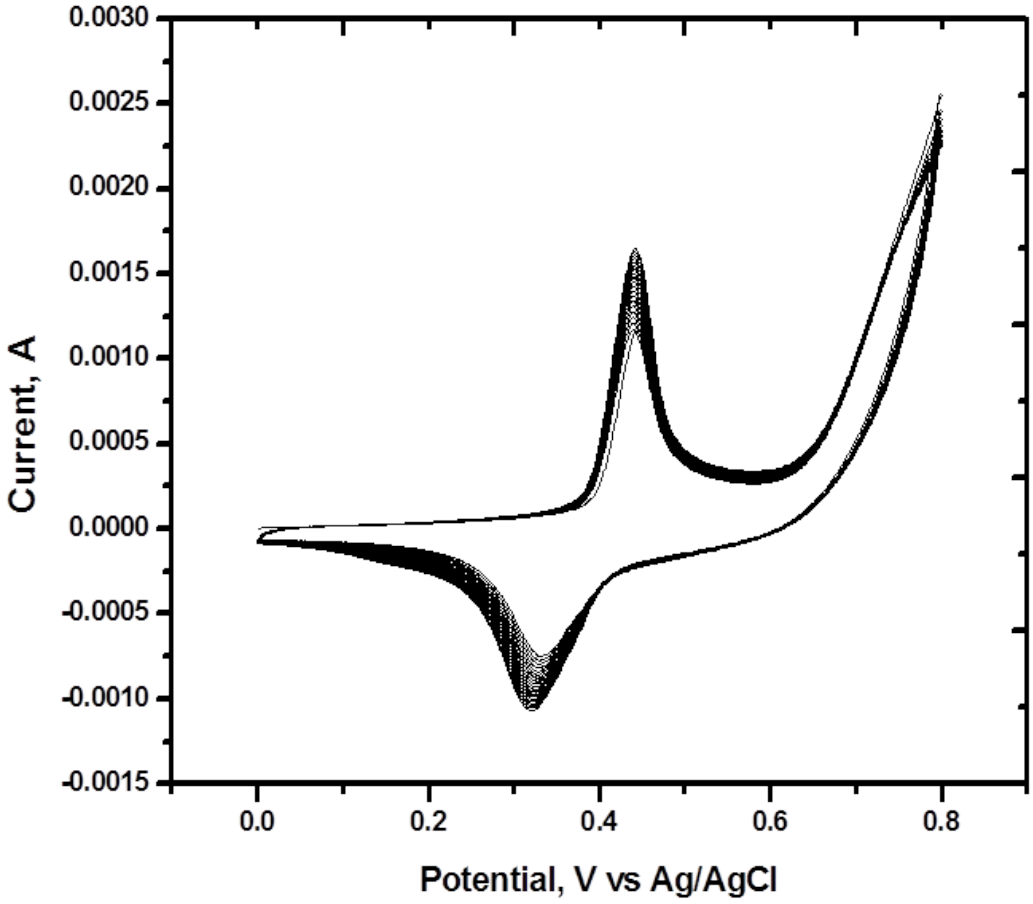

Figure 5.3.2.4 Cyclic voltammogram recorded on bulk Ni 1M NaOH showing a constant composition even after several cycles. The potential was scanned continuously at 50mV/sec.

Finally, the catalytic activity of nickel oxide was evaluated using scanning electrochemical microscopy. The oxygen evolved at various positions at the anodic pole of the bipolar was reduced at the SECM probe. The current was plotted as a function of distance moved by the probe along the electrode as shown in figure 5.3.2.5 (right). Also shown in this figure are the Raman spectra and calculated overpotentials obtained for various positions along the bipolar electrode. Once again, the distribution of the interfacial potential difference between bipolar electrode and the solution was demonstrated by the variation in the current due oxygen reduction. Because the interfacial potential difference is highest at the extremities of the bipolar electrode, the current was highest at the anodic edge and gradually decreased towards the center where the interfacial potential is almost zero. This indicated that the amount of oxygen produced is highest at the edge and reduces to undetectable levels away from the edge.

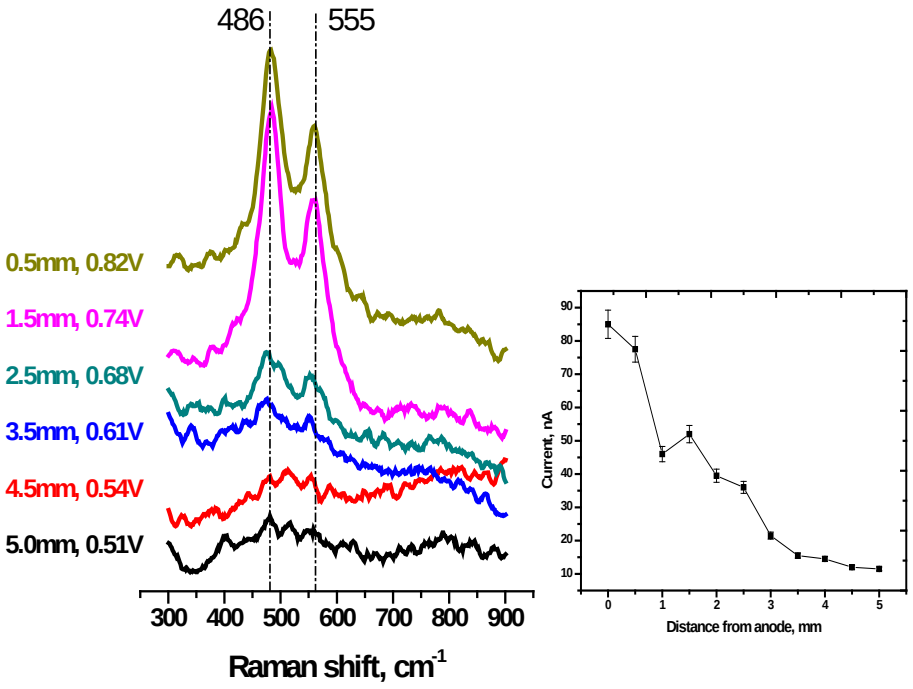

Figure 5.3.2.5 Column to the left: Calculated potentials as a function of position at the anodic pole of the bipolar electrode. Left figure: In situ Raman spectra recorded at positions shown in the left column. Right figure: Tip current due to oxygen reduction at the anodic pole as a function of position.

As observed in figure 5.3.2.5, although the increased SECM probe current is accompanied by increased intensities in the E_g to A_{1g} modes, their relative peak intensities remains constant as a function of increased overpotential at the anodic pole as shown in figure 5.3.2.6. This indicates that the potential driven increased catalytic activity is not due to structural changes in the nickel oxide catalyst. Instead, it is driven by increase in the amount of NiO_2 formed as seen in the cyclic voltammogram in figure 5.3.2.4.

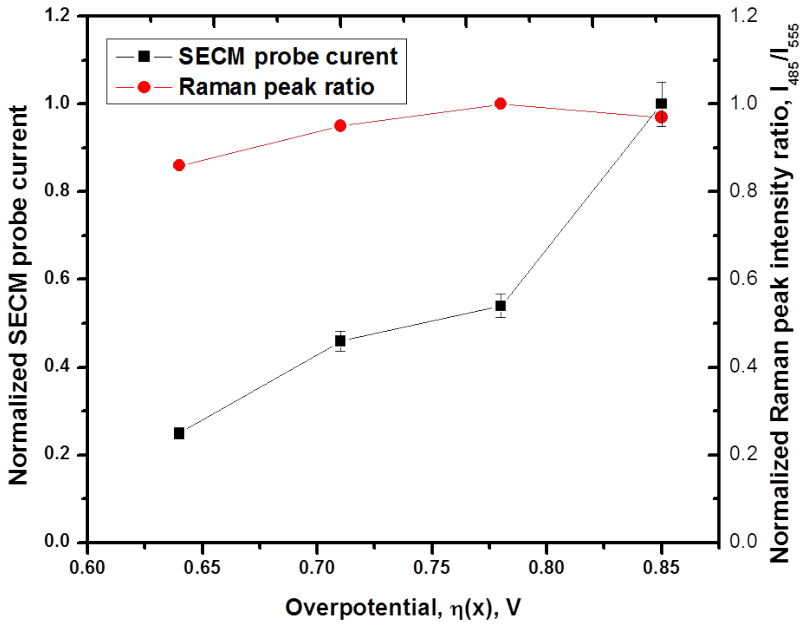

Figure 5.3.2.6 Variation of SECM probe current (black squares) and Raman intensity ratio, $I_{485}/I_{555,}$ (red circles) for the NiO_2 species as a function of overpotential $\eta(x)$.

5. Conclusion

It was demonstrated that the existence of a potential gradient on the surface of the bipolar electrode can be used as a rapid technique to display various compositions of nickel oxide catalyst. Their identities were revealed by Raman microscopy and their activities for water oxidation were screened using SECM. The results of these studies led to the identification of NiO_2 as the active phase of the nickel oxide catalyst. This finding is a preliminary step towards elucidating the mechanism of oxygen evolution by the catalyst which will provide great insight into building structure-activity relationships needed for the development of new catalyst. It was also found that, relative to cobalt oxide, nickel oxide species can catalyze water oxidation of cobalt oxide at lower overpotentials. The higher overpotentials observed in the case of cobalt oxide can be attributed to the multiple transformations in the composition of the cobalt oxide prior to water oxidation compared to a single transformation for nickel oxide.

References

1) Turner, J. A. *Science* **2004,** 305, 972
2) Trasatti, S. *Electrochim. Acta* **1984,** 29-1503
3) Hall, D. E. *J. Electrochem. Soc.* **1983,** 130, 317-321.

4) Li, X. H.; Walsh, F. C.; Pletcher, D. *Phys. Chem. Chem. Phys.* **2010,** 13, 1162

5) McAlpin, J. G.; Surrendranath, Y.; Dinca, M.; Stich, M.; Stoian, S.; Casey, H. W.; Nocera, D.; Britt, R. D. *J. Am. Chem. Soc.* **2010,** *132*, 6882-6883.

6) Gerken, J. B. M., J. G.; Chen, J. Y.C; Rigsby, M. L.; Casey, W. H.; Britt, R. D.; Stahl, S. S. *J. Am.Chem. Soc.* **2011**, *133*, 14431-14442.

7) Lu, P. W. T.; Srinivasan, S. *J. Electrochem. Soc.* **1978,** 125, 1416.

8) Lyons, M. E. G.; Brandon, M. P. *Int. Electrochem. Sci.* **2008,** 3, 1386-1424.

9) Kostecki, R.; Mclarnon, F. *J. Electrochem. Soc.* **1997,** 485-493.

10) Desilvesto, J.; Corrigan, D. A.; Weaver, M. J. *J. Phys. Chem* **1986,** 90, 6408-

11) Desilvesto, J.; Corrigan, D. A.; Weaver, M. J. *J. Electrochem. Soc.* **1988,** 135, 885-892.

12) Cornilson, B. C.; Shan, X. Y.; Loyselle, P. L. *J. Power Sources* **1990,** 29, 453-

13) Corrigan, D. A.; Bendert, R. M. *J. Electrochem. Soc.* **1989,** 136, 723-728

14) Oliva, P.; Leonardi, J.; Laurant, J. F.; Delmas, C.; Braconnier, J. J.; Figlarz, M.; Guibert, A. *J. Power Sources* **1982,** 8, 229-255

15) Wruck, D. A.; Rubin, M. *J. Electrochem. Soc.***1993,** 1097-1104.

16) Kanan, M. W.; Yano, J.; Surendranath, Y.; Dinca, M.; Yachandra, V. K.; Nocera, D. G. *J. Am. Chem. Soc.* **2010,** 132, 13692-13701.

17) Yeo, B. S.; Bell, A. T. *J. Am. Soc.* **2011,** 133, 5587-5593

18) Dinca, M.; Surendranath, Y.; Nocera, D. G. *PNAS* **2009,** 107, 10337-10341.

19) Yeo, B. S.; Bell, A. T. *J. Phys. Chem. C* **2012,** 116, 8494-8400.

20) Bediako, D. K.; Lassallle-Kaiser, B.; Surendranath, Y.; Yano, J.; Yachandra,; Nocera, D. G. *J. Am. Chem. Soc.* **2012,** 134, 6801-6809.

21) Desilvestro, J.; Corrigan D.; Weaver, M. J. Electrochem. *Soc.* **1988,** 135, 885-892

Chapter 6

Summary and Future Outlook

This dissertation demonstrates the use of bipolar electrochemistry as a novel technique for surface patterning and material screening. It is the fact that the bipolar electrode is physically isolated makes the technique unique. Moreover, the ability to control electrochemical reactions and create gradients of various widths, lengths and geometries with very simple and inexpensive instrumentation is quite remarkable.

We presented self-assemble monolayers of thiol molecules functionalized with a redox moiety as a non-destructive method for patterning electrode surfaces. Because the composition of electrocatalyst is highly dependent on potential, bipolar electrochemistry offers a high throughput platform for screening the composition because various forms of the catalyst can be simultaneously displayed on a single surface. By combining bipolar electrochemistry with techniques such as scanning electrochemical microscopy, composition-activity relationships for can be rapidly generated for the design of new catalysts. Throughout this work, it was

demonstrated that Raman spectroscopy can be used to report electrochemical reactions and evaluate reaction gradients on bipolar electrodes. Because faradaic reactions are driven by the potential difference across the electrode surface, the observe Raman reponse from the surface of a bipolar electrode can give insight into the potential distribution on the surface – an information that would be otherwise difficult to obtain due to the lack of physical contact between the electrode and the rest of the instrumentation.

Our future goal is to extend the screening capability of bipolar electrochemistry to biologically relevant molecules. A very important step in drug discovery is to screen a chemical library of potential candidates. Once promising candidates have been selected a more thorough screening will be performed by establishing a dose-response relationship for each one. Because this process is very time-consuming due to sequential testing, limited number of doses is usually tested. One way to increase the number of points on a dose-response plot and also reduce the screening time is to generate concentration gradients of both the drug candidate and its target. Although is point have been demonstrated using microfuidics, the instrumentation is very complicated and requires expertise. Our approaches is to functionalize the enzyme horseradish peroxidase (HRP) with redox-active moiety containing a diazonium salt. Diazonium compounds can be deposited on glassy carbon electrode upon application of a negative potential. Therefore a concentration gradient of the diazonium-functionalized protein can be generated at the cathodic pole of a bipolar electrode. Next, we will generate a gradient of the substrate 2,2'-azino-bis(3-ethylbenzothiazoline-6-sulphonic acid) (ABTS) which produces a blue-green color upon reaction with HRP. It acts as the electron acceptor in the catalytic oxidation of hydrogen peroxide by HRP. The reaction can be stopped for measurement using 1% sodium dodecyl sulfate (SDS). The ABTS gradient will be created on a filter paper by simple diffusion. The filter paper will then be

placed over the electrode containing the protein gradient and its interact with the substrate can be determined by visual inspection. For more quantitative results the UV-Vis spectrum will be recorded at various positions corresponding to different concentrations of the protein and its substrate.